Proceedings of the

14th Patras Workshop on Axions, WIMPs and WISPs

18-22 June 2018

DESY, Hamburg, Germany

Editor: Todd C. Kozlowski

Verlag Deutsches Elektronen-Synchrotron DESY

Proceedings of the

14th Patras Workshop on Axions, WIMPs and WISPs

PATRAS 2018

June 17-22, 2018
Hamburg, Germany

Editors: Todd Kozlowski

Verlag Deutsches Elektronen-Synchrotron

Impressum

Proceedings of the 14th Patras Workshop on Axions, WIMPs and WISPs (PATRAS 2018)
June 17-22, 2018, Hamburg, Germany

Conference homepage
`http://www.axion-wimp2018.desy.de`

Slides at
`http://indico.desy.de/conferenceDisplay.py?confId=123`

Online proceedings at
`http://www-library.desy.de/confprocs.html`

Editors:
Axel Lindner, Todd Kozlowski
December 2018
DESY-PROC-2018-03
ISBN 978-3-945931-22-6
ISSN 1435-8077

Published by
Verlag Deutsches Elektronen-Synchrotron
Printed by
Kopierstelle Deutsches Elektronen-Synchrotron
Notkestraße 85
22607 Hamburg
Germany

Organizing Committee

International Organizing Committee:

Vassilis Anastassopoulos
University of Patras

Laura Baudis
University of Zurich

Joerg Jaeckel
University of Heidelberg

Axel Lindner (Chair)
Deutsche Elektronen-Synchrotron (DESY)

Andreas Ringwald
Deutsche Elektronen-Synchrotron (DESY)

Marc Schumann
University of Freiburg

Yannis K. Semertzidis
CAPP/IBS & KAIST

Konstantin Zioutas (Co-Chair)
University of Patras & CERN

Local organizing committee (DESY):

Brigit Breetzke
Michaela Grimm
Petra Hendrikman-Verstegen
Gabriele Kalhoefer
Axel Lindner (Chair)
Andreas Ringwald

14th Patras Workshop on Axions, WIMPs and WISPs

18-22 June 2018

DESY, Hamburg, Germany

Photo: NN

Scientific Programme

- Direct and Indirect Searches for Dark Matter
- Direct and Indirect Searches for Axions & WISPs
- Searches for Hidden Sector Photons
- Astrophysical Signatures for Dark Matter
- Review of Collider Experiments
- New Developments: Theory & Experiment
- Scalar Dark Energy: Theory & Experiment

Organizing committee:
Axel Lindner (Chair, DESY)
Vassilis Anastassopoulos (University of Patras)
Laura Baudis (University of Zurich)
Joerg Jaeckel (University of Heidelberg)
Andreas Ringwald (DESY)
Marc Schumann (University of Freiburg)
Yannis Semertzidis (CAPP/IBS & KAIST)
Konstantin Zioutas (Co-Chair, University of Patras)

Deadline for abstract submission and
early registration: 30 April 2018

http://axion-wimp.desy.de

SPONSORS: CERN, DESY, IBS/CAPP, SFB 676 (UNIVERSITY OF HAMBURG), UNIVERSITY OF FREIBURG, UNIVERSITY OF HEIDELBERG, UNIVERSITY OF PATRAS, UNIVERSITY OF ZURICH

Preface

After 10 years the Patras Workshop series on Axions, WIMPs and WISPs was back to DESY in Hamburg for its 14th incarnation. 151 participants enjoyed presentations and lively discussions on cosmology, astrophysics, particle physics theory and, last but no least, new experimental results as well as progress and plans towards future detectors. A decade ago the workshop had 64 attendees.
The workshop organization followed closely previous good experiences with wildly mixed topics in each session "forcing" all communities to attend, but added also new elements like combined oral and poster presentations. A special highlight was the science slam to present facets of our physics fields in an entertaining manner to other scientists at DESY and the public. The audience voted for Ciaran O'Hare (Universidad de Zaragoza) as the winner of this little competition with his "Safari in the Milky Way".

No doubt, WISPs have caught up on WIMPs and moved out from some niches. WISP physics is becoming main-stream science and join in with WIMP activities also in fostering a lively community with fascinating theoretical and instrumental developments in spite of lacking any significant discovery.
Hopes are thigh that this might change soon. WIMP detectors are approaching the neutrino floor and ADMX has demonstrated its sensitivity to detect dark matter axions as predicted by benchmark models, just to name two examples. Perhaps "Patras 2019" to be held at Freiburg, Germany, in the first week of June, will see the first WIMP and/or WISP discovery!

As the chairperson of the organizing committee I thank my committee colleagues for the very constructive collaboration and the fun working with you!

In the name of the organizing committee I thank all attendees to "Patras" 2018" very much! You made it a success!

Axel Lindner

Contents

Non-minimally coupled Scalar Dark Matter from Inflationary Fluctuations

Gonzalo Alonso-Álvarez[1]

[1]Institute for Theoretical Physics, Heidelberg University, Heidelberg, Germany

DOI: http://dx.doi.org/10.3204/DESY-PROC-2018-03/Alonso-Alvarez_Gonzalo

It is well known that light scalar fields present during inflation are coherently excited. We show that if the field couples to gravity in a non-minimal way, the fluctuations at large scales are suppressed with respect to the small scales ones. This fact allows for the field excitations to make a sizeable contribution to the energy density of the universe without generating too large isocurvature fluctuations at observable scales. We show that this mechanism could generate all the observable dark matter and study the main cosmological implications of this setup.

1 Introduction

The material presented here is based on [1], to which we refer for more in-depth explanations and discussion, together with a more complete set of references.

Gravitational observations in cosmological and astrophysical settings strongly suggest that a large fraction of the energy density of our Universe is stored in some form of dark matter. New, weakly interacting and massive bosonic degrees of freedom are well motivated ways to explain this. Masses in a wide range of scales are viable, from the ultra light fuzzy dark matter limit to very heavy fields lying close to the Planck scale. Different observables and experimental techniques have been developed to explore this paradigm. The GeV-TeV range has been the most extensively tested, but new ideas will allow to probe lighter fields down to the meV in the future. Some astrophysical observations give a hint for dark matter with a mass around the keV, further motivating theoretical studies of this intermediate mass range.

The two standard frameworks of bosonic dark matter production, thermal freeze out and the misalignment mechanism, require modifications or tuning of parameters to yield the correct relic abundance for these intermediate mass values. It is therefore timely to explore alternative mechanisms that could explain the origin of dark matter in this mass range.

It was recently shown in [2] that dark photon dark matter can be generated from fluctuations of inflationary origin. We argue that an analogue production occurs for a scalar field non-minimally coupled to gravity. A similar idea was used in [3] in the context of Higgs portal dark matter. The non-minimal coupling suppresses the amplitude of the fluctuations at large scales, which explains why isocurvature perturbations have not been observed by the Planck mission [4] in the cosmic microwave background (CMB). We study the quantum generation of the fluctuations and their cosmological evolution to obtain the late-times power spectrum. This allows us to make precise quantitative statements regarding the present abundance of dark matter and the particular features of the mechanism.

2 Non-minimal coupling to gravity

The action for a massive scalar field non-minimally coupled to gravity that we consider is

$$S = \int \mathrm{d}^4x\,\sqrt{-g}\left(\frac{1}{2}\left(m_{\mathrm{Pl}}^2 - \xi\phi^2\right)R - \frac{1}{2}\partial_\mu\phi\partial^\mu\phi - \frac{1}{2}m^2\phi^2\right). \tag{1}$$

We use the mostly plus convention and focus on positive values of the coupling constant ξ. The usual Einstein equations should be modified to take into account the presente of the direct coupling between ϕ and the Ricci scalar R. The modifications induced are however suppressed by powers of ϕ/m_{Pl} and remain small as long as ϕ doesn't probe field values close to the Planck scale. This condition is amply satisfied in our setup and we can consequently neglect any backreaction effects on the geometry.

We specify to a Florian-Lemaitre-Robertson-Walker (FLRW) background. The Ricci scalar is given by $R = 3(1-3\omega)H^2$, H being the Hubble parameter and $\omega = p/\rho$ the equation of state of the fluid driving the expansion. The classical equation of motion for ϕ reads

$$\left(\partial_t^2 + 3H\partial_t + \frac{k^2}{a^2} + m^2 + \xi R\right)\phi(k,t) = 0. \tag{2}$$

3 Cosmological evolution

3.1 Quantum evolution during inflation

Let us first argue that any preinflationary homogeneous initial condition ϕ_0 is washed out due to the non-minimal coupling. We solve the $k \to 0$ limit of Eq. (2) adopting a constant value of the Hubble parameter during inflation. The result is an exponential suppression,

$$\phi_{\mathrm{E}} \simeq \phi_0\ \mathrm{e}^{-\frac{\mathrm{Re}(\alpha_-)}{2}N}, \tag{3}$$

where $\alpha_- = 3 - \sqrt{9-48\xi}$ and N is the total number of efolds of inflation. However, even if the average field $\langle\phi\rangle$ is quickly damped away, the two-point correlator $\langle\phi^2\rangle$ receives sizeable contributions from non-vanishing momentum modes due to the growth of quantum fluctuations.

This effect can be understood within the framework of quantum field theory in classically curved backgrounds. A computation leads to the power spectrum of a mode of comoving momentum k:

$$\mathcal{P}_\phi(k, a(t)) = \left(\frac{H_I}{2\pi}\right)^2 \frac{\pi}{2}\left(\frac{k}{a(t)H_I}\right)^3 \left|H_\nu^{(1)}\left(\frac{k}{a(t)H_I}\right)\right|^2. \tag{4}$$

Here, $H_\nu^{(1)}$ is the Hankel function of the first kind and ν is given by $\nu^2 = 9/4 - 12\xi - m^2/H_I^2$. This power spectrum presents a divergence for large momenta (it grows as k^2), which means that the variance of the field seems to be dominated by the ultraviolet modes. We find a regularization scheme that provides an unambiguous and finite value of the energy density at late times. Being assured that this procedure leads to well-defined observables in the late universe, we can evaluate the regularized version of Eq. (4) for modes that are well outside the horizon, i.e. at a time when they satisfy $k \ll a(t)H_I$.

$$\mathcal{P}_\phi^{(\mathrm{reg})}(k,t) \simeq \mathcal{P}_{\phi_0}^{(\mathrm{reg})}(k)\left(\frac{k}{a(t)H_{\mathrm{I}}}\right)^{3-2\nu}, \quad \text{with} \quad \mathcal{P}_{\phi_0}^{(\mathrm{reg})}(k) = \left(\frac{H_{\mathrm{I}}}{2\pi}\right)^2 \frac{2^{2\nu-1}\Gamma^2(\nu)}{\pi}. \tag{5}$$

This result serves as the initial condition for the posterior evolution.

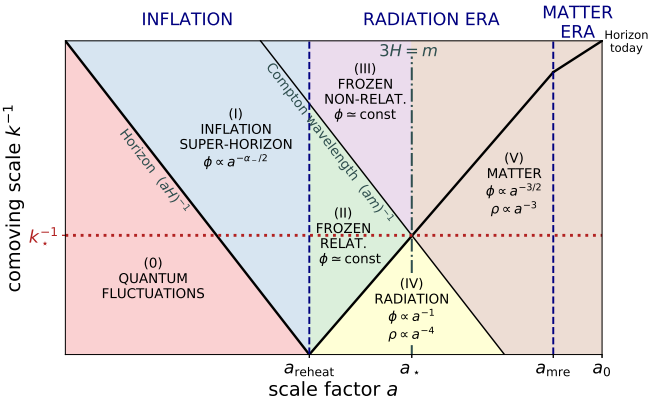

Figure 1: (From [1]). Cosmological evolution of momentum modes as a function of their comoving wavelength k^{-1}. The evolution is distinct in each regime represented by a different color, according to Eq. (2). The modes evolve in horizontal lines from left to right in the figure. They start their life as small quantum fluctuations during inflation (0), whose amplitude grows as they exit the horizon. In the superhorizon inflationary regime (I), the large effective mass suppresses their amplitude. Once inflation ends, the field acquires its late time mass and becomes frozen on superhorizon scales (II and III). If it reenters the horizon while still relativistic (IV), it oscillates with a damped amplitude. At late times when the modes are non-relativistic and Hubble friction is overcome (V), the modes redshift like pressureless matter [5].

3.2 Classical evolution and late time observables

After horizon exit, the modes transition into a regime in which they can be treated classically. This means that their evolution can be traced by solving the classical equation of motion Eq. (2). The power spectrum is obtained by evolving the initial condition Eq. (5).

The solution of the equation of motion in the different regimes of expansion of the Universe is summarized in Fig. 1. The power spectrum of the field at late times is dominated by the modes close to $k_\star$ (highlighted in red), as this is the mode that gets suppressed the least during the cosmological evolution. The corresponding comoving scale is $k_\star^{-1} \simeq 4.1 \cdot 10^7 \text{ km} \cdot \sqrt{\text{eV}/m}$, which is orders of magnitude below the ones accessible to cosmological probes.

The amplitude of isocurvature perturbations at CMB scales is read off the density contrast power spectrum, which can be derived from the field power spectrum. The result is shown in Fig. 2. For a large enough non-minimal coupling, the amplitude of isocurvature perturbations at CMB scales falls below the constraints set by Planck. The peaked power spectrum implies that the bulk of the energy density is stored in overdensities of typical comoving size $k_\star^{-1}$.

We obtain the relic abundance of the field and compare with the observed dark matter one,

$$\frac{\Omega_\phi}{\Omega_{\rm DM}} \simeq C(\alpha_-) \frac{1}{m_{\rm pl}^2} H_{\rm eq}^{-\frac{1}{2}} \; H_{\rm I}^{\frac{1}{2}(4-\alpha_-)} \; m^{\frac{1}{2}(\alpha_-+1)}, \tag{6}$$

where $C(\alpha_-)$ is an $\mathcal{O}(1)$ factor. The different lines in Fig. 3 show values of the scale of inflation for which the dark matter abundance is reproduced, as a function of the mass and the non-minimal coupling. The red region in the figure is excluded by the Planck isocurvature limit and in the grey area graviton-mediated decay could render the field cosmologically unstable.

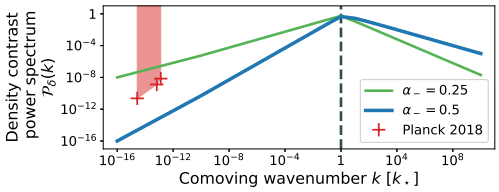

Figure 2: (From [1]). Isocurvature power spectrum. It peaks at the scale $k_\star^{-1}$ and drops below Planck limits at large scales.

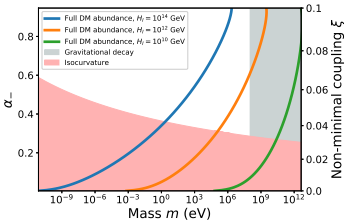

Figure 3: (From [1]). Parameter space of the model. See text for more details.

4 Summary and discussion

Generated in a purely gravitational way, the dark matter in this scenario is a (pseudo)scalar with a small non-minimal coupling to gravity. Quantum fluctuations of the field are amplified during the inflationary epoch in the very early Universe, and the energy density thus produced behaves as non-relativistic, pressureless matter at late times. The density perturbations are of isocurvature type, but the the non-minimal coupling suppresses their amplitude at large scales. The scenario thus avoids the stringent constraints on dark matter isocurvature set by Planck.

As overdensities around the comoving scale $k_\star^{-1}$ are very large, we expect them to collapse and form bound structures early on. The presence of such clumps of dark matter, together with a potentially observable level of isocurvature, are the most particular features of this setup. Although the production mechanism presented is purely gravitational, sufficiently weak couplings to the visible sector are compatible with it.

5 Acknowledgements

The author would like to thank Joerg Jaeckel for his collaboration on the work presented here. This project has received funding from the European Union's Horizon 2020 research and innovation programme under the Marie Sklodowska-Curie grant agreement No 674896 (ITN ELUSIVES). The author acknowledges support by a "La Caixa" foundation fellowship.

6 Bibliography

References

[1] G. Alonso-Álvarez and J. Jaeckel, "Lightish but clumpy: scalar dark matter from inflationary fluctuations," arXiv:1807.09785 [hep-ph].

[2] P. W. Graham, J. Mardon and S. Rajendran, "Vector Dark Matter from Inflationary Fluctuations," Phys. Rev. D **93** (2016) no.10, 103520 doi:10.1103/PhysRevD.93.103520 [arXiv:1504.02102 [hep-ph]].

[3] C. Cosme, J. G. Rosa and O. Bertolami, "Scale-invariant scalar field dark matter through the Higgs portal," JHEP **1805** (2018) 129 doi:10.1007/JHEP05(2018)129 [arXiv:1802.09434 [hep-ph]].

[4] Y. Akrami *et al.* [Planck Collaboration], "Planck 2018 results. X. Constraints on inflation," arXiv:1807.06211 [astro-ph.CO].

[5] P. Arias, D. Cadamuro, M. Goodsell, J. Jaeckel, J. Redondo and A. Ringwald, "WISPy Cold Dark Matter," JCAP **1206** (2012) 013 doi:10.1088/1475-7516/2012/06/013 [arXiv:1201.5902 [hep-ph]].

A global study of the extended scalar singlet model

Ankit Beniwal[1,2*], *Marek Lewicki*[2,3], *Martin White*[2] *and Anthony G. Williams*[2]

[1]The Oskar Klein Centre for Cosmoparticle Physics, Department of Physics, Stockholm University, AlbaNova, SE-106 91 Stockholm, Sweden
[2]ARC Centre of Excellence for Particle Physics at the Terascale (CoEPP) and CSSM, Department of Physics, University of Adelaide, South Australia 5005, Adelaide, Australia
[3]Kings College London, Strand, London, WC2R 2LS, United Kingdom

DOI: http://dx.doi.org/10.3204/DESY-PROC-2018-03/Beniwal_Ankit

We present preliminary results from a global study of the extended scalar singlet model with a fermionic dark matter (DM) candidate. In addition to requiring a successful electroweak baryogenesis, we combine constraints from the DM relic density, direct detection limits from PandaX-II experiment, electroweak precision observables and Higgs searches at colliders. In agreement with previous studies, we find that the model can simultaneously explain (at least a part of) the observed DM abundance and matter-antimatter asymmetry. The viable points often lead to strong gravitational wave (GW) signals that can potentially be probed at future GW experiments.

1 Singlet fermion dark matter model

We extend the Standard Model (SM) by adding a new real scalar singlet S and a Dirac fermion dark matter (DM) field ψ. The model Lagrangian is given by [1]

$$\mathscr{L} = \mathscr{L}_{\rm SM} + \mathscr{L}_S + \mathscr{L}_\psi + \mathscr{L}_{\rm portal}, \tag{1}$$

where $\mathscr{L}_{\rm SM}$ is the SM Lagrangian,

$$\mathscr{L}_S = \frac{1}{2}(\partial_\mu S)(\partial^\mu S) + \frac{1}{2}\mu_S^2 S^2 + \frac{1}{3}\mu_3 S^3 - \frac{1}{4}\lambda_S S^4, \tag{2}$$

$$\mathscr{L}_\psi = \overline{\psi}(i\partial\!\!\!/ - \mu_\psi)\psi - g_S\overline{\psi}\psi S, \tag{3}$$

$$\mathscr{L}_{\rm portal} = -\mu_{\Phi S}\Phi^\dagger\Phi S - \frac{1}{2}\lambda_{\Phi S}\Phi^\dagger\Phi S^2. \tag{4}$$

A linear term of the form $\mu_1^3 S$ is removed by a constant shift $S \to S + \sigma$. When $\mu_3 = g_S = \mu_{\Phi S} = 0$, the model reduces to the scalar Higgs portal [2, 3].

After electroweak symmetry breaking (EWSB), both Φ and S acquire the following VEVs in the unitary gauge

$$\Phi = \frac{1}{\sqrt{2}}\begin{pmatrix} 0 \\ v_0 + \varphi \end{pmatrix}, \quad S = s_0 + s. \tag{5}$$

*Speaker

Constraints (Experiment)	Criteria	Likelihood	Ref.
Relic density (*Planck*)	$\Omega_\psi h^2 \leq \Omega_{\rm DM} h^2 = 0.1188$	one-sided Gaussian	[7]
Direct detection (PandaX-II)	$\sigma_{\rm SI}^{\rm eff} \leq \sigma_{\rm PandaX\text{-}II}$	one-sided Gaussian	[8]
Electroweak baryogenesis	$v_c/T_c \geq 0.6$	one-sided Gaussian	–
Electroweak precision observables	$\Delta S = 0.04 \pm 0.11$ $\Delta T = 0.09 \pm 0.14$ $\Delta U = -0.02 \pm 0.11$	3D Gaussian	[9]
Direct Higgs searches	–	Step function	[10]
Higgs signal strengths	–	1D Gaussian	[11]

Table 1: Summary of constraints included in our global fit. Here v_c is the Higgs VEV at the critical temperature T_c.

Consequently, the fermion DM picks up a mass term, i.e., $m_\psi = \mu_\psi + g_S s_0$.

The portal interaction Lagrangian in Eq. (4) induces a mixing between φ and s fields. To diagonalise the squared mass matrix $\mathcal{M}^2$, we introduce the physical mass eigenstates (h, H) as

$$\begin{pmatrix} h \\ H \end{pmatrix} = \begin{pmatrix} \cos\alpha & -\sin\alpha \\ \sin\alpha & \cos\alpha \end{pmatrix} \begin{pmatrix} \varphi \\ s \end{pmatrix}, \tag{6}$$

where α is the mixing angle. Thus, for small mixing, h is a SM-like Higgs boson, whereas H is dominated by the scalar singlet.

2 Constraints

In light of the recent discovery of a SM-like Higgs boson [4, 5], we set

$$m_h = 125.13\,\text{GeV}, \quad v_0 = 246.22\,\text{GeV}. \tag{7}$$

Thus, our model is completely described by the following 7 free parameters

$$m_H, \quad s_0, \quad \mu_3, \quad \lambda_S, \quad \alpha, \quad m_\psi, \quad g_S. \tag{8}$$

To make parameter inferences, we adopt a frequentist approach and perform 7-dimensional (7D) scans of the model using the `Diver_v1.4.0` [6] package. The set of constraints included in our global fit are summarised in Table 1.

3 Preliminary results

In Fig. 1, we show 2D profile likelihood plots from our global fit in the (m_H, s_0) and (m_H, α) planes. Values of $m_H \lesssim m_h/2 = 62.56\,\text{GeV}$ are ruled out by the observed Higgs signal strengths. This is true regardless of the values of α as the $h \to HH$ decay mode is dominant in this region, and leads to a reduction of the SM-like Higgs signal strength. When $m_H \simeq m_h$, the model can evade all constraints as the contribution from both scalars cancels out. Thus, all values of α are allowed. On the other hand, values of $m_H \gtrsim 4\,\text{TeV}$ are ruled out as they either lead to runaway directions, $\lambda_{\Phi S} \leq -2\sqrt{\lambda_\Phi \lambda_S}$, or non-perturbative couplings, $|\lambda_{\Phi S}|, |\lambda_\Phi| \geq 4\pi$.

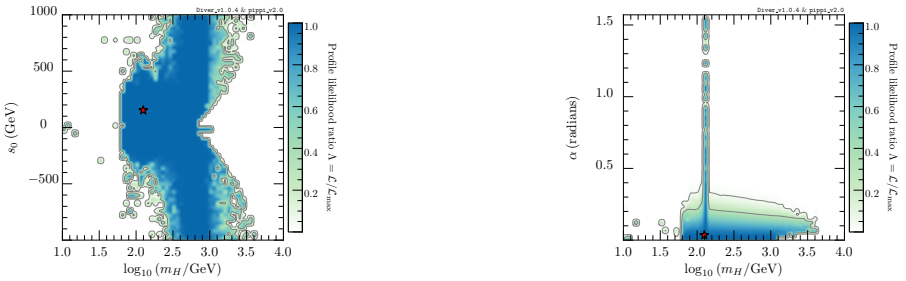

Figure 1: 2D profile likelihood plots from a 7D scan of the model in the (m_H, s_0) and (m_H, α) planes. The best-fit point is marked by the red star.

For the viable points that satisfy all constraints, we compute their gravitational wave (GW) spectra using the expressions given in Ref. [12]. The dependence of the GW spectra on v_*/T_* is shown in Fig. 2. For comparison, we also show the detection prospects of future GW experiments such as LISA, DECIGO and BBO. As is evident from the plot, large values of v_*/T_* lead to a stronger phase transition and a stronger GW signal. In particular, they lead to better prospects for detection at future GW experiments.

4 Conclusions

We have presented preliminary results from a global fit of the extended scalar singlet model with a fermionic DM candidate. Using the constraints from the *Planck* measured DM relic density, direct detection limits from the PandaX-II experiment, electroweak baryogenesis, electroweak precision observables and Higgs searches at colliders, we performed a global fit of the model. In agreement with previous studies, we found that the model can explain (at least a part of) the observed DM abundance and matter-antimatter asymmetry. In addition, the gravitational wave (GW) spectra of viable points are often found to be within reach of future GW experiments.

Acknowledgements

AB thanks the organizers of the Patras 2018 workshop for the opportunity to present this work. This work was supported by the Swedish Research Council (contract 621-2014-5772), ARC Centre of Excellence for Particle Physics at the Terascale (CoEPP) (CE110001104) and the Centre for the Subatomic Structure of Matter (CSSM). ML was supported in part by the Polish MNiSW grant IP2015 043174 and STFC grant number ST/L000326/1. AB was supported by the Australian Postgraduate Award (APA). MW is supported by the Australian Research Council Future Fellowship FT140100244.

References

[1] A. Beniwal, M. Lewicki, M. White and A. G. Williams, in preparation for JHEP (2018).

[2] V. Silveira and A. Zee, Phys. Lett. **161B** (1985) 136. doi:10.1016/0370-2693(85)90624-0.

[3] J. McDonald, Phys. Rev. D **50**, 3637 (1994) doi:10.1103/PhysRevD.50.3637 [hep-ph/0702143 [hep-ph]].

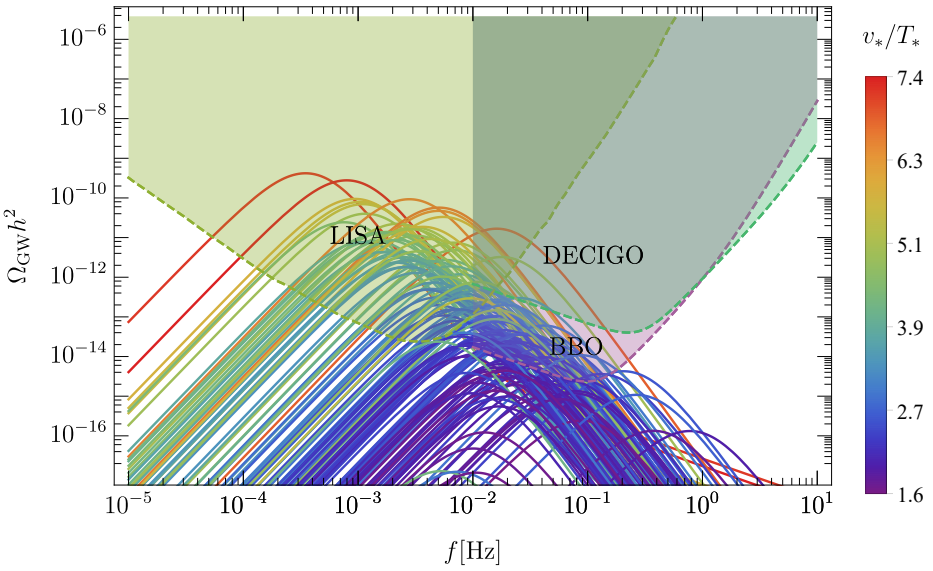

Figure 2: Gravitational wave (GW) spectra of viable points along with the projected sensitivities of future GW experiments such as LISA, DECIGO and BBO. Here v_* is the Higgs VEV at the transition temperature T_*.

[4] G. Aad *et al.* [ATLAS Collaboration], Phys. Lett. B **716** (2012) 1 doi:10.1016/j.physletb.2012.08.020 [arXiv:1207.7214 [hep-ex]].

[5] S. Chatrchyan *et al.* [CMS Collaboration], Phys. Lett. B **716** (2012) 30 doi:10.1016/j.physletb.2012.08.021 [arXiv:1207.7235 [hep-ex]].

[6] G. D. Martinez *et al.* [GAMBIT Collaboration], Eur. Phys. J. C **77** (2017) no.11, 761 doi:10.1140/epjc/s10052-017-5274-y [arXiv:1705.07959 [hep-ph]].

[7] P. A. R. Ade *et al.* [Planck Collaboration], Astron. Astrophys. **594** (2016) A13 doi:10.1051/0004-6361/201525830 [arXiv:1502.01589 [astro-ph.CO]].

[8] X. Cui *et al.* [PandaX-II Collaboration], Phys. Rev. Lett. **119** (2017) no.18, 181302 doi:10.1103/PhysRevLett.119.181302 [arXiv:1708.06917 [astro-ph.CO]].

[9] J. Haller, A. Hoecker, R. Kogler, K. Monig, T. Peiffer and J. Stelzer, Eur. Phys. J. C **78**, no. 8, 675 (2018) doi:10.1140/epjc/s10052-018-6131-3 [arXiv:1803.01853 [hep-ph]].

[10] P. Bechtle, O. Brein, S. Heinemeyer, O. Stal, T. Stefaniak, G. Weiglein and K. E. Williams, Eur. Phys. J. C **74**, no. 3, 2693 (2014) doi:10.1140/epjc/s10052-013-2693-2 [arXiv:1311.0055 [hep-ph]].

[11] P. Bechtle, S. Heinemeyer, O. Stal, T. Stefaniak and G. Weiglein, Eur. Phys. J. C **74**, no. 2, 2711 (2014) doi:10.1140/epjc/s10052-013-2711-4 [arXiv:1305.1933 [hep-ph]].

[12] A. Beniwal, M. Lewicki, J. D. Wells, M. White and A. G. Williams, JHEP **1708**, 108 (2017) doi:10.1007/JHEP08(2017)108 [arXiv:1702.06124 [hep-ph]].

Searching for neutrinoless double-beta decay with GERDA

Riccardo Brugnera[1]

[1]University of Padova and INFN Padova, Italy
on behalf of the GERDA Collaboration

DOI: http://dx.doi.org/10.3204/DESY-PROC-2018-03/Brugnera_Riccardo

The GERDA experiment at LNGS (Italy) is searching for neutrinoless double-beta decay of ^{76}Ge by operating bare germanium detectors enriched in ^{76}Ge to about 88% in liquid argon. Thanks to a background index of $(5.6^{+3.4}_{-2.4} \cdot 10^{-4})$ cts/(keV·kg·yr) for the BEGe detectors and $(5.7^{+4.1}_{-2.6} \cdot 10^{-4})$ cts/(keV·kg·yr) for the coaxial detectors and a Phase II exposure of 58.9 kg·yr a median sensitivity on the half-life of ^{76}Ge of $T_{1/2} = 1.1 \cdot 10^{26}$ yr (for 90% C.L. limit) has been reached. No signal event was detected and a lower limit of $T_{1/2} > 0.9 \cdot 10^{26}$ yr (90% C.L.) has been obtained.

1 Introduction

Double-beta decay is the simultaneous beta decay of two neutrons in a nucleus of mass A and charge Z. It is a second order weak process, predicted by the Standard Model: $(A, Z) \rightarrow (A, Z+2) + 2e^- + 2\overline{\nu}_e$. This $2\nu\beta\beta$ process has been experimentally observed in even-even nuclei and can be detected only when the single beta decay is energetically forbidden or strongly suppressed because of a large change of spin between initial and final state. Extensions of the Standard Model predict that also $0\nu\beta\beta$ decay, $(A, Z) \rightarrow (A, Z+2) + 2e^-$, could occur. The process has a clear signature with a mono-energetic line in the observed electron sum energy spectrum at $Q_{\beta\beta}$. Its observation implies that the lepton number is violated by two units. It would prove that neutrinos have a Majorana mass component being their own anti-particle. The GERDA experiment [1] is designed to search for $0\nu\beta\beta$ decay of the ^{76}Ge. In the following the experimental setup and recent results will be presented.

2 The experiment

The GERDA experiment is located at the Laboratori Nazionali del Gran Sasso (LNGS) in Italy with an overburden of 3500 m.w.e.. Germanium detectors enriched in ^{76}Ge to about 88% are operated bare in a cryostat filled with 64 m^3 of liquid argon (LAr). They simultaneously work as source and detector maximizing the detection efficiency and have a very good energy resolution at $Q_{\beta\beta}$ of $O(0.1\%)$. Their intrinsic impurity concentration is very low and consequently the level of intrinsic backgrounds is negligible. The cryostat is contained in a water tank which forms a passive shield and neutron moderator. Being instrumented with PMTs the water tank operates also as an active Cherenkov muon veto. The apparatus after a first phase (Phase I)

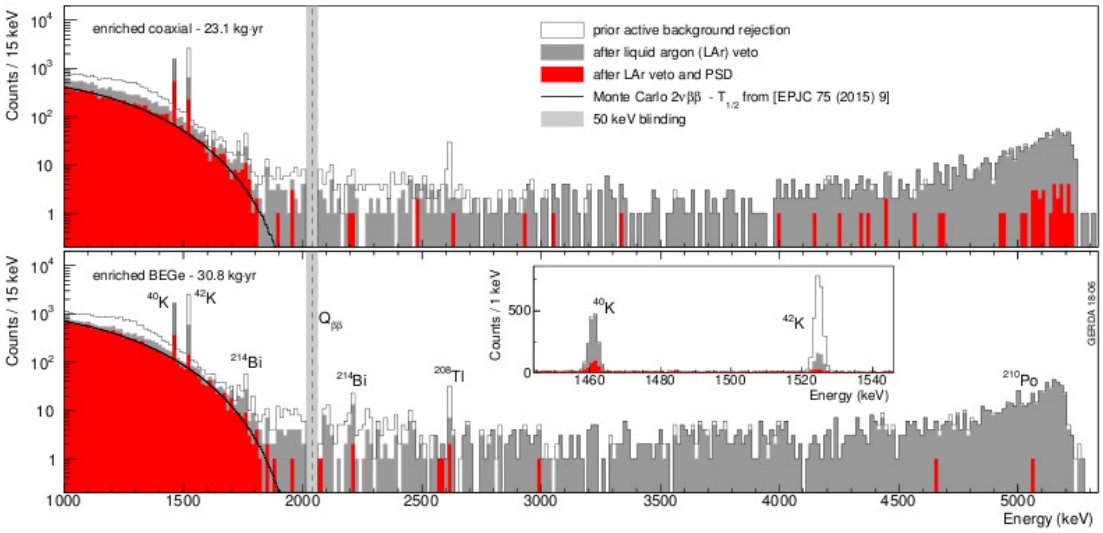

Figure 1: Energy spectra of Phase II data before any cuts (open histogram), after the LAr cut (grey histogram) and then after also the PSD cut (red histogram) for coaxial (top panel) and BEGe (bottom panel) detectors. The black lines are the expected $2\nu\beta\beta$ spectra from the GERDA publication [3]. The vertical grey band is the ±25 keV blind region at the $Q_{\beta\beta}$ value. The inset in the bottom panel shows the BEGe energy region around the two K lines. Various background components are labelled in the bottom panel. The BEGe detector spectrum covers all Phase II data, that of the coaxial detectors all Phase II except for the first 5 kg·yr

completed in 2013 has been upgraded (Phase II) [2]. The active detector mass contains 15.6 kg of coaxial detectors and 20 kg of detectors of broad energy germanium (BEGe) type, which exhibit a better energy resolution and pulse shape discrimination (PSD) respect to the coaxial ones. The detectors are mounted in a seven string geometry. All around the detectors strings a hybrid LAr veto was mounted consisting of light-guiding TPB coated fibers coupled to SiPMS and two arrays of low radioactivity PMTs. The LAr veto utilizes the scintillation light of the LAr to veto events depositing energy inside the argon.

3 The results

The ongoing Phase II data taking started in December 2015 and up to April 2018 has accumulated an exposure of 58.9 kg·yr: 28.1 kg·yr from coaxial detectors and 30.8 kg·yr from BEGe detectors. Events falling in the energy region of ± 25 keV around the $Q_{\beta\beta}$ are unavailable for data analysis until all the analysis cuts are finalized. Weekly calibrations with ^{228}Th sources ensure a stable energy scale for the entire data taking period. The full-width at half-maximum at $Q_{\beta\beta}$ is on average (3.0 ± 0.1) keV for BEGe and (3.6 ± 0.1) keV for coaxial detectors.

The energy spectra collected with the coaxial and BEGe detectors are shown in Fig. 1. Two lines are visible at 1460.8 keV and 1524.6 keV which are due to the decays of ^{40}K and ^{42}K, respectively. Except for these two lines the spectra are dominated in the region below the $Q_{\beta\beta}$ of the ^{76}Ge by the continuum spectrum of the $2\nu\beta\beta$ decay. The high energy part of the

spectrum (above roughly 3500 keV) is due to alpha decays - mainly ^{210}Po - on the thin p^+ contact and groove of the detectors. Their observed energy is degraded due to the very short range of alpha particles. The application of the LAr veto cut (grey histogram) and then of the PSD cut (red histogram) is also shown in Fig. 1.

The inset in the bottom panel shows the two K lines. The LAr veto cut is effective to reduce the ^{42}K line because the β particles of this $\beta - \gamma$ cascade can release up to 2 MeV in the LAr. The ^{40}K line is not affected because it originates from an electron capture in which no energy deposition is released in the LAr. From the monitoring of the ^{40}K line and from the analysis of random triggers a signal acceptance for $0\nu\beta\beta$ events due to the operation of the LAr veto is estimated to be $(97.7 \pm 0.1)\%$.

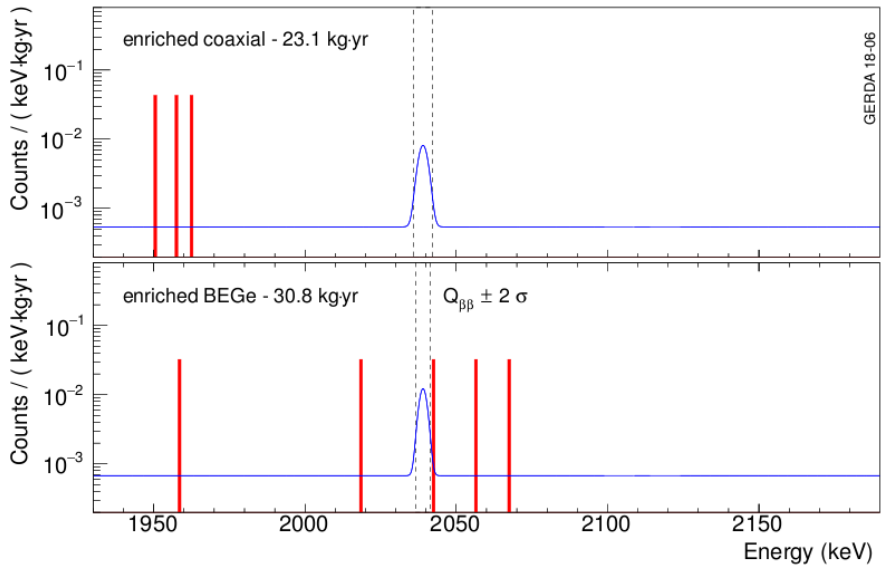

Figure 2: Energy spectra of the coaxial and BEGe detectors in the analysis window. The BEGe detector spectrum covers all Phase II data, that of the coaxial detectors all Phase II except for the first 5 kg·yr. The blue lines show the hypothetical $0\nu\beta\beta$ signal for $T_{1/2} = 0.9{\cdot}10^{26}$ yr residing on the respective constant backgrounds. The statistical fit is performed on a 240 keV wide energy window from 1960 to 2190 keV excluding the $\pm$ 5 keV at the known gamma lines at 2104 keV and 2119 keV, but including the energy region of $\pm$ 5 keV at $Q_{\beta\beta}$.

Signal events deposit their energy in a restricted region of the detectors (single-site events, SSEs), while background events have often multiple energy depositions (multi-site events, MSEs) or occur at the detector surface. The rejection of background events can be done through PSD. MSEs are rejected by a neural network algorithm for the coaxial detectors, and by a simple mono-parametric method for the BEGe detectors [4]. The latter is based on the amplitude of the maximum current pulse divided by the energy of the signal recorded in a BEGe detector. For SSEs this ratio assumes a fixed value independent of where the decay happens, for MSEs and for electrons in the n^+ contact the ratio assumes values lower than that for SSEs, while for events on the groove and p^+ contact the value of the ratio is higher than for SSEs. With a two sided cut MSEs and surface events are so rejected. The alpha events in coaxial

detectors are effectively rejected with a new PSD approach based on the charge collection time [5]. The signal acceptance for PSD is (71.2 ± 4.3)% for coaxial and (87.6 ± 2.5)% for BEGe detectors.

Figure 2 shows the energy spectrum from 1930 keV to 2190 keV after all analysis cuts. The background index evaluated from the events in such plots gives $(5.6^{+3.4}_{-2.4} \cdot 10^{-4})$ cts/(keV·kg·yr) for the BEGe detectors and $(5.7^{+4.1}_{-2.6} \cdot 10^{-4})$ cts/(keV·kg·yr) for the coaxial detectors. These are the lowest background indices obtained up to now respect to all other $0\nu\beta\beta$ experiments in the world if the energy resolution is taken into account. The $0\nu\beta\beta$ analysis is done using an unbinned maximum likelihood fit assuming a Gaussian signal over a flat background. All the data collected in Phase I and Phase II are used for a total exposure of 82.4 kg·yr. A null signal maximizes the likelihood fit. Confidence intervals are evaluated both in the frequentist and Bayesian approach. The frequentist confidence interval taking into account also the systematic uncertainties corresponds to $T_{1/2} > 0.9 \cdot 10^{26}$ yr (90% C.L.) while the median sensitivity is $T_{1/2} = 1.1 \cdot 10^{26}$ yr (90% C.L.). GERDA is the first experiment to surpass 10^{26} yr sensitivity.

4 Conclusions

GERDA Phase II has worked smoothly and with high efficiency since December 2015. In Phase II it has collected 58.9 kg·yr of really good data. With the present data release no signal events were detected and a lower limit of $T_{1/2} > 0.9 \cdot 10^{26}$ yr (90% C.L.) of the $0\nu\beta\beta$ decay of ^{76}Ge has been obtained. A median sensitivity of $T_{1/2} = 1.1 \cdot 10^{26}$ yr (90% C.L.) has been reached, which is the best in the world. The background level in the range of interest is the lowest respect to experiments using other isotopes. Based on these achievements the recently formed LEGEND collaboration is planning a ton-scale ^{76}Ge experiment with the aim to explore half-lives up to 10^{27}yr and more. A first stage it will be the deployment of up to 200 kg of enriched ^{76}Ge detectors inside the GERDA cryostat (LEGEND-200) [6] at LNGS.

References

[1] M. Agostini *et al.*, "The GERDA experiment for the search of $0\nu\beta\beta$ decay in ^{76}Ge," Eur. Phys. J. C **73**, no. 3, 2330 (2013). doi 10.1140/epjc/s10052-013-2330-0 [arXiv:1212.4067 [physics.ins-det]].

[2] M. Agostini *et al.*, "Upgrade for Phase II of the GERDA experiment," Eur. Phys. J. C **78**, no. 5, 388 (2018). doi: 10.1140/epjc/s10052-018-5812-2 [arXiv:1711.01452 [physics.ins-det]].

[3] M. Agostini *et al.*, "Results on $\beta\beta$ decay with emission of two neutrinos or majorons in ^{76}Ge from GERDA phase I," Eur. Phys. J. C **75**, 416 (2015). doi: 10.1140/epjc/s10052-015-3627-y [arXiv:1501.02345 [nuc-ex]].

[4] M. Agostini *et al.*, "Pulse shape discrimination for GERDA Phase I data," Eur. Phys. J. C **73**, 2583 (2013). doi 10.1140/epjc/s10052-013-2583-7 [arXiv:1307.2610 [physics.ins-det]].

[5] A. Zsigmond, "New results from GERDA Phase II," Talk at XXVIII International Conference on Neutrino Physics and Astrophysics, 4-9 June 2018, Heidelberg, Germany, DOI: 10.5281/zenodo.1287603, URL: https://doi.org/10.5281/zenodo.1287603.

[6] N. Abgrall *et al.*, "The Large Enriched Germanium Experiment for Neutrinoless Double-Beta Decay (LEGEND)," AIP Conf. Proc. **1894**, 020027 (2017). doi: 10.1063/1.5007652 [arXiv:1709.01980 [physics.ins-det]].

Axion Monodromy Dark Matter and Fluctuations

Jürgen Berges, Aleksandr Chatrchyan[*], *Joerg Jaeckel*

Institut für theoretische Physik, Universität Heidelberg,
Philosophenweg 16, 69120 Heidelberg, Germany

DOI: http://dx.doi.org/10.3204/DESY-PROC-2018-03/Chatrchyan_Aleksandr

We study the production of axion-like particles (ALP) in the presence of monodromy, via the misalignment mechanism. We show how instabilities can trigger the growth of fluctuations. An analysis of the subsequent nonperturbative dynamics is performed. We discuss the deviations from a matter-like equation of state and explain how ALPs with a monodromy can behave as cold dark matter. These proceedings are based on [1].

1 Introduction

Axion-like particles (ALP), produced via the misalignment mechanism are interesting candidates for cold dark matter, both from the theoretical as well as the experimental perspective [2]. ALPs enjoy a discrete shift symmetry, $\varphi \to \varphi + 2\pi f$, where f is the axion decay constant. The potential of ALPs can be typically parametrized as $U(\varphi) = \Lambda^4[1 - \cos(\varphi/f)]$.

Recently, interest has grown towards ALPs with an explicitly broken discrete shift symmetry. Such ALPs are said to exhibit a monodromy. Several mechanisms are known for realizing monodromy for string axions, mostly discussed in the context of large-field inflation [3, 4]. Implications for ALP dark matter were considered recently by [5]. It was shown that the presence of monodromy extends the range of viable models towards larger experimentally more accessible couplings. At the same time the structure of the potential with many non-degenerate local minima results in a non-trivial time evolution and a growth of fluctuations during the vacuum realignment, which is discussed in this contribution.

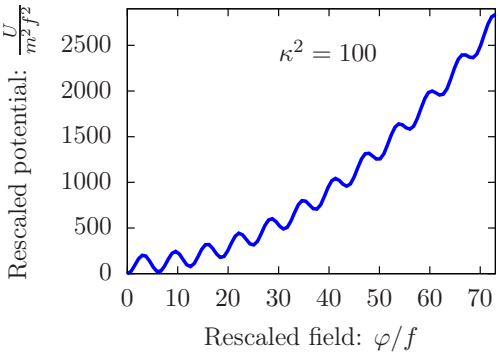

Figure 1: The rescaled potential $x^2/2 + \kappa^2(1 - \cos x)$ for $\kappa^2 = 100$.

We have considered the case of breaking with a quadratic monomial, which corresponds to the massive Sine-Gordon model. The classical potential can be written as,

$$U(\varphi) = \frac{1}{2}m^2\varphi^2 + \Lambda^4\Big(1 - \cos\frac{\varphi}{f}\Big). \tag{1}$$

[*]Talk given by Aleksandr Chatrchyan: chatrchyan@thphys.uni-heidelberg.de

In principle, an arbitrary phase parameter can be included in the argument of the cosine. We set it to zero for simplicity, so that the potential is $\mathbb{Z}_2$-symmetric and has a global minimum at $\varphi = 0$. The potential is shown in Fig. 1 for a particular value of $\kappa^2 = \Lambda^4/(m^2 f^2) = 100$. All self-couplings in (1) are suppressed by powers of f. Alternatively, their strength can be characterized by the dimensionless parameter λ, defined as $\lambda = \Lambda^4/f^4 = (\kappa m)^2/f^2$, which coincides with the quartic coupling from the Taylor expansion of (1) around $\varphi = 0$.

2 Vacuum realignment and instabilities

In the simplest case of the misalignment mechanism, the axion-like field is present already during inflation [2]. The classical equations of motion in an expanding universe have the form

$$\ddot{\varphi} + 3H\dot{\varphi} - \frac{\Delta\varphi}{a^2} + \frac{\delta U}{\delta\varphi} = 0,$$

where $a = a(t)$ is the scale factor, $H = \dot{a}/a$ is the Hubble parameter and co-moving coordinates are used. The field is initially over-damped and obtains some value ϕ_1 after inflation, practically homogeneous throughout the observable universe. It starts to oscillate once the Hubble friction term becomes comparable to the potential term in the equations of motion.

In the presence of background oscillations, fluctuations are subject to parametric resonance instability [5], which leads to an exponential growth of fluctuations with resonant momenta. We have extracted the growth exponents by neglecting the expansion of the universe (setting $a = 1$), solving numerically the linearized equations of motion for the fluctuations in momentum space [6, 5], valid at early times, along with the classical equation for the background field $\phi(t)$, with the initial conditions $\phi(t_0) = \phi_0$ and $\partial_t\phi(t_0) = 0$ (see also [5]). In Fig. 2 the extracted exponent μ is plotted against the momentum p/m and ϕ_0/f for the case of $\kappa^2 = 100$. Depending on the value of ϕ_0/f there is either one wide, or multiple narrow instability bands. The first case corresponds to background oscillations within one local minimum, whereas in the second case the field oscillates over several local minima around $\phi = 0$.

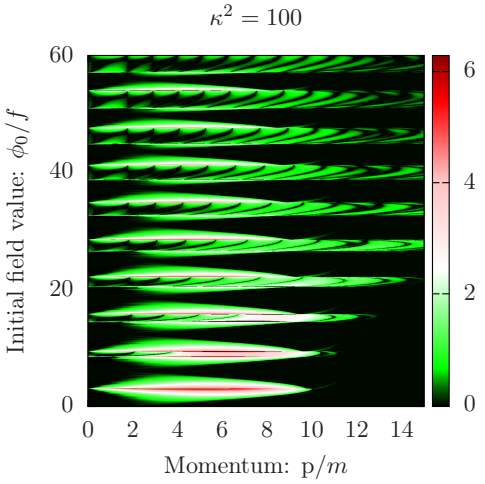

Figure 2: The growth exponent μ/m, characterizing the parametric resonance instability, for $\kappa^2 = 100$. The dark regions correspond to stable modes.

The oscillation amplitude of ϕ decreases with time, if expansion is taken into account. Moreover, physical momenta get redshifted. As a result, each co-moving momentum mode flows with time along a certain trajectory in Fig. 2. For small values of ϕ_1/f, the background field after a couple of oscillations explores the almost quadratic region of the potential, with $\mu \approx 0$. The fluctuations thus do not grow sufficiently and the field behaves exactly as ordinary matter. This is the case for standard ALPs, for which the constraint

$\phi_1/f < \pi$ holds. In the case of large values of ϕ_1/f, the field can spend more time in the region of the potential with strong instability bands and fluctuations will get amplified accordingly.

As the fluctuations grow, nonlinear corrections eventually become important. In particular, when the energy in the fluctuations becomes parametrically $\mathcal{O}(\lambda^{-1/2})$, secondary instabilities set in (see [6]). They correspond to re-scattering of the produced fluctuations and result in a broader and smoother spectrum in momentum space.

3 Strong fluctuations: equation of state

After some time the energy in the fluctuations becomes parametrically $\mathcal{O}(\lambda^{-1})$. This is when the dynamics becomes nonperturbative. Our main tool for studying the dynamics of this stage were the classical-statistical lattice simulations [7], similar to [8].

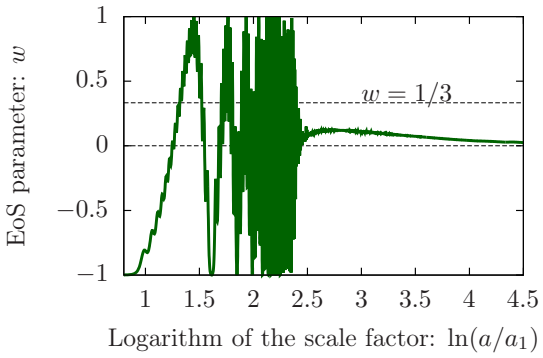

Figure 3: Equation of state parameter as a function of the logarithm of the scale factor $\ln(a/a_1)$.

The background field performs oscillations with a gradually decreasing amplitude. This decrease is both due to expansion, as well as due to the energy transfer to the fluctuations. Once the oscillations occur within one local minimum, $\phi/f \sim \mathcal{O}(\pi)$, the decrease becomes rapid. This is when the attractive nature of the leading self-interactions becomes important. It leads to the fragmentation of the background field [9, 10].

In the most cases the field finds itself in the lowest minimum after the background oscillations die out. It is however also possible that the field settles in one of the false minima. In that case some fraction of the energy is transformed into the form of dark energy [11]. The presence of strong fluctuations has the effect of smearing the wiggles in the effective potential, making it less likely to get trapped in a false minimum.

After the fragmentation of the background field, energy continues to be transferred to higher, previously unoccupied momenta. In the absence of expansion, most of the energy is stored after some time in ultra-relativistic modes, with $\omega_{\mathbf{p}} \approx \mathrm{p}$. The transfer occurs via a self-similar direct cascade that the mode occupancies exhibit at high momenta [12] i.e. the particle momentum distribution function $n(t, \mathrm{p})$ evolves as,

$$n(t,\mathrm{p}) = \Big(\frac{t}{t_S}\Big)^{\alpha} n\Big(t_S, \Big(\frac{t}{t_S}\Big)^{\beta}\mathrm{p}\Big) = \Big(\frac{t}{t_S}\Big)^{\alpha} n_S\Big(\Big(\frac{t}{t_S}\Big)^{\beta}\mathrm{p}\Big),$$

where $n_S(\mathrm{p})$ is the distribution function at some reference time t_S and α and β are real scaling exponents. The above form reflects the system being in the vicinity of a nonthermal fixed point, an attractor solution on the way towards thermal equilibrium (see e.g. [7]).

The numerically extracted ratio of the exponents quickly approaches $\alpha/\beta = 4$, which reflects the conservation of energy (in $3+1$ dimensions). The value of the exponent $\beta \approx -1/5$ is approached comparably slower. This exponent determines the speed of the cascade i.e. the

characteristic momentum scale evolves as $\mathrm{p}_{\mathrm{char}}(t) \sim t^{-\beta}$. Self-similar dynamics of the cascade was studied analytically in [12] with the help of wave kinetic theory of turbulence.

The cascade shifts the equation of state parameter towards $w \to 1/3$. On the other hand, all momenta are red-shifted in the presence of expansion, in a radiation-dominated universe according to $\mathrm{p} \sim t^{-1/2}$. Therefore, typical momenta become non-relativistic again after some time. This is demonstrated in Fig. 3, where we plotted the numerically extracted equation of state parameter w as a function of $\ln(a/a_1)$, with a_1 being the scale factor at the start of oscillations, for the case of ALPs with $\kappa^2 = 100$, $\phi_0/f = 100$, $f = 10^9$GeV and $m_a = \Lambda^2/f = \kappa m = 1$eV. For simplicity we have included only standard vacuum quantum fluctuations in the initial conditions. The oscillations of w around zero at early times are due to the oscillating background field. Already at $\ln(a/a_1) \approx 5$, which corresponds to $H \approx 10^{-4}$eV, w becomes approximately zero. The field behaves as cold dark matter if $w \approx 0$ happens before matter-radiation equality at $H_{\mathrm{eq}} = 1.8 \times 10^{-27}$eV.

4 Conclusion

The presence of monodromy for ALPs, in addition to extending the range of viable dark matter models, can lead to strong fluctuations in the axion-like field. These fluctuations play an important role for structure formation and, in particular, they can lead to the formation of miniclusters [13]. More details on our analysis, as well as the allowed parameter space and phenomenological implications will be provided in an upcoming publication [1].

Acknowledgments

We gratefully acknowledge support by the DFG TransRegio research collaborative TR33 “The Dark Universe”. Some of the numerical calculations were performed on the computational resource bwUniCluster, funded by the Ministry of Science, Research and the Arts Baden-Württemberg and the Universities of the State of Baden-Württemberg, within the framework program Baden-Württemberg high performance computing (bwHPC).

References

[1] J. Berges, A. Chatrchyan, and J. Jaeckel, in preparation.

[2] P. Arias *et al.*, JCAP **1206**, 013 (2012), arXiv:1201.5902.

[3] L. McAllister, E. Silverstein, and A. Westphal, Phys. Rev. **D82**, 046003 (2010), arXiv:0808.0706.

[4] E. Silverstein and A. Westphal, Phys. Rev. **D78**, 106003 (2008), arXiv:0803.3085.

[5] J. Jaeckel, V. M. Mehta, and L. T. Witkowski, JCAP **1701**, 036 (2017), arXiv:1605.01367.

[6] J. Berges and J. Serreau, Phys. Rev. Lett. **91**, 111601 (2003), arXiv:hep-ph/0208070.

[7] J. Berges, (2015), arXiv:1503.02907.

[8] G. N. Felder, Comput. Phys. Commun. **179**, 604 (2008), arXiv:0712.0813.

[9] J. Berges, K. Boguslavski, A. Chatrchyan, and J. Jaeckel, Phys. Rev. **D96**, 076020 (2017), arXiv:1707.07696.

[10] M. A. Amin, R. Easther, and H. Finkel, JCAP **1012**, 001 (2010), arXiv:1009.2505.

[11] T. Kobayashi and P. G. Ferreira, Phys. Rev. **D97**, 121301 (2018), arXiv:1801.09658.

[12] R. Micha and I. I. Tkachev, Phys. Rev. **D70**, 043538 (2004), arXiv:hep-ph/0403101.

[13] C. J. Hogan and M. J. Rees, Phys. Lett. **B205**, 228 (1988).

SMASH-ing Vacuum Metastability

C.R. Das[1], *Katri Huitu*[2] *and Timo J. Kärkkäinen*[2]

[1]Bogoliubov Laboratory of Theoretical Physics, Joint Institute of Nuclear Research, Joliot-Curie 6, 141980 Dubna, Moscow region, Russian Federation
[2]Department of Physics and Helsinki Institute of Physics, P. O. Box 64, FI-00014 University of Helsinki, Finland

DOI: http://dx.doi.org/10.3204/DESY-PROC-2018-03/Das_Chittaranjan

Five fundamental problems - neutrino oscillations, baryogenesis, dark matter, inflation, strong CP problem - are solved at one stroke in "SM-A-S-H" (Standard Model-Axion-Seesaw-Higgs portal inflation) model by Andreas Ringwald et. al. The Standard Model (SM) particle content was extended by three right-handed SM-singlet neutrinos N_i, a vector-like color triplet quark Q, a complex SM-singlet scalar field σ that stabilises the Higgs potential, all of them being charged under a global lepton number (hyper-charge) and Peccei-Quinn (PQ) $U(1)$ symmetry. We found numerically that SMASH model not only solves five fundamental problems but also the sixth problem "Vacuum Metastability" through the extended scalar sector.

1 Introduction

It is well-known that the Standard Model (SM) Higgs potential is metastable [1], as the sign of the quartic coupling λ_H turns negative at instability scale around $\Lambda_{IS} \sim 10^{11}$ GeV. The largest uncertainties of SM vacuum stability are driven by both the top quark pole mass and the mass of SM Higgs boson. Experimental current data is in significant tension with the stability hypothesis, making it more likely that the universe is in a metastable vacuum state. The expected lifetime of vacuum decay to a true vacuum is extraordinarily long, and it is unlikely to affect the evolution of the universe. However, it is unclear why the vacuum state entered to metastable or unstable vacuum, to begin with during the early universe.

It is possible that at or below the instability scale heavy degrees of freedom originating from a theory beyond the SM start to alter the running of the SM parameters of renormalization group equations (RGE). This approach aims to solve the vacuum metastability problem by proving that the universe is currently in a stable vacuum. One theory candidate is a complex singlet σ extended SM. The scalar sector of such a theory may stabilise the theory with a threshold mechanism [2, 3]. The effective SM Higgs coupling gains a positive correction $\delta \equiv \lambda_{H\sigma}^2/\lambda\sigma$ at m_σ, where $\lambda_{H\sigma}$ is the Higgs doublet-singlet portal coupling and λ_σ is the quartic coupling of σ.

This threshold mechanism is embedded in a recent SMASH [4, 5] theory, which utilizes it at $\lambda_{H\sigma} \sim -10^{-6}$ and $\lambda_\sigma \sim 10^{-10}$, where the vacuum expectation value $v_\sigma \sim 10^{11}$ GeV breaks the lepton number and the Peccei-Quinn symmetry simultaneously. The SMASH framework [4, 5] expands the scalar sector of the SM by introducing a complex singlet field σ.

2 Threshold correction

Consider an energy scale below $m_\sigma < \Lambda_{IS}$, where the heavy scalar σ is integrated out. The low-energy Higgs potential should match the SM Higgs potential:

$$V(H) = \lambda_H^{SM}\left(H^\dagger H - \frac{v^2}{2}\right)^2. \tag{1}$$

It turns out that the quartic coupling which we measure has an additional term:

$$\lambda_H^{SM} = \lambda_H - \frac{\lambda_{H\sigma}^2}{\lambda_\sigma}. \tag{2}$$

Since the SM quartic coupling will be approximately -0.08 at M_P, the threshold correction

$$\delta \equiv \frac{\lambda_{H\sigma}^2}{\lambda_\sigma}, \tag{3}$$

should be large enough to push the high-energy counterpart λ_H to positive value all the way up to M_P. In the literature there are two possible ways of implementing this threshold mechanism.

One may start by solving the SM RGE's up to m_σ, from where the SMASH effect kicks in, and the quartic coupling λ_H gains a sudden increment by δ. Continuation of RGE analysis then requires utilizing SMASH RGE's up to the Planck scale, $M_P = 1.22 \times 10^{19}$ GeV.

Another way is to solve the SMASH RGE's from the SM scale, not bothering to solve the low-energy SM RGE's at all. We gave both examples in Fig.1 and 2. In Fig.3 we have shown how the current experimental values of $m_t = 172.44 \pm 0.60$ GeV and $m_H = 125.09 \pm 0.32$ GeV are staying within the stability region due to the $\lambda_{H\sigma} \sim -10^{-6}$.

3 Choice of $\lambda_{H\sigma}$

To avoid the overproduction of dark radiation via the cosmic axion background, we choose $\lambda_{H\sigma} < 0$. To obtain the observed matter-antimatter asymmetry via leptogenesis, a hierarchy on heavy Majorana neutrinos N_i is required. This is achieved by assigning $Y_n = y_N \times diag(1, 2, 2.1)$, where Y_N and y_N are right-handed and left-handed neutrino Yukawa matrices respectively.

4 Conclusions

1. SMASH unifies axions, seesaw and extended Higgs sector on one energy scale, $\mu \sim 10^{10}$ – 10^{11} GeV, solving several problems badgering the Standard Model in one go.

2. SM vacuum is metastable, since λ_H turns negative around $\mu \simeq 10^{12}$ GeV, SMASH can fix this vacuum metastability problem with $\lambda_{H\sigma} \gtrsim -10^{-5}$ at two-loop RGE level.

3. Also, SMASH shows atmospheric neutrino mass splitting is around 0.05 eV and solar neutrino mass splitting is around 0.009 eV.

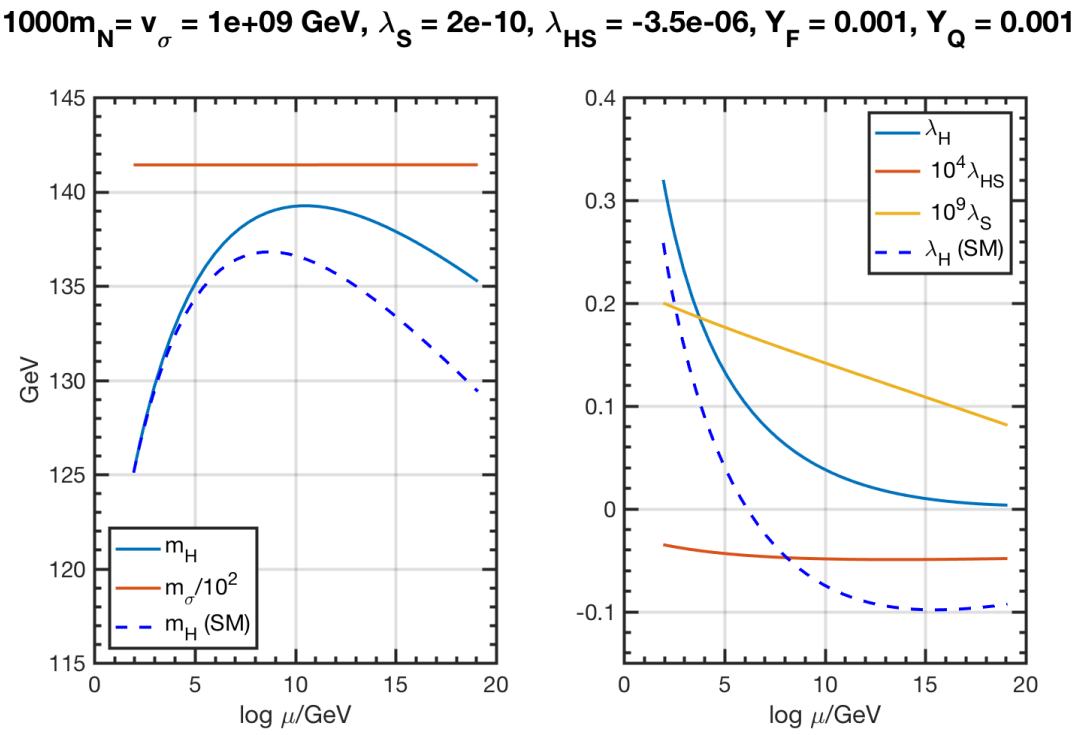

Figure 1: Running of Higgs, σ bare mass and scalar potential parameters with benchmark point. Threshold applied from the beginning at m_Z.

References

[1] S. Alekhin *et al.*, "The top quark and Higgs boson masses and the stability of the electroweak vacuum," Phys. Lett. B **716**, 214 (2012) doi:10.1016/j.physletb.2012.08.024 [arXiv:1207.0980 [hep-ph]].

[2] J. Elias-Miro *et al.*, "Stabilization of the Electroweak Vacuum by a Scalar Threshold Effect," JHEP **1206**, 031 (2012) doi:10.1007/JHEP06(2012)031 [arXiv:1203.0237 [hep-ph]].

[3] O. Lebedev *et al.*, "On Stability of the Electroweak Vacuum and the Higgs Portal," Eur. Phys. J. **C72**, 2058 (2012) doi:10.1140/epjc/s10052-012-2058-2 [arXiv:1203.0156 [hep-ph]].

[4] G. Ballesteros *et al.*, "Standard Model–axion–seesaw–Higgs portal inflation. Five problems of particle physics and cosmology solved in one stroke," JCAP **1708**, 001 (2017) doi:10.1088/1475-7516/2017/08/001 [arXiv:1610.01639 [hep-ph]].

[5] G. Ballesteros *et al.*, "Unifying inflation with the axion, dark matter, baryogenesis and the seesaw mechanism," Phys. Rev. Lett. **118**, 071802 (2017) doi:10.1103/PhysRevLett.118.071802 [arXiv:1608.05414 [hep-ph]].

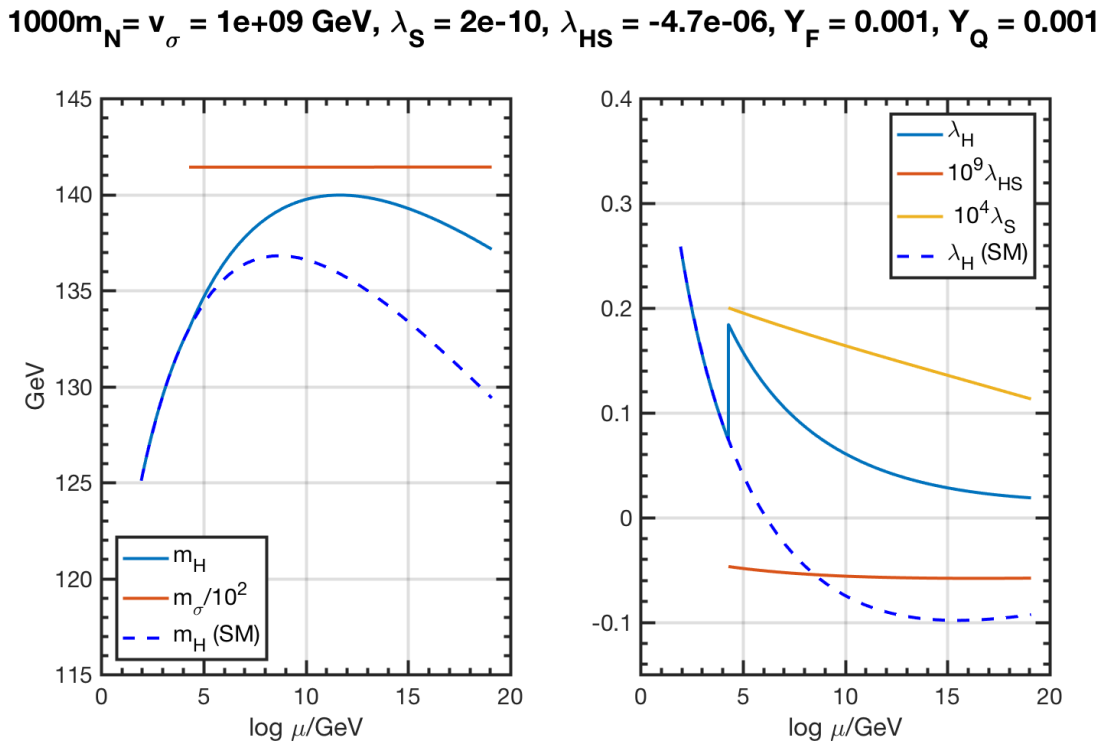

Figure 2: Running of Higgs, σ bare mass and scalar potential parameters with benchmark point. Threshold correction utilized at m_ρ.

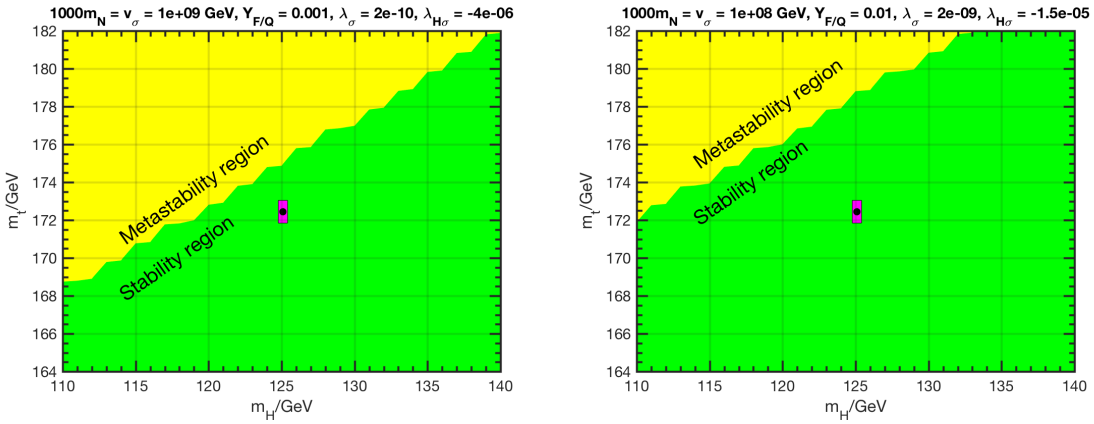

Figure 3: Scalar potential vacuum stability regions for $\lambda_{H\sigma} \approx -10^{-5}$ in (m_H, m_t) plane.

First results from NA62

Babette Döbrich[1]*

[1]CERN, CH-1211 Geneva 23

DOI: http://dx.doi.org/10.3204/DESY-PROC-2018-03/Dobrich_Babette

We discuss first results of the search for $K^+ \to \pi^+\nu\bar{\nu}$ from the 2016 data set of NA62. Standard model sensitivity is shown to be achieved. The experiment continued to take data in 2017 and 2018 and this data is currently under investigation. In addition, NA62 performs various searches for BSM particles which are sketched in this contribution.

1 NA62 and $K^+ \to \pi^+\nu\bar{\nu}$

The NA62 experiment has been built to achieve at a precise measurement of the rare decay $K^+ \to \pi^+\nu\bar{\nu}$. The SM branching ratio of this decay is extremely small [1], but can be predicted with high precision: $(K \to \pi\nu\bar{\nu}) = (8.4 \pm 1.0) \times 10^{-11}$. To achieve its goal, NA62 is equipped with a hermetic detector system, cf. fig. 1 and achieves a $\mathcal{O}(100)$ps timing resolution.

After a commissioning phase, NA62 is taking quality data towards the measurement of $K^+ \to \pi^+\nu\bar{\nu}$ since 2016. NA62 will pause with the pause of the CERN accelerator infrastructure in 2019/2020. Restart of the experiment is expected in 2021 for 'Run3'.

The hadron beam for NA62 is produced via CERN's SPS primary 400 GeV proton beam which interacts in an upstream target (at 0m in fig. 1). An achromat selects a 75 GeV unsepa-

*On behalf of the NA62 Collaboration: R. Aliberti, F. Ambrosino, R. Ammendola, B. Angelucci, A. Antonelli, G. Anzivino, R. Arcidiacono, M. Barbanera, A. Biagioni, L. Bician, C. Biino, A. Bizzeti, T. Blazek, B. Bloch-Devaux, V. Bonaiuto, M. Boretto, M. Bragadireanu, D. Britton, F. Brizioli, M.B. Brunetti, D. Bryman, F. Bucci, T. Capussela, A. Ceccucci, P. Cenci, V. Cerny, C. Cerri, B. Checcucci, A. Conovaloff, P. Cooper, E. Cortina Gil, M. Corvino, F. Costantini, A. Cotta Ramusino, D. Coward, G. D'Agostini, J. Dainton, P. Dalpiaz, H. Danielsson, N. De Simone, D. Di Filippo, L. Di Lella, N. Doble, B. Dobrich, F. Duval, V. Duk, J. Engelfried, T. Enik, N. Estrada-Tristan, V. Falaleev, R. Fantechi, V. Fascianelli, L. Federici, S. Fedotov, A. Filippi, M. Fiorini, J. Fry, J. Fu, A. Fucci, L. Fulton, E. Gamberini, L. Gatignon, G. Georgiev, S. Ghinescu, A. Gianoli, M. Giorgi, S. Giudici, F. Gonnella, E. Goudzovski, C. Graham, R. Guida, E. Gushchin, F. Hahn, H. Heath, T. Husek, O. Hutanu, D. Hutchcroft, L. Iacobuzio, E. Iacopini, E. Imbergamo, B. Jenninger, K. Kampf, V. Kekelidze, S. Kholodenko, G. Khoriauli, A. Khotyantsev, A. Kleimenova, A. Korotkova, M. Koval, V. Kozhuharov, Z. Kucerova, Y. Kudenko, J. Kunze, V. Kurochka, V.Kurshetsov, G. Lanfranchi, G. Lamanna, G. Latino, P. Laycock, C. Lazzeroni, M. Lenti, G. Lehmann Miotto, E. Leonardi, P. Lichard, L. Litov, R. Lollini, D. Lomidze, A. Lonardo, P. Lubrano, M. Lupi, N. Lurkin, D. Madigozhin, I. Mannelli, G. Mannocchi, A. Mapelli, F. Marchetto, R. Marchevski, S. Martellotti, P. Massarotti, K. Massri, E. Maurice, M. Medvedeva, A. Mefodev, E. Menichetti, E. Migliore, E. Minucci, M. Mirra, M. Misheva, N. Molokanova, M. Moulson, S. Movchan, M. Napolitano, I. Neri, F. Newson, A. Norton, M. Noy, T. Numao, V. Obraztsov, A. Ostankov, S. Padolski, R. Page, V. Palladino, C. Parkinson, E. Pedreschi, M. Pepe, M. Perrin-Terrin, L. Peruzzo, P. Petrov, F. Petrucci, R. Piandani, M. Piccini, J. Pinzino, I. Polenkevich, L. Pontisso, Yu. Potrebenikov, D. Protopopescu, M. Raggi, A. Romano, P. Rubin, G. Ruggiero, V. Ryjov, A. Salamon, C. Santoni, G. Saracino, F. Sargeni, V. Semenov, A. Sergi, A. Shaikhiev, S. Shkarovskiy, D. Soldi, V. Sougonyaev, M. Sozzi, T. Spadaro, F. Spinella, A. Sturgess, J. Swallow, S. Trilov, P. Valente, B. Velghe, S. Venditti, P. Vicini, R. Volpe, M. Vormstein, H. Wahl, R. Wanke, B. Wrona, O. Yushchenko, M. Zamkovsky, A. Zinchenko

rated secondary beam (containing around 6 % Kaons) for NA62, around 23m downstream the target. This beam is guided into the experimental hall at CERN's Prevessin site, with the first detector (KTAG) located at around 70 m.

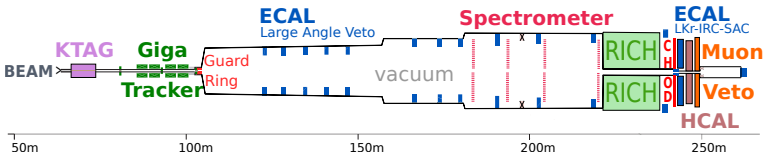

Figure 1: Layout of NA62. See [2] for details on the detector.

In Fig. 1, the Giga Tracker, GTK in short (Si-pixel), and the STRAWs are two trackers that allow to determine the 3-momentum of the incident beam particles and their decay products, respectively. The GTK data is time-matched with the KTAG (differential Cerenkov counter) to obtain the full Kaon 4-momentum. The CHANTI station ("guard ring" in the figure) provides a veto against inelastic interactions of the 75 GeV beam in the third GTK tracker-station. A RICH positively identifies charged pions from K^+ decays. Hadron ID is provided by the calorimeters MUV1 and MUV2 (HCAL in the figure). As further veto, the MUV3 plastic scintillator detector ("muon veto" in the figure), placed after an iron absorber, is used to identify muons. Finally, photons can be vetoed at small angles by IRC and SAC, at intermediate angles by the liquid krypton calorimeter (LKr). This veto system is denoted as ECAL in the figure at $\sim$ 241m. At the largest angles, photons are detected by the lead-glass large-angle-veto (LAV) calorimeters.

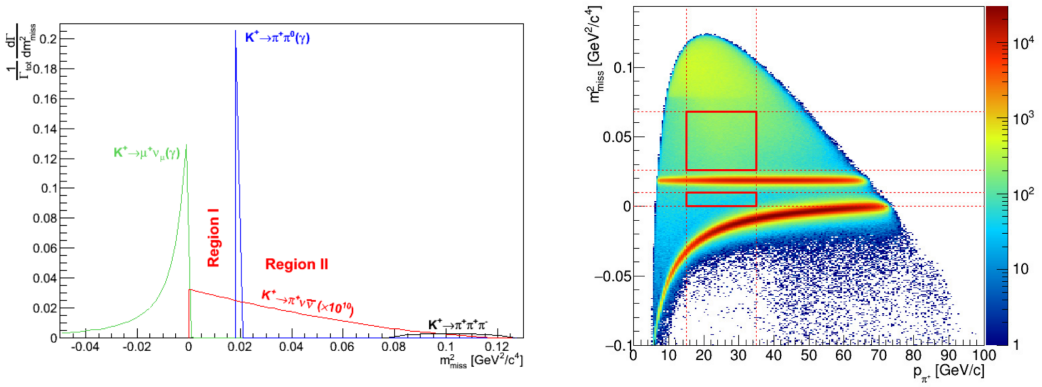

Figure 2: Left panel: m^2_{miss} for main decay channels and for $K^+ \to \pi^+\nu\bar{\nu}$ (the latter being scaled by 10^{10}). Right: Data (minimum bias, one-track selection), m^2_{miss} as function of track momentum with π^+ mass hypothesis. The kinematic boxes of the 2 signal regions are indicated in red: The secondary track momentum must be in between 15GeV and 35GeV.

First results of the analysis of the 2016 data set w.r.t. the decay $K^+ \to \pi^+\nu\bar{\nu}$ are discussed in the following.

The signal selection proceeds as follows: A charged kaon of the hadron beam must be

matched in space and time with a downstream pion. The crucial kinematic variable is the squared missing mass: $m^2_{\rm miss} = (P_K - P_\pi)^2$. The shape of the respective main kaon decay mode in the $m^2_{\rm miss}$ variable yield two natural signal regions for the search of $K^+ \to \pi^+\nu\bar{\nu}$, away from the central peak of $K^+ \to \pi^+\pi^0$, cf. fig. 2. To ameliorate background from Gaussian tails, the signal regions R1 and R2 are $\sim 10\sigma$ away from $K^+ \to \pi^+\pi^0$ and $K^+ \to \mu^+\nu$. Computing $m^2_{\rm miss}$ through the nominal Kaon momentum or taking the Pion momentum from the RICH instead of the STRAWs provides an additional handle on background rejection since it provides a handle against mis-reconstruction in STRAW and GTK.

K^+ and π^+ (through RICH and calorimeters) must be positively identified and photon and multi-track rejections are applied. The π^+ momentum is restricted to be $15 < |\vec{p}_{\pi^+}| < 35$ GeV as this facilitates the vetoing of π^0. The achieved detection inefficiency of π^0 from data is $2.5{\times}10^{-8}$.

The number of Kaons in the 2016-subsample used for the analysis is $(1.21 \pm 0.04) \times 10^{11}$ (measured on control-triggered data). Accounting for a selection acceptance of (4.0±0.1)%, a trigger efficiency of (87±2) % and a random veto loss probability of (76±4) %, the expected number of $K^+ \to \pi^+\nu\bar{\nu}$ signal events is (0.267 ± 0.001 (stat) ± 0.020 (syst) ± 0.032 (ext)), where the external error is due to uncertainties on the SM calculations.

Backgrounds to this search some from charged kaon decays (in and before the decay region) and by beam interactions. Background sources are studied with data driven methods in background regions, and corrected for kinematic and radiative tails. Subsequently, they are extrapolated to control regions as well as signal regions, once the control region extrapolations yield a satisfactory result. A list of expected background contributions is found in fig. 3, right-hand panel.

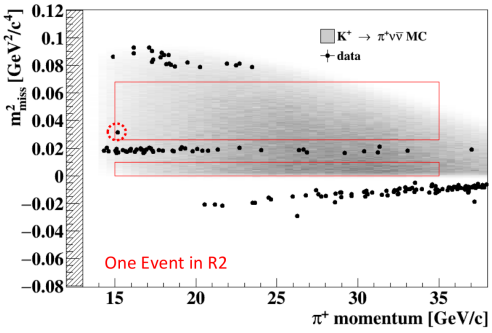

Process	Expected events in signal region
$K^+ \to \pi^+\pi^0(\gamma)$	$0.064 \pm 0.007_{stat} \pm 0.006_{syst}$
$K^+ \to \pi^+\nu(\gamma)$	$0.020 \pm 0.003_{stat} \pm 0.003_{syst}$
$K^+ \to \pi^+\pi^-e^+\nu$	$0.018^{+0.024}_{-0.017}\vert_{stat} \pm 0.009_{syst}$
$K^+ \to \pi^+\pi^+\pi^-$	$0.002 \pm 0.001_{stat} \pm 0.002_{syst}$
Upstream background	$0.050^{+0.090}_{-0.030}\vert_{stat}$
Total	$0.15 \pm 0.09_{stat} \pm 0.01_{syst}$

Figure 3: Left panel: m^2_{miss} as function of π^+ momentum. Data passing the $K^+ \to \pi^+\nu\bar{\nu}$ selection appear in the red boxes. The grey area is the distribution of events for $K^+ \to \pi^+\nu\bar{\nu}$ from MC. One event is observed in the R2 signal box. Right panel: Table of expected background contributions in signal regions.

After unblinding of the signal regions, one candidate event is found in R2 in the 2016 data sub-sample, as shown in fig. 3 (left). This is consistent with the SM expectation (0.267) and with the background expectation. The event has a positive track, with momentum of 15.3 GeV/c and ring in the RICH detector consistent with a π^+ hypothesis. Note that data analyzed here amount to only to a fraction of the total exposure of the NA62 experiment in 2016-2018.

Using the CLs method, the observed upper limit on the $K^+ \to \pi^+\nu\bar{\nu}$ branching ratio

is $\mathrm{BR}(K^+ \to \pi^+\nu\bar{\nu}) < 14 \times 10^{-10}$ at 95 % CL, while the corresponding expected limit is $\mathrm{BR}(K^+ \to \pi^+\nu\bar{\nu}) < 10 \times 10^{-10}$.

This result can be understood as a proof of principle of the decay-in-flight technique adopted by NA62. The experiment has already collected more than 20 times the statistics used here, and the analysis of this larger data sample is ongoing.

2 BSM searches with NA62

Physics beyond the Standard Model (BSM) can show itself at NA62 in many facets. The most obvious possibility that would impact NA62's main analysis is the existence of a non-flavor diagonal QCD axion [3, 4]. If such an axion exists, its signal would lie in R1, and $K^+ \to \pi^+\nu\bar{\nu}$ would constitute a background to it. A search for such events has to account for the two-body kinematics for flavorful axions and possibly differently optimized selection cuts.

Results of new physics searches by NA62 from Kaon decays include a search for Heavy Neutral leptons (2015 data) [5] and invisibly decaying Dark Photons (2016 data) [6].

An additional line of research is pursued by searching of decays of long-lived new particles at MeV-GeV masses. Such particles can be produced in the target region at 0-23m by proton interactions in the collimator or in decays of heavy mesons in that region. In this fashion, BSM ideas of new vector, (pseudo-)scalar or neutrino-like particles can be put to the test in dedicated beam-dump runs or with parasitic triggers during regular data-taking.

Acknowledgments

The author would like to thank the organizers and especially the DESY team for growing and bringing together the axion community with this yearly event. BD is supported by ERC-STG 802836 (AxScale).

References

[1] A. J. Buras, D. Buttazzo, J. Girrbach-Noe and R. Knegjens, JHEP **1511**, 033 (2015) doi:10.1007/JHEP11(2015)033 [arXiv:1503.02693 [hep-ph]].

[2] E. Cortina Gil *et al.* [NA62 Collaboration], JINST **12**, no. 05, P05025 (2017) doi:10.1088/1748-0221/12/05/P05025 [arXiv:1703.08501 [physics.ins-det]].

[3] L. Calibbi et. al., Phys. Rev. D **95**, no. 9, 095009 (2017) doi:10.1103/PhysRevD.95.095009 [arXiv:1612.08040 [hep-ph]].

[4] F. Björkeroth, E. J. Chun and S. F. King, JHEP **1808**, 117 (2018) doi:10.1007/JHEP08(2018)117 [arXiv:1806.00660 [hep-ph]].

[5] E. Cortina Gil *et al.* [NA62 Collaboration], Phys. Lett. B **778**, 137 (2018) doi:10.1016/j.physletb.2018.01.031 [arXiv:1712.00297 [hep-ex]].

[6] NA62 Collaboration, in preparation

The Klash Proposal: Status and Perspectives

C. Gatti[1], *D. Alesini*[1], *D. Babusci*[1],*C. Braggio*[6,7], *G. Carugno*[6,7], *N. Crescini*[5,7], *D. Di Gioacchino*[1], *P. Falferi*[3,4], *G. Lamanna*[2], *C. Ligi*[1], *A. Ortolan*[5], *L. Pellegrino*[1], *A. Rettaroli*[1], *G. Ruoso*[5], *S.Tocci*[1]

[1] INFN, Laboratori Nazionali di Frascati, Italy
[2] Università di Pisa and INFN, Italy
[3]Istituto di Fotonica e Nanotecnologie, CNRFondazione Bruno Kessler, Povo, Trento, Italy
[4]INFN, TIFPA, Povo (TN), Italy
[5]INFN, Laboratori Nazionali di Legnaro, Legnaro (PD), Italy
[6]INFN, Sezione di Padova, Padova, Italy
[7]Dip. di Fisica e Astronomia, Padova, Italy

DOI: http://dx.doi.org/10.3204/DESY-PROC-2018-03/Gatti_Claudio

Recently some of the authors proposed [1] a search for galactic axions with mass about 0.2 μeV using a large volume resonant cavity, tens of cubic meters, cooled down to 4 K and immersed in a magnetic field of about 0.6 T generated inside the superconducting magnet of the KLOE experiment located at the National Laboratory of Frascati of INFN. This experiment, called KLASH (KLoe magnet for Axion SearcH), has a potential sensitivity on the axion-to-photon coupling, $g_{a\gamma\gamma}$, of about 6×10^{-17} GeV^{-1}, reaching the region predicted by KSVZ [2] and DFSZ [3] models of QCD axions. We report here the status of the project.

1 Introduction

The search for galactic-axion with a "Haloscope", a resonant cavity immersed in a strong magnetic field as proposed by P. Sikivie [4], is a well established technique. The power generated by axion conversion in a haloscope is proportional to the product of the stored magnetic energy, the loaded quality factor, Q_L, and the cavity angular frequency ω_c: $P_{\rm sig} \propto \omega_c B^2 V Q_L$. Since cavity volume, V, scales approximately as ω_c^{-3} and the quality factor for a copper cavity at cryogenic temperatures scales as $\omega^{-2/3}$, we have $P_{\rm sig} \propto \omega_c^{-8/3}$ making the research at lower masses advantageous even with a moderate magnetic field B. ADMX [5] probed the QCD-axions in the mass range between 2 and 3 μeV by using a haloscope composed of a resonant cavity with volume 0.2 m^3 and unloaded quality factor about 2×10^5 immersed in a magnetic field of 7.6 T. Lower masses are foreseen, for instance, by models where the Peccey-Quinn symmetry is broken before Inflation. In the following, we show that a search for galactic axions with mass in the range 0.3-1 μeV is possible using a large volume resonant cavity of about 33 m^3 cooled down to 4.5 K and immersed in a magnetic field of 0.6 T generated inside the superconducting magnet of the KLOE experiment located at the National Laboratory of Frascati of INFN.

2 The KLOE Superconducting Magnet

The KLOE experiment [6] recorded data from e^+e^- collisions at DAΦNE, the ϕ-factory at the Laboratori Nazionali di Frascati (LNF), since April 1999. The detector is surrounded by a NbTi Superconducting magnet [7, 8] providing an homogeneus 0.6 T field. The magnet cryostat has an inner diameter of 4.86 m and a length of 4.4 m. The coil is kept at a temperature of 4.5 K with liquid helium. The helium flow comes from a cryogenic plant with an extra cooling capacity which has been formerly dedicated to the FINUDA experiment and to the four compensating solenoids operating in the DAFNE collider.

3 The KLASH Haloscope

In order to run at 4 K, the copper resonant-cavity will be hosted in a dedicated cryostat (Fig. 1) composed of a vacuum chamber and a radiation shield at $\sim$ 70 K surrounding the cavity. The preliminary design foresees a cavity diameter of 3.72 m with maximum length of 3 m corresponding to a total volume of about 33 m^3. The total weight of cryostat and cavity is expected to be about 12 tons, driven by mechanical constraints.

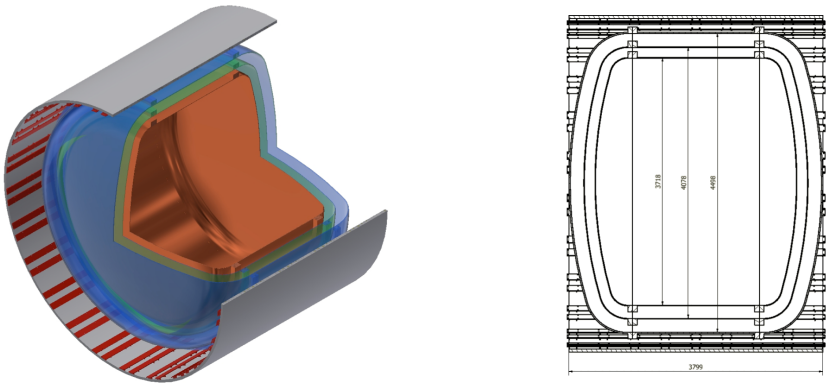

Figure 1: Left: 3D sketch of the cryostat inserted into the SC magnet, together with the 70 K screen and the copper cavity. Right: Preliminary design of cryostat and cavity.

The nominal resonance-frequency of the cavity is 64 MHz with quality factor about 750,000 at 4K assuming copper with RRR=25. Simulations show that a conventional system of two metallic tuning rods with 300 mm radius shift the resonance frequency from 70 to 110 MHz while keeping the quality factor above 500,000. Several strategies are under investigation to tune the frequency up to 250 MHz, including a multiple-cell cavity [9] or its replacement with smaller ones, allowing us to probe the axion-mass region between 0.3 and 1 μeV. From preliminary calculations the quality factor is expected to scale almost linearly with frequency from 550,000 at 70 MHz down to 370,000 at 250 MHz. The cavity mode will be critically coupled to an electric-dipole field-probe and the signal read-out with a conventional or microstrip SQUID amplifier. A ^{3}He refrigerator will cool down the SQUID amplifier to reduce its noise temperature to 300 mK [10].

4 The KLASH Sensitivity

In this section, we assume to perform the frequency scan by employing three different cavities of radii 1.9, 1.2 and 0.9 m with two tuning rods both of radius 300, 190 and 140 mm, respectively. The integration time for each frequency step is expected to be between 10 and 15 minutes. The discovery potential in the coupling-mass plane, calculated with these assumptions, is shown in Figure 2. The sensitivity band reaches the region predicted for QCD axions of the KSVZ and DFSZ models in the mass range between 0.3 and 1 μeV. The three vertical purple-bands

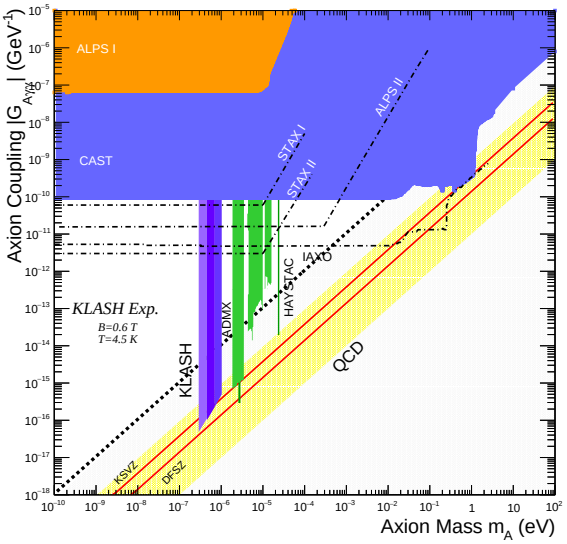

Figure 2: The KLASH discovery potential for axion mass m_a in the range between 0.3 and 1 μeV, in three years of data taking. The three purple bands correspond to data taking with three different cavities of radii 1.9, 1.2 and 0.9 m. The yellow band is the preferred region for the KSVZ and DFSZ models. The gray region below the dashed line refers to the axion models discussed in [11]. Also shown the expected sensitivity of STAX [12], IAXO [13] and ALPSII [14].

correspond to one year of data taking with each of the three resonant cavities.

5 Conclusions

At the moment of writing, INFN funded a design study of one year for the KLASH Conceptual Design Report. One of the main outcomes of this study will be the mechanical design of the cryostat that will allow us to define the cost of construction.

References

[1] D. Alesini *et al.*, "The KLASH Proposal," arXiv:1707.06010.

[2] J. Kim, "Weak-Interaction Singlet and Strong CP Invarianc" Phys. Rev. Lett. **43**, 103 (1979). M.A. Shifman, A.I. Vainshtein, and V.I. Zakharov, "Can confinement ensure natural CP invariance of strong interactions" Nucl. Phys. B **166**, 493 (1980).

[3] M. Dine, W. Fischler, and M. Srednicki, "A simple solution to the strong CP problem with a harmless axion" Phys. Lett. B **104**, 199 (1981); A.P. Zhitnitskii, "On Possible Suppression of the Axion Hadron Interactions" Sov. J. Nucl. Phys. **31**, 260 (1980).

[4] P. Sikivie, "Experimental Tests of the "Invisible" Axion," Phys. Rev. Lett. **51**, 1415 (1983) and "Detection rates for invisible-axion searches," Phys. Rev. D **32**, 2988 (1985).

[5] N. Du *et al.*,"Search for Invisible Axion Dark Matter with the Axion Dark Matter Experiment," Phys. Rev. Lett. **120**, 151301 (2018).

[6] P. Franzini and M. Moulson, "The Physics of DAFNE and KLOE" Annu. Rev. Nucl. Part. S. **56**,207-251 (2006).

[7] J.S.H.Ross et al., "Progress in the design, manufacturing and testing of the KLOE solenoid for the DANE ring at Frascati". 1997 Particle Accelerator Conference, Vancouver (Canada) 12-16 May 1997.

[8] M. Modena, "The DaΦNE Cryogenic System", LNF-97/046(IR) (1997).

[9] J. Jeong *et al.*, "Concept of multiple-cell cavity for axion dark matter search", Phys.Lett. **B**, 777 (2018), arXiv:1710.06969.

[10] M. Muck *et al*, "Superconducting quantum interference device as a near-quantum-limited amplifier at 0.5 GHz," App. Phys. Lett. **78**, 967 (2001).

[11] L. Di Luzio, F. Mescia, and E. Nardi, "Redefining the Axion Window," Phys. Rev. Lett. **118**, 031801 (2017).

[12] L. Capparelli *et al.*,"Axion-like particle searches with sub-THz photons," Phys. Dark Univ. **12**, 37 (2016).

[13] IAXO collaboration, I. Irastorza, "The International Axion Observatory IAXO". Letter of Intent to the CERN SPS committee.

[14] A. Spector, "ALPS II technical overview and status report," arXiv:1611.05863.

Probing axion-photon coupling from the resonant conversion of QCD axion and ALP dark matter

Shu-Yu Ho[1], *Ken'ichi Saikawa*[2], *Fuminobu Takahashi*[3,4]

[1]Department of Physics, Tohoku University, Sendai, Miyagi 980-8578, Japan
[2]Max-Planck-Institut für Physik (Werner-Heisenberg-Institut), Föhringer Ring 6, D-80805 München, Germany
[3]Kavli Institute for the Physics and Mathematics of the Universe (Kavli IPMU), UTIAS, WPI, The University of Tokyo, Kashiwa, Chiba 277-8568, Japan
[4]Center for Theoretical Physics, Massachusetts Institute of Technology, Cambridge, MA 02139, U.S.A.

DOI: http://dx.doi.org/10.3204/DESY-PROC-2018-03/Ho_Shu-Yu

We refine the adiabatic condition of the conversion between the QCD axion and axion-like particle (ALP) at level crossing. We then focus on a scenario where the ALP produced by the adiabatic conversion of the QCD axion explains the observed dark matter abundance. Interestingly, we find that the ALP decay constant can be much smaller than the ordinary case in which the ALP is produced by the realignment mechanism. As a consequence, the ALP-photon coupling is enhanced by a few orders of magnitude, which is advantageous for the future ALP and axion-search experiments using the ALP-photon coupling.

1 Introduction of axions

The axion is a hypothetical particle, which was originally postulated in order to resolve the strong CP problem in quantum chromodynamics (QCD). The Lagrangian of QCD includes a CP-violating term with a dimensionless coefficient $\theta_{\rm QCD}$. This coefficient is usually called the strong CP phase. From the measurements of the neutron electric dipole moment, the magnitude of $\theta_{\rm QCD}$ is severely constrained to be less than 10^{-10}. Such a tiny $\theta_{\rm QCD}$ is unnatural and needs an explanation.

One of the plausible solutions to the strong CP problem is the Peccei-Quinn (PQ) mechanism. In this mechanism, the strong CP phase is promoted to a dynamic variable and one introduces a scalar field a called the QCD axion, which is a pseudo-Nambu-Goldstone boson associated with the spontaneous breakdown of a global axial U(1) PQ symmetry. At energies below the QCD confinement scale, the QCD axion acquires a potential due to non-perturbative effects of QCD and then it rolls down to a CP-conserving minimum, solving the strong CP problem. The potential of the QCD axion can be approximated by a cosine form as $V_{\rm QCD}(a) = m_a^2(T) f_a^2 \left[1 - \cos\left(a/f_a\right)\right]$, where $m_a(T)$ and f_a are the mass and the decay constant of the QCD axion, respectively. The temperature-dependent QCD axion mass based on one of the latest lattice QCD result is given in [1].

The QCD axion starts oscillating around its potential minimum from an initial misalignment

value, $a_0 \equiv f_a\theta_0$, when $m_a(T)$ becomes comparable to the Hubble parameter $H(T)$. Such a coherently oscillating axion field can be treated as cold dark matter (DM) in the universe. This is the so-called realignment mechanism based on the assumption that the PQ symmetry was broken before or during inflation and never restored afterward. The relic abundance of the QCD axion DM, Ω_a, in the regime $|\theta_0| \ll \pi$ is estimated as $\Omega_a h^2 \simeq 0.14\,\theta_0^2\big(f_a/10^{12}/\mathrm{GeV}\big)^{1.17}$, where h is the normalized Hubble constant, and this formula is only valid in the case when the QCD axion begins to oscillate before $m_a(T)$ approaches the zero temperature value. The astrophysical observations put the lower bound on the axion decay constant, $f_a \gtrsim 4\times10^8\,\mathrm{GeV}$, which ensures the stability of the QCD axion DM on a cosmological time scale.

The interactions of the QCD axion with the standard model particles are suppressed by the decay constant. For example, the coupling of the QCD axion to photons is given by $\mathcal{L}_{a\gamma\gamma} = -g_{a\gamma\gamma}a\widetilde{F}_{\mu\nu}F^{\mu\nu}/4$, where $F_{\mu\nu}$ is the electromagnetic field strength tensor and $\widetilde{F}_{\mu\nu}$ is its dual tensor, and the coupling coefficient $g_{a\gamma\gamma} = \alpha/(2\pi f_a)\cdot C_{a\gamma}$ with $C_{a\gamma} = -1.92(4) + \mathcal{E}/\mathcal{N}$, where α is the electromagnetic fine-structure constant, $\mathcal{E}$ the electromagnetic anomaly, and $\mathcal{N}$ the color anomaly of the PQ symmetry.

The concept of the QCD axion can be generalized to the case of many axions or axion-like particles (ALPs), which may appear as low energy descriptions of some fundamental framework such as string theory. The ALPs have similar properties to the QCD axion, but they do not necessarily interact with QCD gluons. Instead, they may acquire a mass from some hidden confining gauge interactions. The ALP φ can also be produced in the early universe via the realignment mechanism and it can serve as cold DM for certain values of the parameters. The relic abundance of ALP DM with a mass m_φ and a decay constant f_φ is evaluated as $\Omega_\varphi h^2 \simeq 0.3\,\theta_{\varphi,0}^2\big(m_\varphi/\mathrm{eV}\big)^{1/2}\big(f_\varphi/10^{12}/\mathrm{GeV}\big)^2$. Finally, ALP can also couple to photons via the Lagrangain as $\mathcal{L}_{\varphi\gamma\gamma} = -g_{\varphi\gamma\gamma}\varphi\widetilde{F}_{\mu\nu}F^{\mu\nu}/4$ with $g_{\varphi\gamma\gamma} = \alpha/(2\pi f_\varphi)\cdot C_{\varphi\gamma}$, where $C_{\varphi\gamma}$ is a model-dependent coefficient. Notice that the ALP-photon coupling only contains the model-dependent contribution, which should be contrasted to the QCD axion-photon coupling which includes the model-independent contribution.

It is reasonable that the QCD axion and ALPs co-exist in nature since the former can solve the strong CP problem in QCD and the latter is motivated by string theory. It is also possible that there is a mass mixing between them due to hidden sectors. We will explore this scenario in the following sections.

2 Mass mixing between the QCD axion and ALP

Suppose that there is an ALP φ which has a mass mixing with the QCD axion a. Such a mass mixing may be induced by the potential of the form $V_{\mathrm{mix}}(a,\varphi) = m_\varphi^2 f_\varphi^2\big[1-\cos\big(a/f_a+\varphi/f_\varphi\big)\big]$. Upon diagonalizing mass mixing matrix, one can obtain the heavy and light mass eigenstates a_H and a_L and their respective masses $m_H(T)$ and $m_L(T)$ and the mixing angle $\xi = \xi(T)$, see Ref. [2] for their explicit forms. One interesting consequence of the mass mixing is that, as the cosmic temperature drops, the values of $m_H(T)$ and $m_L(T)$ approach to each other at high temperatures and apart from each other at low temperatures under certain conditions. We call such behavior the level crossing. More formally, we define the level crossing as a situation in which the squared difference of the mass eigenvalues is minimized at some finite value of T. Accordingly, we find the condition for the level crossing to take place, $f_\varphi/f_a < 1$ and $m_\varphi/m_a < \big(1-f_\varphi^2/f_a^2\big)^{-1/2}$. See Fig. 1.

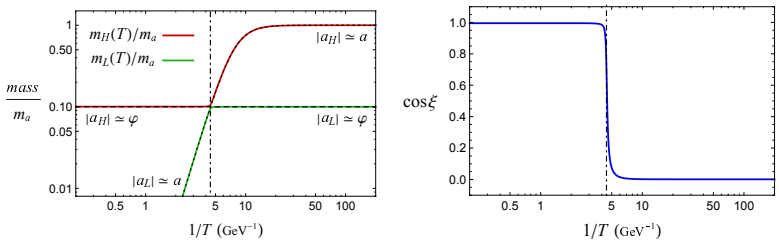

Figure 1: Evolution of the mass eigenvalues and mixing angle as functions of temperature. In the left panel, the red (green) solid line represents the heavier (lighter) mass eigenvalue, the dotted (dashed) black line denotes $m_a(T)\,(m_\varphi)$, and the masses are normalized by the zero temperature QCD axion mass, m_a. The dot-dashed black line in both panels indicates the temperature at the level crossing. For these plots, we have set $m_\varphi/m_a = 0.1$ and $f_\varphi/f_a = 0.1$.

3 Adiabatic conversion and cosmological axion abundances

Under certain conditions, the adiabatic conversion from the QCD axion into ALP could take place at the level crossing. Namely, the composition of light and heavy axions drastically changes across the level crossing. Based on an argument on adiabatic invariants for multiple harmonic oscillators [3], the adiabatic condition between the QCD axion and ALP at the level crossing is written by

$$\left|\frac{d\ln\cos\xi(T)}{dt}\right|^{-1}_{T=T_{\rm l.c.}} \gg \max\left[\frac{2\pi}{m_H(T)}, \frac{2\pi}{m_L(T)}, \frac{2\pi}{m_H(T)-m_L(T)}\right]_{T=T_{\rm l.c.}},$$

where the left-hand (right-hand) side is the external (internal) time scale of the system. One can examine this condition numerically by looking at the time evolution of comoving axion numbers. See Ref. [2] for the definition and numerical results of the comoving axion numbers.

Now let us evaluate the DM abundance. In our model both the light and heavy axions could contribute to DM, and the total DM abundance is given by the sum of their contributions. We have numerically followed the evolution of the QCD axion and ALP for a broad range of f_φ and m_φ and calculated their abundances. Since the comoving number of the light axion produced by the same mechanism as the QCD axion is converted to ALP, and DM behaves like ALP at the present time, then the abundance of DM is suppressed by the mass ratio, which opens up a nontrivial parameter space. In Fig. 2, we show the contours of fixed $\Omega_{\rm DM}h^2$ (f_a) for different values of f_a ($\Omega_{\rm DM}h^2$) in the left (right) panel. Notice that in the bottom right corners of these contours, the ALP decay constant can be a few orders of magnitude smaller than the QCD axion decay constant, which implies an enhancement of the ALP-photon coupling in our model.

4 Implications for the axion search experiments

Many axion search experiments rely on the axion coupling to photons, which is induced by loop diagrams. The Lagrangian describing the interactions between the axions and photons is given as $\mathcal{L}_{\text{axion-}\gamma\text{-}\gamma} = -\left(g_{L\gamma\gamma}\,a_H + g_{H\gamma\gamma}\,a_L\right)\widetilde{F}_{\mu\nu}F^{\mu\nu}/4$, where $g_{H\gamma\gamma}$ and $g_{L\gamma\gamma}$ are the coupling constants with the explicit forms given in [2]. We map the viable regions in the right panel of Fig. 2 into the plane of $(m_L, g_{L\gamma\gamma})$, and the result is shown in Fig. 3, together with various experimental and astrophysical limits on the coupling of the QCD axion and/or ALPs with photons as a function of their mass. As expected, the coupling of the light axion with photons

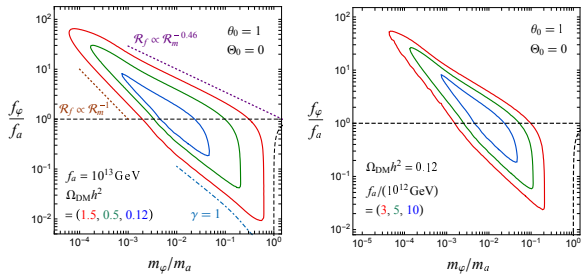

Figure 2: Contours of the DM abundance $\Omega_{\rm DM}h^2 = 0.12, 0.5$, and 1.5 with $f_a = 10^{13}\,\mathrm{GeV}$ (left panel) and $\Omega_{\rm DM}h^2 = 0.12$ for different values of $f_a = (3, 5, 10) \times 10^{12}\,\mathrm{GeV}$ (right panel).

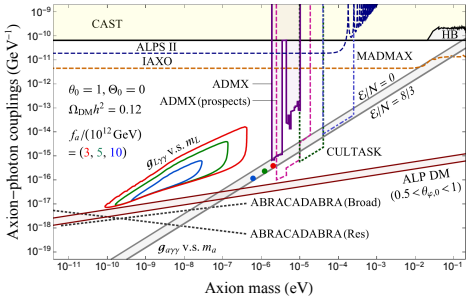

Figure 3: The predicted axion-photon couplings as a function of the light axion mass for $f_a = (3, 5, 10) \times 10^{12}\,\mathrm{GeV}$. Red, green, and blue lines represent the predictions for the mass and coupling of the light axion, and dots represent the corresponding ones of the heavy axion. We also show experimental and astrophysical constraints on the coupling, projected sensitivities of future experiments, the QCD axion coupling with $\mathcal{E}/\mathcal{N} = 0$ and $8/3$, and the region where the ALP explains DM without a mass mixing (brown diagonal band).

in our model is enhanced by a few orders of magnitude compared with the prediction of the single ALP DM shown as the brown band.

5 Summary

We have strictly defined the condition of the level crossing to take place between the QCD axion and ALP and refined the condition of the adiabatic conversion between them by considering another relevant timescale which was missed in Ref. [4]. We have numerically checked the validity of the refined adiabatic condition by looking at the time evolution of comoving axion numbers. We have also shown that the ALP (or more precisely, the lighter mass eigenstate) with a relatively small decay constant gives the dominant contribution to the observed DM abundance, which is advantageous for future axion search experiments.

References

[1] S. Borsanyi *et al.*, Nature **539**, no. 7627, 69 (2016) [arXiv:1606.07494 [hep-lat]].

[2] S. Y. Ho, K. Saikawa and F. Takahashi, JCAP **1810**, no. 10, 042 (2018) [arXiv:1806.09551 [hep-ph]].

[3] M. Devaud, V. Leroy, J-C. Bacri, and T. Hocquet, `https://hal.archives-ouvertes.fr/hal-00197565`, 2007.

[4] N. Kitajima and F. Takahashi, JCAP **1501**, no. 01, 032 (2015) [arXiv:1411.2011 [hep-ph]].

Axions and the Galactic disc and halo white dwarf luminosity functions

Jordi Isern[1,2]

[1]Institut de Ciències de l'Espai (ICE,CSIC), Barcelona, Spain
[2]Institut d'Estudis Espacials de Catalunya (IEEC), Barcelona, Spain

DOI: http://dx.doi.org/10.3204/DESY-PROC-2018-03/Isern_Jordi

The evolution of white dwarfs is a simple gravothermal cooling process of. Since their luminosity function (LF) is sensitive to the characteristic cooling time, it is possible to use its slope to test the existence of additional unexpected sources or sinks of energy. We compute theoretical LF of the Galactic thin and thick disks, and stellar halo and we compare them with the observed ones. The signature of an unexpected extra cooling seems to be present in the LF of these galactic structures and seems compatible with the existence of DFSZ axions with coupling constant $g_{\rm ae} \sim 1.5 - 2.2 \times 10^{-3}$.

1 Introduction

White dwarfs are the last evolutionary stage of stars with a mass $M \leq 10 \pm 2$ M$_\odot$. They are degenerate objects and their evolution is just a gravothermal cooling process. Their structure consists of a degenerate core containing the bulk of mass that acts as an energy reservoir, plus a partially degenerate envelope that controls the energy outflow. White dwarfs with masses $M \lesssim 0.4$ M$_\odot$ have He cores, those with $M \gtrsim 1.1$ M$_\odot$ have ONe cores, and those with a mass in between, the large majority, have cores made of a mixture of ^{12}C and ^{16}O plus some impurities, being ^{22}Ne the most important one. All of them are surrounded by a thin helium layer with a mass $\sim 10^{-2}$ M$_{\rm WD}$, and 80% of them are also surrounded by an even thinner layer of hydrogen containing a mass in the range of 10^{-15} to 10^{-4} M$_\odot$. White dwarfs displaying hydrogen in their spectra are generically referred as DA, and the remaining ones non-DA.

Globally, the evolution of the luminosity of white dwarfs can be written as:

$$L + L_\nu + L_{\rm x} = -\int_0^{M_{\rm WD}} C_{\rm v} \frac{dT}{dt}\, dm - \int_0^{M_{\rm WD}} T\Big(\frac{\partial P}{\partial T}\Big)_{V,X_0} \frac{dV}{dt}\, dm + \quad (l_{\rm s} + e_{\rm s})\dot{M}_{\rm s} + \varepsilon_{\rm x} \qquad (1)$$

where the l.h.s. of the equation represents the sinks of energy due to photons, neutrinos and any exotic particle, while the r.h.s. contains the sources of energy like the heat capacity of the star, the work due to the change of volume, the contribution of the latent heat and gravitational settling upon crystallization, times the rate of solidification, $\dot{M}_{\rm s}$, and any additional exotic source [1]. If it is assumed that the core is nearly isotherm and this equation is complemented with a relationship connecting the temperature of the core with the luminosity of the star, typically $L \propto T_{\rm c}^{\alpha}$, where $\alpha \simeq 2.7$, it is possible to obtain the evolution of the central temperature. Therefore, this means that white dwarfs can be used as a calorimeter to detect the presence of additional sources or sinks of energy.

There are two ways to measure the cooling rate of white dwarfs, one is through the secular drift of the period of pulsation of variables and the other by fitting the shape of the luminosity function.

The luminosity function is defined as the number of white dwarfs of a given luminosity per unit of magnitude interval and unit volume:

$$n(l) = \int_{M_{\rm i}}^{M_{\rm s}} \Phi(M)\,\Psi(\tau)\tau_{\rm cool}(l,M)\;dM \tag{2}$$

where $\tau = T_G - t_{\rm cool}(l,M) - t_{\rm PS}(M)$, M is the mass of the parent star (for convenience all white dwarfs are labeled with the mass of the main sequence progenitor), $l = -\log(L/L_\odot)$, T_G is the age of the population under study, $t_{\rm cool}$ is the cooling time down to luminosity l, $\tau_{\rm cool} = dt/dM_{\rm bol}$ is the characteristic cooling time, $M_{\rm s}$ and $M_{\rm i}$ are the maximum and the minimum mass respectively of a main sequence star able to produce a white dwarf, of luminosity l, i.e. is the mass that satisfies the condition, $T_G = t_{\rm cool}(l,M) + t_{\rm PS}(M)$ and $t_{\rm PS}$ is the lifetime of the progenitor of the white dwarf. The remaining quantities, the initial mass function, $\Phi(M)$, and the star formation rate (SFR), $\Psi(t)$, are not known a priori and depend on the galactic properties of the stellar population under study. Since the total density of white dwarfs is not well known, the computed luminosity function is usually normalized to the bin with the smallest error bar, traditionally the one with $l = 3$, in order to compare theory with observations.

An interesting feature is that the bright part of the white dwarf luminosity function - that with bolometric magnitude $M_{\rm bol} < 13$ - is almost independent of the assumed star formation rate. This can be explained with simple arguments. Since the characteristic cooling time is not strongly dependent on the mass of the white dwarf, Eq. 2 can be written as:

$$n(l) \propto \langle\tau_{\rm cool}\rangle \int \Phi(M)\Psi(\tau)dM \tag{3}$$

Restricting ourselves to bright white dwarfs - namely, those for which $t_{\rm cool}$ is small - the lower limit of the integral is satisfied by low-mass stars and, as a consequence of the strong dependence of the main sequence lifetimes with the mass, it takes a value which is almost independent of the luminosity under consideration. Therefore, if Ψ is a well behaved function and T_G is large enough, the integral is not sensitive to the luminosity, its value is absorbed by the normalization procedure and the shape of the luminosity function only depends on the averaged physical properties of white dwarfs. In any case, it is important to realize that adjusting bin by bin it is possible to find an SFR that almost completely fits the observed luminosity function [2] and is compatible with the SFRs obtained with independent methods [3]. This SFR is obtained as an *ad hoc* fit to the observations using the existing models of white dwarf cooling. Consequently other models with different physical ingredients would provide different results. One way to break this degeneracy and to decide if it is necessary to include new physics is to examine the luminosity functions of populations that have independent star formation stories as the signature introduced by any anomalous process should be present in all of them at similar luminosities [4]. It is important to emphasize here that the luminosity band $6 \lesssim M_{\rm bol} \lesssim 13$ is the one with less theoretical uncertainties and where all the present models of cooling coincide. In this work the BaSTI model [5] has been used, but the results have been tested with other independent cooling sequences [4].

2 The axion case

Axions couple to photons, electrons and nucleons with strengths that depend on the specific implementation of the Peccei-Quinn symmetry. For instance, in the KSVZ model, axions couple with hadrons and photons, while in the DFSZ model they also couple with electrons. In all of them, the strength of the interaction is not fixed by the theory and is related with the mass of the axion. As happens with neutrinos, axions can be copiously produced in the hot and dense interiors of stars and, depending on their coupling with matter and photons, they can modify the expected evolution of stars and reveal in this way their existence.

The first hint that axions could be modifying the cooling of white dwarf stars was provided by the secular drift of the period of pulsation of G117-B15A [7], a DA variable. The argument was that these white dwarfs are placed in the luminosity domain where the cooling by neutrinos, $\dot{\epsilon}_\nu \propto T^7$, is substituted by the cooling by photons, $L_\nu \propto T^{2.5}$, and the cooling by DFSZ axions, $\dot{\epsilon}_\mathrm{a} \propto T^4$, can provide the extra cooling necessary to account for the observed drift of G117-B15A.

The second hint was provided by the white dwarf luminosity function which displays a slight excess of white dwarfs in the region $M_\mathrm{bol} \sim 8-10^\mathrm{mag}$ that can be easily removed if the influence of DFSZ axions with $g_\mathrm{ae} \times 10^{13} \sim 0.6-2.24$ is included [8]. A similar result was obtained using other independent empirical luminosity functions [9, 10, 11].

3 Results and conclusions

As it has been already mentioned, if axions or any other cooling agent are acting on white dwarfs, their imprint must be present in all the galactic structures. In particular, using the Super Cosmos Sky Survey (SCSS), it has been possible to separate the contributions of the thin, thick discs and halo to the luminosity function [12]. In all three cases, the standard model of cooling predicts an excess of white dwarfs in the same region around $M_\mathrm{bol} \simeq 10^\mathrm{mag}$, providing support to the hypothesis that this shortage is not a consequence of the star formation rate but of the existence of an additional energy sink [4]. Recently, Munn [13] has improved and separated the contributions of the disc and halo white dwarfs to the luminosity function obtained from the Sloan Digital Sky Survey (SDSS) [14]. As before, the discrepancies between theory and observations decrease when axions are included [4].

An important ingredient in building the luminosity function of bright white dwarfs is the role played by the adopted scale height. It has been argued [15] that the existing discrepancies in the region $M_\mathrm{bol} \sim 6-12^\mathrm{mag}$ is caused by the use of a fixed scale height. Once more it has been found that, when variable scale heights are used, the inclusion of axions improves the agreement between theory and observations [4].

The shape of he luminosity functions studied here could also be reproduced just adding bursts of star formation of convenient intensity at convenient times in the history of the Galaxy. Strictly speaking we cannot discard a conspiracy of Nature to produce similar features at the same places in the luminosity function of white dwarfs in populations that are not correlated or weakly correlated, but it seems more natural to invoke an intrinsic property of white dwarfs. Certainly, the results presented here do not prove the existence of axions and other possibilities, like the different cooling rates of DA and non-DA white dwarfs, have to be considered, but any alternative solution has to be able to provide an explanation to the observed secular drift of ZZ Ceti stars. In any case, these results provide a compelling argument to explore the possibilities of detecting axions with a mass in the few meV domain.

Finally, it is necessary to emphasize that the existence of axions with the properties quoted here can introduce subtle but detectable changes in the evolution of stars as is the case of red giants [16], horizontal branch stars [17] and globular clusters [16, 18, 19].

Acknowledgments

This work has been supported by MINECO grants ESP2015-66134-R (JI), by the European Union FEDER funds, and by grants 2014SGR1458 (JI) and the CERCA program of the Generalitat de Catalunya.

References

[1] J. Isern, E. García-Berro, M. Hernanz, R. Mochkovitch, "The physics of white dwarfs," J. Phys. Cond. Mat. **10**, 11263 (1998).

[2] N. Rowell, "The star formation history of the solar neighborhood from the white dwarf luminosity function," MNRAS **434**, 1549 (2013).

[3] M. Cignoni *et al.*, "Recovering the star formation rate in the solar neighborhood," A&A **459**, 783 (2006).

[4] J. Isern *et al.*, "Axions and the luminosity function of white dwarfs. The thin and thick disks, and the halo," MNRAS **478** 2569 (2018).

[5] M. Salaris *et al.*, "A large stellar evolution database for population synthesis studies. VI. White dwarf cooling sequences," ApJ **716**, 1241 (2010).

[6] G. G. Raffelt, "Stars as laboratories for fundamental physics : the astrophysics of neutrinos, axions, and other weakly interacting particles," Chicago: University of Chicago Press (1996).

[7] J. Isern *et al.*, "Axion cooling of white dwarfs," ApJ **392**, L23 (1992).

[8] J. Isern it et al., "Axions and the cooling of white dwarfs," ApJ **682**, L109 (2008).

[9] J. Isern it et al., "Axions cooling of white dwarfs," in Proceedings of the 8th Patras Workshop on Axions, WIMPs and WISPs (2013) [arXiv: 1304.7652].

[10] M.M. Miller Bertolami *et al.*, "Revisiting the axion bounds from the galactic white dwarf luminosity function," JCAP **10** 069 (2014).

[11] J. Isern, "Gaia and the use of white dwarfs as advanced Physics laboratories," in Proceedings of The Golden Age of Cataclysmic Variables and Related Objects - III, Palermo, Italy (2015). [Online at http://pos.sissa.it/cgi-bin/reader/conf.cgi?confid=255, id.5].

[12] N. Rowell, N.C. Hambly, "White dwarfs in the SuperCOSMOS Sky Survey: the thin disc, thick disc and spheroid luminosity functions," MNRAS **417**, 93 (2011).

[13] J.A. Munn *et al.*, "A Deep Proper Motion Catalog Within the Sloan Digital Sky Survey Footprint. II. The White Dwarf Luminosity Function ," AJ **153**, 10 (2017).

[14] H.C. Harris *et al.*, "The White Dwarf Luminosity Function from Sloan Digital Sky Survey Imaging Data," AJ **131** 571 (2006).

[15] M. Kilic *et al.*, "The Ages of the Thin Disk, Thick Disk, and the Halo from Nearby White Dwarfs," MNRAS **837**, 162 (2017).

[16] N. Viaux *et al.*, "Neutrino and Axion Bounds from the Globular Cluster M5 (NGC 5904)," PRL **111**, 231301 (2013).

[17] A. Ayala *et al.*, "Revisiting the Bound on Axion-Photon Coupling from Globular Clusters," PRL **113**, 191302 (20149.

[18] B.M. Hansen *et al.*, "Constraining Neutrino Cooling Using the Hot White Dwarf Luminosity Function in the Globular Cluster 47 Tucanae," ApJ bf 809, 141 (2015).

[19] R. Goldsbury *et al.*, "Constraining White Dwarf Structure and Neutrino Physics in 47 Tucanae," ApJ **82.**, 27 (2016).

Search for Dark Matter in the form of Axion-like Particles and Hidden Photons in the XMASS Detector

Kazufumi Sato[1] *for the XMASS collaboration*

[1]University of Tokyo, Gifu, Japan

DOI: http://dx.doi.org/10.3204/DESY-PROC-2018-03/Kazufumi_Sato

XMASS searches for dark matter using a liquid xenon scintillator. With its low background environment, the XMASS detector has sensitivity not only for standard WIMPs but also for dark matter interacting with electrons. We conducted searches for axion-like particles and hidden photons as candidates for cold dark matter. These bosons are expected to induce recoiled electrons through an interaction analogous to photoelectric effect. We set most stringent upper limits on the coupling constant g_{Ae} of axion-like particles and the kinetic mixing α'/α of hidden photons over the mass range from 40 to 120 keV/c^2.

1 Introduction

XMASS is a multi-purpose experiment using a liquid xenon scintillator. Its main physics motivation is a direct detection of Dark Matter (DM). XMASS searches for an interaction of DM with xenon target resulting in scintillation emissions induced by recoiled particles. XMASS has a good sensitivity not only for a standard WIMPs producing nuclear recoils, but also for other types of DM producing recoil electrons. On condition without a discrimination between nuclear recoils and electron recoils, we achieve an event rate of $O(10^{-4})$ count/day/kg/keV in the energy range from $\sim$ 20 to 100 keV, which is the lowest rate among xenon direct detection experiments in the same generation [1, 2, 3].

Hidden Photons (HPs) and Axion-like Particles (ALPs) are candidates of cold DM [4]. Both bosons can interact with electrons; ALPs can have a coupling constant g_{Ae} with electrons and HPs can kinetically mixes with normal photons with strength α'/α. As the results, both bosons are absorbed by materials through an interaction analogous to a photoelectric effect [5], transferring their total energy to recoiled electrons. Assuming the bosons are non-relativistic, the energy they deposit in the material is equivalent to their rest mass.

A wide mass region up to O(100keV) is allowed for HPs, as shown in Fig. 5 of Ref. [4]. In high mass region, indirect searches give stringent limits of 10^{-26} on the α'/α in the mass ranges from 1 keV/c^2 to 50 keV/c^2 and above 120 keV/c^2. Such indirect limits are, however, relatively weak ($\alpha'/\alpha < O(10^{-24})$ around 90 keV/c^2, where XMASS has a good sensitivity and a potential to set more stringent limits. In this paper, we present results of the searches for ALPs and HPs using 800 live-days of XMASS data taken in 2013–2016.

2 XMASS detector

The XMASS detector [6] is located 2700 m.w.e underground at Kamioka Observatory in Japan. The XMASS detector consists of an inner detector contained in a vacuum-insulated copper vessel, and an outer detector surrounding the vessel. The inner detector is a liquid xenon scintillator with 832 kg of sensitive volume. A scintillation emission resulting from the interaction between DM and the xenon target is detected by 642 photomultiplier tubes (PMTs) which cover ∼62% of the inner surface of the sensitive volume. The outer detector is a cylindrical-shaped water-Cherenkov counter used as an active veto for cosmic-ray muons and as a passive shield for neutrons and γ-rays from outside environment.

3 Analysis

We searched for signal peaks induced by ALPs or HPs in the observed energy spectrum. The details of analysis are presented in [7] and references therein.

We analyzed events where at least 4 PMTs have hits over 0.2 PE threshold in the inner detector and no significant activities in the outer detector. XMASS standard cuts [7] were applied to reject events originating from PMT after-pulses and electronic noise.

In this stage, dominant backgrounds (BGs) come from β-rays and γ-rays from radioactive isotopes (RIs) contained in the detector materials, such as the PMTs and its support structure. The xenon volume itself serves as an effective shield for such radiations. An event vertex is reconstructed based on a maximum-likelihood evaluation of the observed PE distribution in the PMTs [6]. By requiring the vertex to be reconstructed inside a fiducial volume which is an inner region less than 30 cm radius, these BGs were effectively suppressed by three orders of magnitude.

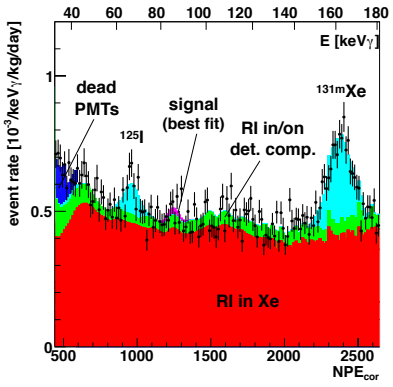

Figure 1: Observed energy spectrum after the fiducial cut. The black dots represent the data. The stacked histograms show the BG MCs (green, red, blue, and light blue) and the signal MC (magenta) at the best fit for a boson mass of 85 keV/c^2.

The energy spectrum after the fiducial volume cut is shown in Fig. 1, where the energy deposit of the event is reconstructed from the total number of PEs (NPE$_{cor}$) with corrections for the position dependence of the PE detection efficiency and for time-dependent change of xenon optical properties [7]. Avoiding a low energy region where we found the contribution from mis-reconstructed events [7] due to dead PMTs, we searched for the signals from ALPs and HPs in the region from 590 to 1760 NPE$_{cor}$ corresponding to 40–120 keV, where the event rate is $\sim 5 \times 10^{-4}$ counts/day/kg/keV. The dominant BGs came from RIs dissolved in liquid xenon, such as ^{85}Kr, ^{214}Pb which is a ^{222}Rn daughter, ^{39}Ar, and ^{14}C. The quantitative evaluation for abundances of these RIs as well as RIs with smaller contribution, such as RIs in the detector materials and xenon isotopes activated by external neutrons, is described in [7].

3.1 Expected signal

Assuming the DM velocity is non-relativistic, the event rate of the absorption of ALPs (HPs) in the xenon target, $R_{ALP(HP)}$, is expressed in the term of the cross-section of photoelectric effect σ_{pe} replacing the photon energy ω by the mass $m_{ALP(HP)}$, as [5]:

$$R_{ALP}[1/\mathrm{kg/day}] = \frac{1.2\times10^{19}}{A} g_{Ae}^2 \sigma_{pe}(\omega = m_{ALP})[\mathrm{barn}] \cdot m_{ALP}[\mathrm{keV}]$$

for ALPs and

$$R_{HP}[1/\mathrm{kg/day}] = \frac{4\times10^{23}}{A}\frac{\alpha'}{\alpha}\frac{\sigma_{pe}(\omega = m_{HP})[\mathrm{barn}]}{m_{HP}[\mathrm{keV}]}$$

for HPs, where $A = 131.3$ is xenon's atomic mass and we assume that a DM density is 0.3 GeV/cm^3. Because the absorption is an analogue of photoelectric effect, the detector response to ALPs (HPs) with mass $m_{ALP(HP)}$ was evaluated using a Monte Calro (MC) simulation for standard photons whose energies = $m_{ALP(HP)}$. The expected energy spectrum is an almost Gaussian which peaks around $m_{ALP(HP)}$.

3.2 Peak search

We searched for a signal peak by fitting the histogram of the observed energy spectrum (Fig. 1) with MC expectations for BG RIs and signals. For ALPs, the fitting chi-square was defined as:

$$\chi^2_{fit}\left(m_{ALP}, g_{Ae}\right) \equiv \sum_i^{N_{bin}} \frac{\left(R^i_{obs} - R^i_{BGtot} - R^i_{ALP}(m_{ALP}, g_{Ae})\right)^2}{\left(\delta R^i_{obs}\right)^2 + \left(\delta R^i_{BGtot}\right)^2 + \left(\delta R^i_{ALP}\right)^2} + \chi^2_{sys}, \tag{1}$$

where R^i_{obs}, R^i_{BGtot}, and R^i_{ALP} are event rates in the i-th bin for the data, BG MC, and signal MC, respectively, and $\delta R_{obs}, \delta R_{BGtot}$, and δR_{ALP} are their respective statistical errors. The chi-square for HPs is obtained by replacing $R^i_{ALP}(m_{ALP}, g_{Ae})$ to $R^i_{HP}(m_{HP}, \alpha'/\alpha)$. The R_{BGtot} is the sum of BG MCs for each RI, *i.e.*:

$$R_{BGtot} = \sum_{j:\mathrm{RI\ types}} p_j R_{j\text{-th BG}},$$

where the $R_{j\text{-th BG}}$ is the expected event rate from the j-th RI and p_j is its scale parameter whose initial value is unity. The chi-square was minimized separately for every 2.5 keV/c^2 step in the mass between 40–120 keV/c^2 and for each fine step of α'/α in the $\alpha'/\alpha > 0$ region, by fitting the p_js. We thus obtained the chi-square profile as a function of α'/α for each mass.

The systematic uncertainties are taken into consideration through a penalty term χ^2_{sys} in Eq. (1). It handles the uncertainty of the abundance of each RI and the uncertainties of MC parameters which are the non-linearity of xenon scintillaiton yield, the energy resolution and position resolution of the detector, and BG increases due to dead PMTs. The detail descriptions of χ^2_{sys} and the systematic uncertainties are found in [7].

4 Result

We did not find any finite signal peaks, and thus set 90% CL upper limits on g_{Ae} and α'/α in a 40–120 keV/c^2 mass region, as shown in Fig. 2. Our limits, $g_{Ae} < 1.6\times10^{-13}$–$4\times10^{-13}$ for

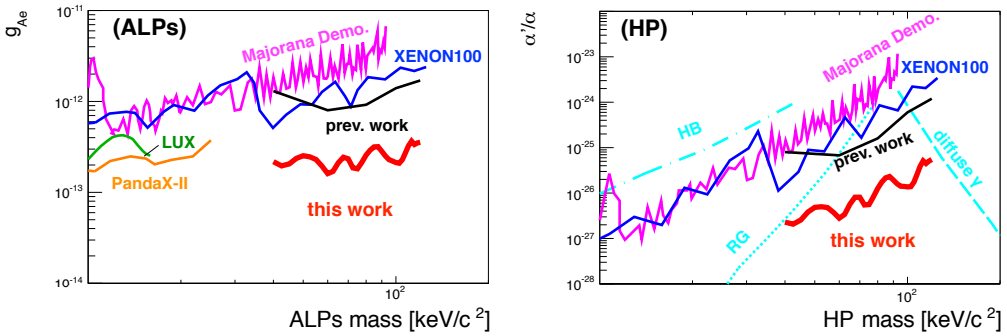

Figure 2: Constraints on g_{Ae} of ALPs (left) and α'/α of HPs (right). The red line shows the 90% CL constraint presented in this report. The limits from other direct searches [1, 2, 3, 8] and indirect searches [9] are also shown.

ALPs and $\alpha'/\alpha < 2 \times 10^{-27}$–$6 \times 10^{-26}$ for HPs, are the most stringent limits over this mass range. Limits from other direct and indirect searches are also shown in the figure. Our results compensate the HP mass region where the indirect limits are relatively weak, and cover the higher ALP mass region than limits from LUX and PandaX-II.

5 Acknowledgments

We gratefully acknowledge the cooperation of the Kamioka Mining and Smelting Company. This work was supported by the Japanese Ministry of Education, Culture, Sports, Science and Technology, Grant-in-Aid for Scientific Research, JSPS KAKENHI Grant No. 19GS0204 and 26104004, the joint research program of the Institute for Cosmic Ray Research (ICRR), the University of Tokyo, and partially by the National Research Foundation of Korea Grant (NRF-2011-220-C00006) and Institute for Basic Science (IBS-R017-G1-2018-a00).

References

[1] D. S. Akerib *et al.* (LUX Collaboration), Phys. Rev. Lett. **118**, 261301 (2017) [arXiv:1704.02297 [astro-ph.CO]].

[2] C. Fu *et al.* (PandaX-II Collaboration), Phys. Rev. Lett. **119**, 181806 (2017) [arXiv:1707.07921 [hep-ex]].

[3] E. Aprile *et al.* (XENON Collaboration), Phys. Rev. D **96**, 122002 (2017) [arXiv:1709.02222 [astro-ph.CO]].

[4] P. Arias, D. Cadamuro, M. Goodsell, J. Jaeckel, J. Redondo, and A. Ringwald, JCAP **2012**, 013 (2012) [arXiv:1201.5902 [hep-ph]].

[5] M. Pospelov, A. Ritz, and M. Voloshin, Phys. Rev. D **78**, 115012 (2008) [arXiv:0807.3279 [hep-ph]].

[6] K. Abe *et al.* (XMASS Collaboration), Nucl. Inst. Meth. A **716**, 78 (2013) [arXiv:1301.2815 [physics.ins-det]].

[7] K. Abe *et al.* (XMASS Collaboration), [arXiv:1807.08516 [astro-ph.CO]], and XMASS papers cited therein.

[8] N. Abgrall *et al.* (Majorana Collaboration), Phys. Rev. Lett. **118**, 161801 (2017) [arXiv:1612.00886 [nucl-ex]].

[9] H. An, M. Pospelov, J. Pradler, and A. Ritz, Phys. Lett. B **747**, 331 (2015) [arXiv:1412.8378 [hep-ph]].

Effective Approximation of Electromagnetism for Axion Haloscope Searches

Younggeun Kim[1,2], *Dongok Kim*[1,2], *Junu Jung*[1,2], *Yun Chang Shin*[1]*, *Yannis K. Semertzidis*[1,2]

[1]Center for Axion and Precision Physics Research, IBS, Daejeon, South Korea, 34051
[2]Department of Physics, KAIST, Daejeon, South Korea, 34141

DOI: http://dx.doi.org/10.3204/DESY-PROC-2018-03/Kim_Younggeun

An effective approximation is applied to Maxwell's equations with an anomalous axion interaction. A new set of Maxwell's equations acquired from this approximation describes only reacted fields generated by the anomalous interaction. Unlike other approaches, this set of Maxwell's equations inherently satisfies the boundary condition for haloscope searches. The electromagnetic field solutions are evaluated for both cylindrical and as toroidal cavity geometries. A small but non-zero difference between electrically and magnetically stored energies appears in both cases. The difference may come from an anomalous non-dissipating current induced by oscillating axions. A possible haloscope search with an external electric field is also studied from the duality that naturally arises in this approach.

1 Introduction

A very weak coupling of axions with particles from the Standard Model, they may be weakly interacting with the electromagnetic fields as well [1, 2]. The interaction of an axion with an electromagnetic field is governed by allowing an anomalous coupling of the axion to the electromagnetic field as: $a\mathbf{E}\cdot\mathbf{B} \propto -aF_{\mu\nu}\tilde{F}^{\mu\nu}$. This coupling results in the conversion of axions into photons via the inverse Primakoff effect [2]. Most of the successful experiments searching for axion are based on this anomalous interaction in addition to an assumption of axions as halo dark matter, which are accordingly called axion haloscope searches [3, 4]. Fundamentally, to include the anomalous coupling of axion with electromagnetic field requires modification of classical Maxwell's equations [5, 6, 7].

However, due to the axion anomaly, this modification of Maxwell's equations causes other issues : it doesn't naturally satisfy certain boundary condition, particularly one necessary for axion haloscope searches [8, 9]. This is mainly because the electromagnetic field generated from the anomalous interaction is not clearly separated from applied external fields, which is necessary to create the haloscope condition, in Maxwell's equations.

We introduce an effective approximation of Maxwell's equations to decouple the reacted electromagnetic field generated by the anomalous interaction from the external fields. The separated Maxwell's equations provide the motion of the reacted electromagnetic fields only. We

*corresponding author

applied them to axion haloscope cases, and showed they both naturally satisfy boundary conditions for haloscope searches. A very small but non-zero value arises in the difference between the electric and magnetic stored energies in both cases. The difference can be interpreted as a polarization density induced by the anomalous interaction of the axion.

2 Separation of Maxwell's equations for haloscope seraches

The Maxwell's equations can be derived from the full Lagrangian with the Bianchi Identity as follows:

$$\nabla\cdot(\mathbf{E}-cg_{\mathrm{A}}\theta\mathbf{B})=\frac{\rho_e}{\varepsilon},\nabla\cdot\mathbf{B}=0,\nabla\times\mathbf{E}=-\frac{\partial\mathbf{B}}{\partial t},\nabla\times(c\mathbf{B}+g_{\mathrm{A}}\theta\mathbf{E})=\frac{1}{c}\frac{\partial}{\partial t}(\mathbf{E}-cg_{\mathrm{A}}\theta\mathbf{B})+c\mu\mathbf{J}_e, \tag{1}$$

with dimensionless axion coupling constant $g_A=\frac{\alpha_{EM}}{2\pi f_a}c_{a\gamma\gamma}=\frac{g_{\mathrm{A}}}{f_a}$ [10], where $\alpha_{EM}\approx 1/137$ is the fine structure constant and f_a is the axion decay constant in unit of GeV. $c_{a\gamma\gamma}$ is the dimensionless coupling which is model dependent as $c_{a\gamma\gamma}=-1.92$ (KSVZ), or $c_{a\gamma\gamma}=0.75$ (DFSZ) [11, 12, 13, 14]. Then the axion field can be represent as dimensionless field $\frac{a}{f_a}=\theta(t)$ [15]. Many of the ongoing experimental searches for axions from Primakoff's effect are all based on the Maxwell's equations in Eq. 1 [2, 3]. However, because of the axion anomaly, this set of Maxwell's equations doesn't naturally satisfy certain boundary conditions. The general haloscope conditions that have been assumed in other approaches [8, 9] are, zero external currnet $\mathbf{J}_e=0$, zero external charge density $\rho_e=0$, zero external electric field $\mathbf{E}_{\mathrm{ext}}=0$, non zero curlless time independent external magnetic field $\mathbf{B}_{\mathrm{ext}}$. Under theese haloscope conditions, the fourth equation in Eq. 1 becomes $\nabla\times\mathbf{B}=-\frac{g_{\mathrm{A}}}{c}\mathbf{B}_{\mathrm{ext}}\frac{\partial\theta}{\partial t}$. While the boundary condition constrains $\nabla\times\mathbf{B}=0$ on the left side of Ampere's law, the right side doesn't intuitively become zero because of the anomalous interaction term. One can't naively exclude the anomaly term either. This problem was avoided by forcing the non-zero anomalous term using new fields, $\mathbf{E}_a$ and $\mathbf{B}_a$ [8, 9] as, $\nabla\times\mathbf{B}_a=-\frac{g_{\mathrm{A}}}{c}\mathbf{B}_{\mathrm{ext}}\frac{\partial\theta}{\partial t}=\frac{1}{c^2}\frac{\partial\mathbf{E}_a}{\partial t}$. These solutions for an electromagnetic field obtained from this approach don't explicitly satisfy Maxwell-Faraday's law for oscillating axion field. This is because the electromagnetic field generated from the anomalous interaction was not clearly decoupled from the electromagnetic field applied for the axion interaction in Maxwell's equations even though they are quite different from each other in terms of magnitudes and directions.

This issue can be resolved by applying an effective approximation onto the Maxwell's equations in Eq. 1. By assuming that the axion anomaly slightly perturbs the electromagnetic field, one can expand the electromagnetic field as;

$$\mathbf{E}=\textstyle\sum_m(g_{\mathrm{A}})^m\mathbf{E}_m=\mathbf{E}_0+g_{\mathrm{A}}\mathbf{E}_1+g_{\mathrm{A}}^2\mathbf{E}_2+\cdot\cdot, \tag{2a}$$

$$\mathbf{B}=\textstyle\sum_m(g_{\mathrm{A}})^m\mathbf{B}_m=\mathbf{B}_0+g_{\mathrm{A}}\mathbf{B}_1+g_{\mathrm{A}}^2\mathbf{B}_2+\cdots. \tag{2b}$$

Since g_{A} is an order of 10^{-3} in both the KSVZ and DFSZ cases, the higher order terms can be ignored, and only the leading and first order terms are considered,

$$\mathbf{E}\simeq\mathbf{E}_0+g_{\mathrm{A}}\mathbf{E}_1,\ \mathbf{B}\simeq\mathbf{B}_0+g_{\mathrm{A}}\mathbf{B}_1. \tag{3}$$

Now one can assume a certain space filled with the external electromagnetic field, $\mathbf{E}_0$ and $\mathbf{B}_0$. If there is no axion, there is no axion-like interaction. Therefore, the total electromagnetic field in the space will still remain $\mathbf{E}=\mathbf{E}_0$ and $\mathbf{B}=\mathbf{B}_0$.

However, if there are interactions between the external electromagnetic field and axions through the axion-like term, a reacted electromagnetic field, $\mathbf{E}_{\rm rea}$, $\mathbf{B}_{\rm rea}$, will be generated. Therefore, it can be inferred that the total electric and magnetic fields $\mathbf{E}$ and $\mathbf{B}$ in the space are slightly different in terms of magnitudes and directions from the external applied fields $\mathbf{E}_0$ and $\mathbf{B}_0$. In this case, the total fields can be expressed as a superposition of the original fields $\mathbf{E}_0$, $\mathbf{B}_0$ and the reacted fields from the axion-interaction term, $\mathbf{E}_{\rm rea}$, $\mathbf{B}_{\rm rea}$ as:

$$\mathbf{E} = \mathbf{E}_0 + \mathbf{E}_{\rm rea},\ \mathbf{B} = \mathbf{B}_0 + \mathbf{B}_{\rm rea}. \tag{4}$$

By recalling order expansion of electromagnetic field, one can set the relationships of the reacted fields as

$$\mathbf{E}_{\rm rea} = g_{\rm A}\mathbf{E}_1,\ \mathbf{B}_{\rm rea} = g_{\rm A}\mathbf{B}_1. \tag{5}$$

Now, we can apply the specific boundary condition for axion haloscope case: a curlless time independent external magnetic field ($\nabla \times \mathbf{B}_0 = 0,\ \dot{\mathbf{B}}_0 = 0$), zero external electric field ($\mathbf{E}_0 = 0$) with zero current, ($\mathbf{J_e} = 0$), and zero charge density, ($\rho_e = 0$). The set of Maxwell's equations with order of g_A^0 remains describing the external electromagnetic field, $\mathbf{E}_0$ and $\mathbf{B}_0$.

Furthermore, a new set of Maxwell's equations which describes only reacted fields, $\mathbf{E}_{\rm rea}$, $\mathbf{B}_{\rm rea}$ to the applied external magnetic field $\mathbf{B}_0$ is attained as:

$$\nabla \cdot \mathbf{E}_{\rm rea} = 0,\ \nabla \cdot \mathbf{B}_{\rm rea} = 0,\ \nabla \times \mathbf{E}_{\rm rea} = -\frac{\partial \mathbf{B}_{\rm rea}}{\partial t},\ \nabla \times \mathbf{B}_{\rm rea} = \frac{1}{c^2}\frac{\partial}{\partial t}(\mathbf{E}_{\rm rea} - cg_{\rm A}\theta\mathbf{B}_0). \tag{6}$$

Eq. 6 is different from Maxwell's equations in Eq. 1. First of all, Eq. 6 is obtained from a perturbation of the total electromagnetic field. Second, while it is not possible to isolate the reacted electromagnetic field from the applied electromagnetic field in Eq. 1, they are clearly separated.

3 Electromagnetic field for haloscope searches

We can solve the modified Maxwell's equation Eq. 6 with certain boundary condition for some geometry, e.g. cylinder and toroid. This set of solutions is different not only from the ordinary resonant solutions but also from the solutions in Ref. [8]. The special solution for the reacted electric field, $\mathbf{E}_{\rm rea}^{\rm special} = cg_{\rm A}\theta_0 \mathrm{B}_0 e^{-i\omega_a t}$, doesn't propagate or resonate by itself. It just oscillates with the axion oscillating frequency: ω_a. The electromagnetic field starts to propagate or resonate only when the ordinary solutions are acquired. This implies that a conductive surface is required to define the reacted electromagnetic field since the amplitude of reacted fields is defined only by the boundary condition.

Detail description about the field solution and the stored energy difference between electric field and magnetic field is in the literature Ref. [16].

4 Conclusion

We have introduced an effective approximation of Maxwell's equations including the anomalous coupling of an axion with an electromagnetic field to resolve some issues about boundary conditions in the axion haloscope searches. It shows that the reacted electromagnetic field are clearly separated from the applied fields. We also evaluated the resonant electromagnetic field for two different cavity conditions, a cylindrical cavity and a toroidal cavity, from the decoupled

Maxwell's equations. A difference arises between the electric and magnetic energies stored in the cavity mode. The difference can be interpreted as a polarization density induced by the anomalous interaction of the axion.

5 Acknowledgement

This work was supported by IBS-R017-D1-2018-a00.

References

[1] M. Srednicki, "Axion Couplings to Matter. 1. CP Conserving Parts," Nucl. Phys. B **260** (1985) 689. doi:10.1016/0550-3213(85)90054-9

[2] H. Primakoff, Phys. Rev. **81** (1951) 899. doi:10.1103/PhysRev.81.899

[3] P. Sikivie, "Experimental Tests of the Invisible Axion," Phys. Rev. Lett. **51** (1983) 1415 Erratum: [Phys. Rev. Lett. **52** (1984) 695]. doi:10.1103/PhysRevLett.51.1415, 10.1103/PhysRevLett.52.695.2

[4] K. Van Bibber, N. R. Dagdeviren, S. E. Koonin, A. Kerman and H. N. Nelson, "Proposed experiment to produce and detect light pseudoscalars," Phys. Rev. Lett. **59** (1987) 759. doi:10.1103/PhysRevLett.59.759

[5] F. Wilczek, "Two Applications of Axion Electrodynamics," Phys. Rev. Lett. **58** (1987) 1799. doi:10.1103/PhysRevLett.58.1799

[6] L. Visinelli, "Axion-Electromagnetic Waves," Mod. Phys. Lett. A **28** (2013) no.35, 1350162 doi:10.1142/S0217732313501629 [arXiv:1401.0709 [physics.class-ph]].

[7] S. C. Tiwari, "Axion electrodynamics in the duality perspective," Mod. Phys. Lett. A **30** (2015) no.40, 1550204. doi:10.1142/S0217732315502041

[8] B. T. McAllister, S. R. Parker and M. E. Tobar, "Axion Dark Matter Coupling to Resonant Photons via Magnetic Field," Phys. Rev. Lett. **116** (2016) no.16, 161804 Erratum: [Phys. Rev. Lett. **117** (2016) no.15, 159901] doi:10.1103/PhysRevLett.117.159901, 10.1103/PhysRevLett.116.161804 [arXiv:1607.01928 [hep-ph], arXiv:1512.05547 [hep-ph]].

[9] B. R. Ko *et al.*, "Electric and magnetic energy at axion haloscopes," Phys. Rev. D **94** (2016) no.11, 111702 doi:10.1103/PhysRevD.94.111702 [arXiv:1608.00843 [hep-ph]].

[10] D. J. E. Marsh, "Axion Cosmology," Phys. Rept. **643** (2016) 1 doi:10.1016/j.physrep.2016.06.005 [arXiv:1510.07633 [astro-ph.CO]].

[11] J. E. Kim, "Weak Interaction Singlet and Strong CP Invariance," Phys. Rev. Lett. **43** (1979) 103. doi:10.1103/PhysRevLett.43.103

[12] M. A. Shifman, A. I. Vainshtein and V. I. Zakharov, "Can Confinement Ensure Natural CP Invariance of Strong Interactions?," Nucl. Phys. B **166** (1980) 493. doi:10.1016/0550-3213(80)90209-6

[13] M. Dine, W. Fischler and M. Srednicki, "A Simple Solution to the Strong CP Problem with a Harmless Axion," Phys. Lett. **104B** (1981) 199. doi:10.1016/0370-2693(81)90590-6

[14] A. R. Zhitnitsky, "On Possible Suppression of the Axion Hadron Interactions. (In Russian)," Sov. J. Nucl. Phys. **31** (1980) 260 [Yad. Fiz. **31** (1980) 497].

[15] J. E. Kim, "Constraints on very light axions from cavity experiments," Phys. Rev. D **58** (1998) 055006 doi:10.1103/PhysRevD.58.055006 [hep-ph/9802220].

[16] Y. Kim, D. Kim, J. Jung, J. Kim, Y. C. Shin, and Y. K. Semertzidis. Effective Approximation of Electromagnetism for Axion Haloscope Searches. 2018.

Search for solar chameleons with a GridPix detector at the CAST experiment

Christoph Krieger (for the CAST collaboration)
University of Bonn, Bonn, Germany

DOI: http://dx.doi.org/10.3204/DESY-PROC-2018-03/Krieger_Christoph

Axion helioscopes like the CERN Axion Solar Telescope (CAST) can be utilized to search for solar chameleons in a similar way as for solar axions. Here, we report on the results of a solar chameleon search conducted at CAST in 2014 and 2015 using a GridPix detector mounted behind an X-ray telescope and looking for soft X-rays in the regime from 200 eV up to 10 keV originating from converted solar chameleons. As no significant excess over the expected background was observed, an improved upper bound on the chameleon photon coupling $\beta_\gamma < 5.7 \times 10^{10}$ for $1 < \beta_\mathrm{m} < 10^6$ at 95 % CL could be derived, surpassing CAST's previous result by about a factor two and reaching sensitivity below the solar luminosity bound.

1 Dark energy and chameleons

One possible way to explain dark energy is by modifying General Relativity through the introduction of a new scalar field coupling to matter along with a screening mechanism to avoid unnatural effects such as the appearance of a fifth force with long range. For the chameleon, non-linear self-interactions and coupling to matter β_m cause chameleons to acquire a kind of "effective mass" which depends on the local mass density. A recent summary of experimental constraints together with a summary of the underlying theory can be found in [1].

An effective chameleon-photon coupling can be easily introduced allowing for chameleon production through the Primakoff effect in electromagnetic fields and leading to the prediction of solar chameleons. In the Sun, the production in strong magnetic fields in parts of the solar interior can be considered. The tachocline region, located at approximately $0.7\,\mathrm{R}_\odot$, is believed to be a source of such magnetic fields caused by differential rotation. The production of solar chameleons and their earth-based detection with an (axion) helioscope experiment has been intensively studied and proposed in [2, 3].

The flux of solar chameleons originating from the tachocline peaks typically at about 600 eV. Through the inverse Primakoff effect solar chameleons can be (re)converted into soft X-ray photons inside a strong magnetic field. Thus, given X-ray detectors sensitive in the sub-keV energy range, an axion helioscope like the CERN Axion Solar Telescope (CAST) can be refitted into a chameleon helioscope.

2 The CERN Axion Solar Telescope

CAST is an axion helioscope which uses a decommissioned LHC prototype dipole magnet to provide a 9 T magnetic field over a length of almost 10 m [4]. The magnet is mounted on a moving structure allowing it to follow the Sun during sunrise and sunset. The ends of the magnet's bores are equipped with highly sensitive low-background X-ray detectors and (partially) X-ray telescopes. CAST currently provides the best limit on the axion-photon coupling over a wide axion mass range [5]. Following CAST's first solar chameleon search [6] using a silicon drift detector without an X-ray telescope in 2013, in 2014 the GridPix detector [7] was mounted to the MPE X-ray telescope [8].

3 The GridPix detector

The GridPix detector is a gaseous X-ray detector using the GridPix technology which combines a pixelized readout chip with a high granular Micromegas stage matched and precisely aligned to the underlying pixels. It is produced directly on top of the chip by photolithographic postprocessing techniques. As pixelized readout chip, here the Timepix ASIC [9] is used, which features 256×256 square pixels with a pitch of 55 µm. Through the gas amplification stage above each individual pixel, the GridPix detector allows for the detection of single primary electrons. This enables the detection of soft X-ray photons with energies down to a few hundred eV. Through the high spatial resolution of the Timepix ASIC, an event-shape based background suppression can be applied [10].

A detailed description of the GridPix detector for CAST can be found in [7]. Prior to installation at CAST, the GridPix detector was fully characterized at the variable X-ray generator of the CAST detector lab with X-ray energies ranging from 277 eV up to 8 keV [11]. The detector is connected to the X-ray telescope via a custom interface vacuum system and surrounded by a lead shielding to reduce background originating from environmental radiation as well as cosmic muons.

4 Operation at CAST

From October 2014 until its dismantling in December 2015, the GridPix detector took data at CAST and participated in the solar (sunrise) trackings resulting in a total of 4785 h of background data and 254 h of solar tracking [7, 12]. During the whole period the detector worked stable and reliably without any detector related interruption to the data taking at all. The GridPix detector was calibrated daily with an ^{55}Fe source underlining its stable performance.

5 Data analysis

Applying a likelihood based background suppression method to the background data the detector's background rate can be determined. From this the expected background contribution for the sunrise data can be extrapolated. As no excess over the expected background is observed the theoretically expected solar chameleon signal can be used to derive an upper bound on the photon-chameleon coupling by applying the CLs method.

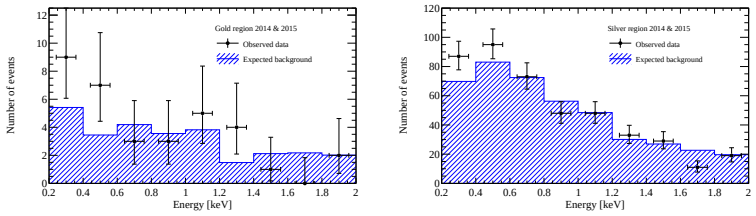

(a) (b)

Figure 1: Expected background and observed spectra for the sunrise solar tracking periods of CAST's 2014 and 2015 data taking campaign, respectively for the *gold* (a) and the *silver* (b) region. Plots are published in [12].

5.1 The expected background

A likelihood based method utilizing event-shape variables [11, 12] is applied to the background data. The background suppression method uses the reference data gained during the characterization in the CAST detector lab [11] and is adjusted in a way that 80 % of real X-rays pass the suppression independently of the X-ray energy. As the background rate varies over the detector's active area with the lowest background level reached in the center, the data has been split in two regions: the inner *gold* region and the *silver* region. Below 2 keV, a background level of 10^{-4} /keV/cm^2/s is reached in the *gold* region. By multiplying the background rates with the total sunrise solar tracking time the expected background can be extrapolated which is shown in Fig. 1 in comparison with the observed data. Clearly, no significant excess over the expected background is observed.

5.2 The expected chameleon signal

Starting with the theoretical solar chameleon spectrum [3, 6] and taking into account the reconversion in CAST, the geometry of CAST's bore and the imaging of the X-ray telescope (especially its efficiency and off-axis behavior) in a simplified raytracing simulation as well as the detector's efficiency and the absorption in the X-ray entrance window the detectable X-ray flux originating from solar chameleons can be computed.

5.3 Expected sensitivity and observed upper bound

To extract an upper bound on the chameleon-photon coupling `TLimit`, the `ROOT` implementation of the CLs method [13, 14], is used. The expected backgrounds and signals as well as the observed data are fed into `TLimit` along with statistical as well as systematical uncertainties. Fig. 2 shows the derived expected and observed upper bounds in comparison to CAST's previous result [6] and the solar luminosity bound. As can be seen, the previous result could be improved by almost a factor of two while for the first time with CAST surpassing the solar luminosity bound. The resulting upper bound on the chameleon-photon coupling is

$$\beta_\gamma < 5.74 \times 10^{10} \tag{1}$$

at 95 % CL and for $1 < \beta_\mathrm{m} < 10^6$ (only non-resonant chameleon production in the Sun is considered here). The full analysis is published in [12].

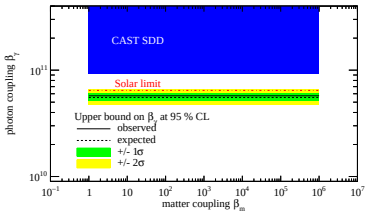

Figure 2: Expected (black dashed line) and observed (black solid line) upper bound on the chameleon photon coupling β_γ at 95 % CL in comparison to CAST's previous limit [6] (blue) and the solar luminosity bound (red dash-dotted line). Plot published in [12].

6 Summary and outlook

Following CAST's first solar chameleon search a GridPix detector has been installed behind one of CAST's X-ray telescope and conducted a solar chameleon search from October 2014 until its dismantling in December 2015. As no significant excess over the expected background could be observed in the solar tracking data, a new and improved upper bound on the chameleon-photon coupling could be derived: $\beta_\gamma < 5.74 \times 10^{10}$ at 95 % CL for $1 < \beta_\mathrm{m} < 10^6$. Thus, CAST's previous result could be surpassed by almost a factor of two.

To continue the search for solar chameleons at CAST an improved GridPix detector has been installed in 2017 implementing several upgrades aiming for lower background levels as well as ultrathin windows have been developed and implemented to increase the detectable solar chameleon flux. In addition, a radiation pressure detector (KWISP), sensitive to β_γ as well as β_m is operated and continuously improved at CAST.

7 Bibliography

References

[1] C. Burrage *et al.*, Living Rev. Relativ. **21**, 1 (2018) doi:10.1007/s41114-018-0011-x.

[2] Ph. Brax *et al.*, Phys. Rev. D **82**, 043007 (2010) doi:10.1103/PhysRevD.82.043007.

[3] Ph. Brax *et al.*, Phys. Rev. D **85**, 043014 (2012) doi:10.1103/PhysRevD.85.043014.

[4] K. Zioutas *et al.*, Nucl. Instr. Meth. Phys. Res. A **425**, 480-487 (1999) doi:10.1016/S0168-9002(98)01442-9.

[5] V. Anastassopoulos *et al.*, Nat. Phys. **13**, 584-590 (2017) doi:10.1038/nphys4109.

[6] V. Anastassopoulos *et al.*, Phys. Lett. B **749**, 172-180 (2015) doi:10.1016/j.physletb.2015.07.049.

[7] C. Krieger *et al.*, Nucl. Instr. Meth. Phys. Res. A **867**, 101-107 (2017) doi:10.1016/j.nima.2017.04.007.

[8] M. Kuster *et al.*, New J. Phys. **9**, 169 (2007) doi:10.1088/1367-2630/9/6/169.

[9] X. Llopart *et al.*, Nucl. Instr. Meth. Phys. Res. A **581**, 485-494 (2007) doi:10.1016/j.nima.2007.08.079.

[10] C. Krieger *et al.*, Nucl. Instr. Meth. Phys. Res. A **729**, 905-909 (2013) doi:10.1016/j.nima.2013.08.075.

[11] C. Krieger *et al.*, Nucl. Instr. Meth. Phys. Res. A **893**, 26-34 (2018) doi:10.1016/j.nima.2018.02.109.

[12] V. Anastassopoulos *et al.*, [arXiv:1808.00066 [hep-ex]].

[13] A. Read, J. Phys. G: Nucl. Part. Phys **28**, 2693 (2002), doi:10.1088/0954-3899/28/10/313.

[14] T. Junk, Nucl. Instr. Meth. Phys. Res. A **434**, 135-443 (1999) doi:10.1016/S0168-9002(99)00498-2.

Exchange-Correlation Effects in Axion Structure Formation

Erik Lentz[1]

[1]Georg-August Universität Göttingen, Göttingen, Deutschland

DOI: http://dx.doi.org/10.3204/DESY-PROC-2018-03/Lentz_Erik

The search for QCD axion dark matter is well underway. Many of these searches require detailed knowledge of the axion's cosmological distribution. However, our understanding of axion structure formation is far from complete, due largely to the candidate's highly-degenerate state. The presentation summarized in this proceedings reveals a new model of structure formation of condensed Bose fluids that includes the effects of exchange and correlation. Theory and preliminary simulations show notable deviations from mean field approaches.

1 Introduction

The QCD axion is a well-motivated candidate to be the cold dark matter (CDM), seeding large scale structures in the visible universe by gravitational infall. As a scalar field of sub-meV mass, relic axions differentiate themselves from most CDM theories as axions form a highly-degenerate fluid at dark matter densities. How to treat degenerate Bose fluids has created a tension in the axion structure formation community. The vast majority of the research holds that QCD axions behave like a pressure-less classical fluid above the Jeans scale ($\lambda_J \sim O$(m - km)) [1, 2, 3]. A much smaller portion of the community hold the in-congruent position that degenerate axions require an inherently quantum description and have unique collective behaviors, even on cosmological scales [4, 5, 6]. Progress towards a consensus has stalled in recent years.

A new model of axion infall may be able to resolve this contention. The model must be simple enough for large simulation covering the breadth of cosmological scales while respecting the peculiar nature of the highly-degenerate axion fluid. Mean field theories are insufficient for this task due to their constraining and correlation-destroying assumptions. Understanding the cosmological context of axion infall is necessary in order to move beyond the mean field.

Axion dynamics are dominated by gravity during the time of significant structure formation from matter domination to the present. It is this the creation of halos and galaxies and the other non-linear structures that are formed during this period that we wish to model. The dominance of gravity in fact traces back to before the radiation-matter transition to the time when axion self and other non-gravitational interactions become feeble, but is sourced with the radiation fields. Without self-interactions the axion particle number becomes conserved and the cold fluid can be well-described by first quantization, namely a many-body quantum mechanics, Fig. 1. A many-body quantum mechanical description of axion infall is the starting point of the presented model.

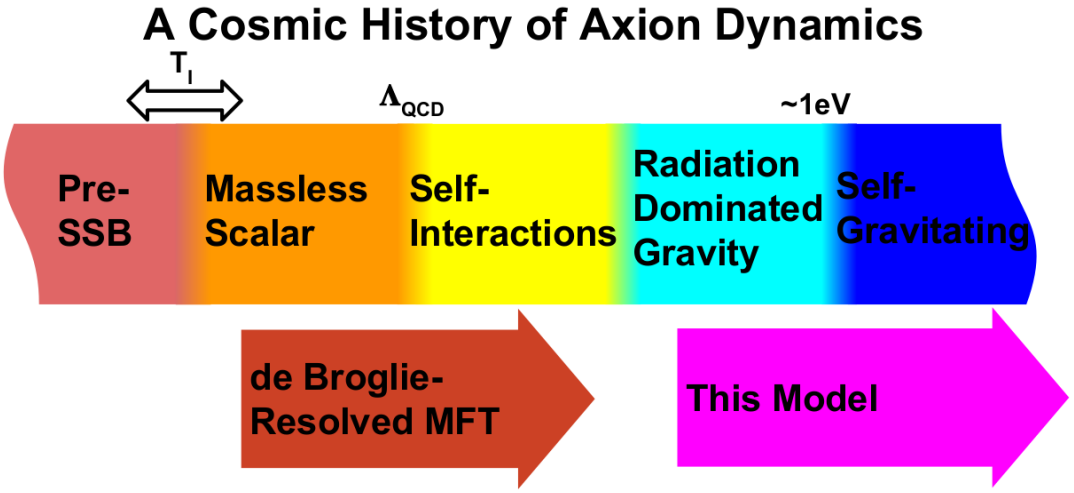

Figure 1: Cosmological history of QCD axion dynamics. Early time and high temperature conditions are to the left, running to late time and cold conditions to the right. It is a typical feature of QCD axion theories that the ordering of inflation (T_I) and the spontaneous symmetry breaking (SSB) of the axion's parent scalar is uncertain. Some time later, the QCD phase transition (Λ_{QCD}) provides the axion field with a mass and consequently its status as a DM candidate. Further cosmic expansion brings the gravity of fluctuations into dominance for the axion, marginalizing the effectiveness of mean field models (MFTs) and highlights the model presented here.

2 The Model and Preliminary Results

A many-body quantum mechanics of self-gravitating axions satisfies a Schrödinger equation,

$$i\partial_t \Psi = -\sum_i^N \frac{\hbar^2 \nabla_i^2}{2m_a a^2}\Psi + \sum_i^N \Phi_{other}(\vec{x}_i)\Psi + \sum_{i<j}^N \phi_a\left(|\vec{x}_i - \vec{x}_j|\right)\Psi \tag{1}$$

plus a particle exchange symmetry between any two axions

$$\Psi\left(\vec{x}_1, ..., \vec{x}_i, ..., \vec{x}_j, ..., \vec{x}_N; t\right) = +\Psi\left(\vec{x}_1, ..., \vec{x}_j, ..., \vec{x}_i, ..., \vec{x}_N; t\right) \quad \forall i, j \tag{2}$$

where Φ_{other} is the gravitational potential from other species and ϕ_a is the inter-axion gravitational potential.

The many-body description may be straight-forwardly transformed to a distribution function on super-de Broglie scales and distilled down to a Boltzmann-like evolution equation for the total density

$$\partial_t f + \vec{v}\cdot\vec{\nabla} f - \vec{\nabla}\bar{\Phi}\cdot\vec{\nabla}_v f - \int d^6 w_2 \vec{\nabla}\Phi_{12}\cdot\vec{\nabla}_v f\left(\tilde{g} - 1\right) f = O(\hbar). \tag{3}$$

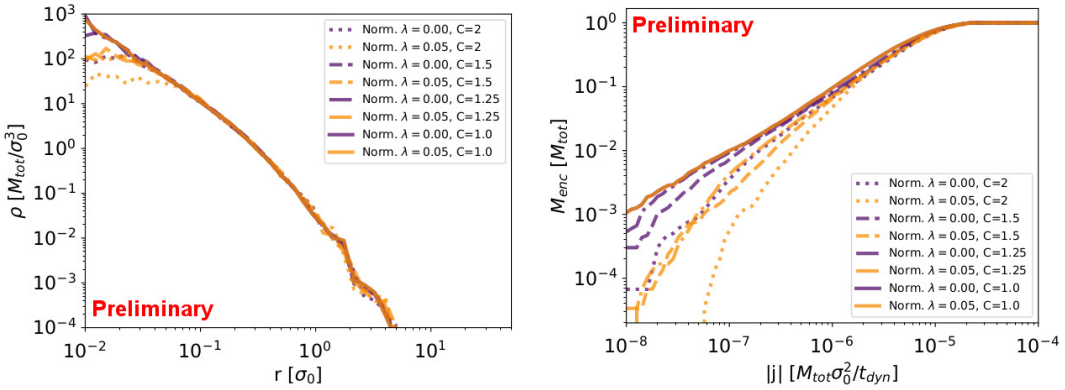

Figure 2: (Left) Spherical density profiles of several collapse simulations. Correlation (C) measures range from trivial at $C = 1$ to highly positively correlated at $C = 2$. The correlation level and spin (λ) track well with the appearance of a halo core. This level of response to angular momentum is not seen among cold dark matter halos. Note that the core scale is emergent much like the concentration in NFW [7], which can also be seen at $r \sim 0.2$. (Right) Enclosed mass angular momentum profiles of the same simulations. Here increased correlation and angular momentum are seen to suppress low angular momentum material relative to the universal cold dark matter shape. All simulations are run with 50,000 particles in a custom direct gravity code. Initial distributions are spherically symmetric, normal, and with spin parameter set according to [9].

Deviations from classical dynamics are due to exchange-correlation (XC) contributions, sourced by the two-body inter-axion correlation function

$$\tilde{g} = \frac{C - \lambda_1 f_+}{1 + \lambda_2 f_+}. \tag{4}$$

where C is the initial correlation of the axion condensate, f_+ is the single-body distribution form summarized over the two phase spaces parameterizing the correlation function, and the λs are Lagrange multipliers set by the normalization of $\tilde{g}f$.

Simulating collapse and virialization may be done via an N-Body technique. Preliminary dark matter only simulations show many structural differences between classical CDM and Bose halos, including the disruption of the universal profiles of radial density and enclosed angular momentum [7, 8], Fig. 2. More specifically, the radial density profile is altered within the virial radius by the presence of a central core, whose emergent scale responds to the spin of the halo in a way that CDM halos do not [10]. The enclosed mass profile also shows significant changes to the angular momentum content of the halo in the form of removal of low angular momentum material, and also shows enhanced sensitivity to the halo spin. The full extent of these new structures, up to the resolution capabilities of the simulations, are still being catalogued. Understanding the XC physics to this resolution is also still underway.

3 Summary

Axion DM structure formation is impacted by exchange-correlation on super-de Broglie scales. The altered dynamics are capable of producing unique structures that survive collapse and virialization. Some of the presented results have recently become available [11, 12]. Keep an eye out for further upcoming publications and future work on this exciting topic!

4 Acknowledgement

Thank you to the Patras workshop organizing committee and host DESY for facilitating the workshop, the University of Göttingen Institute for Astrophysics, the University of Washington Physics and Astronomy Departments, and the U.S. Department of Energy office of High Energy Physics for partial support through DOE grant DE-SC0011665.

References

[1] S. Davidson, "Axions: Bose Einstein condensate or classical field?," Astroparticle Physics **65**, 101 (2015) doi:10.1016/j.astropartphys.2014.12.007 [arXiv:1405.1139].

[2] Guth, A. H. and Hertzberg, M. P. and Prescod-Weinstein, C. "Do dark matter axions form a condensate with long-range correlation?," Phys. Rev. D **92**, 10, 3513 (2015) doi:10.1103/PhysRevD.92.103513 [arXiv:1412.5930].

[3] Hertzberg, M. P., "Quantum and classical behavior in interacting bosonic systems," JCAP **11**, 037 (2016) doi:10.1088/1475-7516/2016/11/037 [arXiv:1609.01342].

[4] Erken, O. and Sikivie, P. and Tam, H. and Yang, Q., "Cosmic axion thermalization," Phys. Rev. D **85**, 6, 063520 (2012) doi:10.1103/PhysRevD.85.063520.

[5] Banik, N. and Sikivie, P., "Cosmic Axion Bose-Einstein Condensation," [arXiv:1501.05913].

[6] Chakrabarty, Sankha S. and Enomoto, Seishi and Han, Yaqi and Sikivie, Pierre and Todarello, Elisa M., "Gravitational self-interactions of a degenerate quantum scalar field," Phys. Rev. D **97**, 4, 3531 (2018) doi:10.1103/PhysRevD.97.043531.

[7] Navarro, J. F. and Frenk, C. S. and White, S. D. M., "The Structure of Cold Dark Matter Halos," ApJ **462**, 563 (1996) doi:10.1086/177173 [arXiv:astro-ph/9508025].

[8] Bullock, J. S. and Dekel, A. and Kolatt, T. S. and Kravtsov, A. V. and Klypin, A. A. and Porciani, C. and Primack, J. R., "A Universal Angular Momentum Profile for Galactic Halos," ApJ **555**, 240B (2001) doi:10.1086/321477 [arXiv:astro-ph/0011001].

[9] Peebles, P. J. E., "Origin of the Angular Momentum of Galaxies," ApJ **155**, 393P (1969) doi:10.1086/149876.

[10] Lentz, E. W. and Quinn, T. R. and Rosenberg, L. J., "The Effects of Angular Momentum on Halo Profiles," ApJ **89**, 822 (2016) doi:10.3847/0004-637X/822/2/89 [arXiv:1603.01322].

[11] Lentz, E. W. and Quinn, T. R. and Rosenberg, L. J., "Condensate Dynamics with Non-Local Interactions," [arXiv:1808.06378].

[12] Lentz, E. W. and Quinn, T. R. and Rosenberg, L. J., "Axion Structure Formation I: The Co-motion Picture," [arXiv:1810.09226].

MADMAX: A new Road to Axion Dark Matter Detection

Béla Majorovits[1] *for the MADMAX collaboration*

[1]MPI for Physics, Germany

DOI: http://dx.doi.org/10.3204/DESY-PROC-2018-03/Majorovits_Bela

Axions with mass around 100 μeV are very well motivated dark matter candidates. Ideas on how to make experiments sensitive in this axion mass range came up only recently. Notably the di-electric haloscope approach seems very promising. The MAgnetized Disc and Mirror Axion eXperiment (MADMAX) collaboration is exploiting this technology to build an experiment sensitive to dark matter axions in the 100 μeV mass range. In this article a short motivation for this axion mass range is given. The basic principles of MADMAX are explained and the current status and plans are reported on.

1 Introduction and Motivation

Arguably, the most elegant solution to the strong CP problem is the Peccei-Quinn (PQ) mechanism which leads to the introduction of the axion-field [1, 2] as a result of spontaneous breaking of a global $U(1)_{PQ}$ symmetry at an energy scale f_{PQ}. In this way the Axion acquires a mass inversely proportional to f_{PQ}. In general there is no a priori prediction for f_{PQ}, resulting in a wide range of possible axion masses. Lower limits on f_{PQ} are given by astrophysical constraints [3] translating into upper limits of the dark matter axion mass of $\approx 10\,\mathrm{meV}$.

In case PQ symmetry is after inflation todays universe would be composed of many patches, which during PQ phase transition were causally disconnected, consequently these patches acquired independent arbitrary θ values. The initial θ-value to be considered in this case is thus the average θ value of all patches of the universe causally connected today, that at time of PQ symmetry breaking were causally disconnected. Unfortunately the prediction is complicated by uncertainties due to additional axions being produced by the decay of *topological defects* (strings and domain walls) hence increasing the axion density significantly. However, latest calculations seem to indicate that for this scenario the axion mass has to be above $25\,\mu$eV [4] and could be around $100\,\mu$eV [5], assuming they make up the bulk of dark matter. Note that the de Broglie wavelength of $100\,\mu$eV axions is a few meters, hence is considerably longer than the size of a typical experiment.

The search for dark matter axions has been pioneered by the ADMX collaboration making use of the coherent E-field oscillation that would be induced through axion-photon conversion by the inverse Primakoff effect [6] - with a frequency determined by the axion mass - inside a magnetized resonant cavity [7]. This approach becomes less sensitive with increasing axion mass as the corresponding photon frequency increases, reducing the volume of the corresponding resonance cavity. Additionally the quality factor of cavities decreases with increasing frequencies.

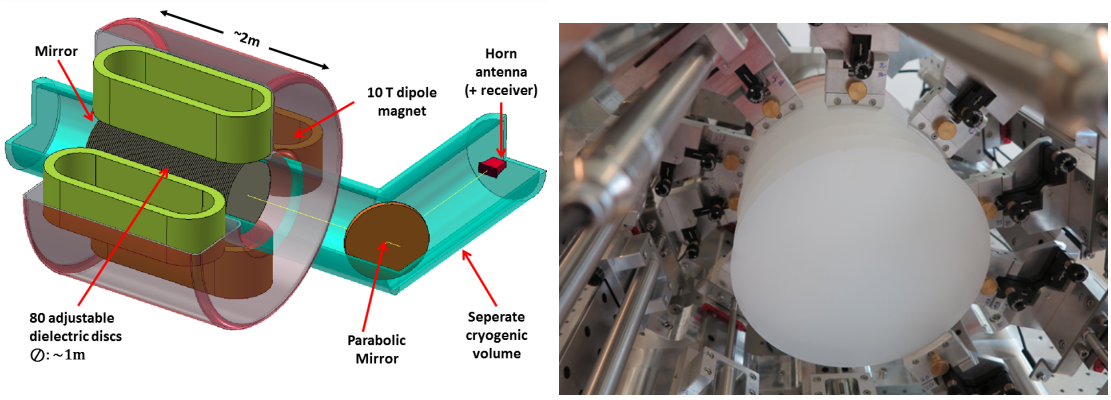

Figure 1: Left: Schematic sketch of MADMAX. Right: Proof of principle booster setup with up to 20 sapphire discs.

Presently it seems this approach is limited to the search of dark matter axion masses below $\approx 40\mu$eV.

Lately the dielectric haloscope approach has been introduced [8], making use of coherent emission of electro-magnetic (EM) waves at the boundaries between media with different di-electric constants: In case such a boundary is placed inside a magnetic field, the axion-induced E-field oscillations would lead to a discontinuity at the boundary due to the change in di-electric constant. As such discontinuities are forbidden, they are compensated by the emission of EM waves with frequency corresponding to the oscillation frequency of the axion-induced E-field.

Assuming axions make up the dark matter of the universe, a perfect mirror ($\epsilon = \infty$) would emit a total power of $\approx 2{\cdot}10^{-27}\mathrm{W/m^2}$ inside a 10 T B-field parallel to the surface [9]. In order to enhance this power, interference effects of coherently emitted waves from multiple surfaces can be utilized. It can be shown that by using a *booster* consisting of a mirror in front of 80 $LaAlO_3$ discs with $\epsilon = 24$ and a dielectric loss of few times 10^{-5} a power boost with respect to a single surface of few times 10^4 could be reached for a frequency range of tens of MHz, thus amplifying the expected emitted axion induced power of such a system to $\approx 10^{-23}$ W [10]. For frequencies between 10 and 40 GHz this is detectable by using low noise HEMT based preamplifiers with a system temperature of ≈ 10 K [11].

2 MADMAX Basics and Status

A schematic sketch of MADMAX and its main components is shown in Fig. 1 (left). A *booster* inside a 4 K cryo-vessel consisting of up to 80 precisely adjustable discs with ≈ 1 mm thickness and $\approx 1\,\mathrm{m}^2$ area in front of a mirror is placed inside the magnet. A parabolic mirror focuses the emitted microwave beam into an antenna transmitting the signal to a receiver system recording the signal.

The MADMAX project is carried out in a staged approach. After the proof of principle and design study phase, it is planned to build magnet and booster prototypes for both, mechanical characterization and verification as well as for first measurements allowing to obtain competitive limits on Axion Like Particles (ALPs)in the mass range between 40 and 120 μeV.

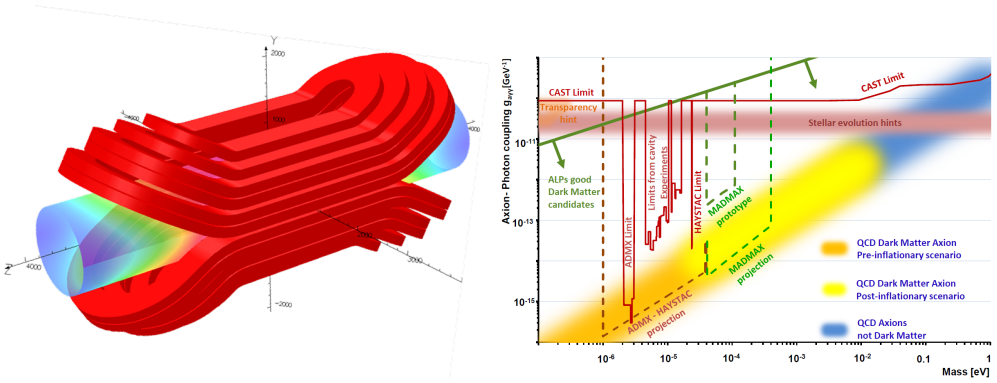

Figure 2: Left: Proposed block design consisting of two halves with 6 individual coils each (red). The color code inside the cylinder displays the B-field strength. Right: Dark matter axion and ALPs search parameter range.

The proof of principle setup consisting of up to 20 sapphire discs with 20 cm diameter connected to precision motors is shown in Fig 1 (right). It is used to test the obtainable precision for the disc placement, ensuring that the corresponding boost of the axion induced power of the system as function of frequency is reproducible. Also diffraction and unwanted reflection effects from antenna and surrounding are being tested. Discs are being adjusted using a positioning algorithm based on comparison of the measured group delay with the one expected from simulations. The algorithm has been applied many times for different number of discs installed. Using this setup it could be shown that the reproducibility of individual disc positions is on the order of a few μm. Using up to five sapphire discs it was demonstrated that the reproducibility of the power boost of the system calculated using the measured EM response each time the system has been re-adjusted is reproducible to better than 5%. Also the frequency of the power boost peak was found to have a variation of less than 5% of the FWHM of the boost factor. Note that these calculations do not consider 3D effects yet. First results of the ongoing work to extrapolate these numbers to higher number of discs, including 3D simulations of realistic setups are encouraging. Such a system can already be used to search for hidden photons with a competitive sensitivite.

The design, development and production of the magnet is being done in the framework of an EU innovation partnership. Two innovation partners, CEA-IRFU, Saclay and Bilfinger Noell are presently close to finishing two independent design studies. Both design studies showed that it is feasible to build a magnet based on a *block design* using NbTi superconductor with the required 100 T^2m^2 and a homogeneity of the field of better than 5%. In both design studies it was shown that the obtained peak fields and forces are consistent with requirements and that the magnet should be cryo-stable. In Fig. 2 (left) the design concept is visualized[1].

A prototype booster system with 20 discs of 30 cm diameter is presently being designed. It is based on the idea of using three precision guide rails per disc. The self supporting booster system can ba slid inside a cryo-vessel. The discs can be positioned using rods attached to specially developed piezo motors, suitable for operation at cryogenic temperatures and in a high B-field. Alternatively it is presently investigated to mount the piezo motors to the discs

[1]Here the Bilfinger-Noell model is shown. Note that the CEA-IRFU model is very similar in design.

directly.

In Phase II a prototype magnet will be built with a reduced aperture and a reduced B-field. After demonstrating the feasibility of the proposed technology such a setup will be used to probe viable parameter space of dark matter ALPs.

A receiver with a total sensitivity to detect within a week a signal at 10-30 GHz with a Lorentzian width of 10^{-6} of the frequency with $\approx 10^{-23}$ W has been built. It is based on heterodyne down-mixing of a liquid helium cooled High Electron Mobility Transistor HEMT-preamplifier (Low Noise Factory) signal being recorded by four samplers with internal FADC for instantaneous FFT conversion of the signal. The contibution of the HEMT preamplifier to the signal temperature is roughly 5 K, while the total system temperature reached is ≈ 10 K. The setup has a dead time of 1.4 %.

DESY Hamburg has offered the MADMAX collaboration to host the experiment. Preparations of the cryogenic infrastructure are already ongoing. First tests and measurements with the prototype booster are presently planned for the year 2022. Also the prototype magnet is scheduled to be available at DESY at this time, allowing to start first measurements for ALPs. The final magnet could be available a few years after that.

3 Sensitivity and Conclusion

With the prototype magnet and booster system a sensitivity in the 40 to 120 μeV ALPs mass range down to $g_{a\gamma\gamma} \approx 10^{-12}\,\mathrm{GeV}^{-1}$ is expected after three years of measurement. The full MADMAX experiment could reach the sensitivity to scan the predicted coupling strength of the KSVZ and DSFZ QCD axion models in the same mass range. The sensitivity to scan even higher axion masses up to 400 μeV can be reached if a detection system is developed that allows to reach the quantum noise level in the frequency range 40 – 100 GHz. Projected sensitivities are displayed together with existing limits and the preferred parameter ranges in Fig. 2 (right).

4 Acknowledgments

The work was partly supported by DFG through SFB 1258 and the Excellence Clusters *Universe* in Munich and *Quantum Universe* in Hamburg.

References

[1] R. Peccei, H. Quinn. Phys. Rev. Lett. **38**, no. 25, 1440 (1977)

[2] F. Wilczek, Phys. Rev. Lett. **40**, 279 (1978)

[3] G. Raffelt, Lecture Notes Phys. **741**, 51 (2008)

[4] V.B. Klaer and G.D. Moore, JCAP **11**, 049 (2017) [arXiv:1708.07521 [hep-ph]].

[5] S. Borsanyi et al., Nature **539**, 69 (2016) [arXiv:1606.07494 [hep-lat]].

[6] P. Sikivie, Phys. Rev. Lett **51**, 1415 (1983); Erratum ibid. **51**, 695 (1983)

[7] ADMX collaboration, Phys. Rev. Lett. **120**, 152301 (2018)

[8] J. Jaeckel and J. Redondo, Phys. Rev. D **88**, 115002 (2013)[arXiv:1308.1103]

[9] D. Horns et al., JCAP **1304**, 016 (2013) [arXiv:1212.2970 [hep-ph]]

[10] A. Millar et al., JCAP **1701**, 061 (2017) [arXiv:1612.07057

[11] A. Caldwell et al., Phys. Rev. Lett. **118**, 091801 (2017), https://www.mpp.mpg.de/fileadmin/user_upload/Forschung/MADMAX/madmax_white_paper.pdf

Axion emission and detection from a Galactic supernova

Pierluca Carenza[1], *Giampaolo Co'*[2,3], *Tobias Fischer*[4], *Maurizio Giannotti*[5], *Alessandro Mirizzi*[1,6]*; *Thomas Rauscher*[7,8]

[1]Dipartimento Interateneo di Fisica "Michelangelo Merlin", Università degli Studi di Bari, Bari, Italy
[2]Dipartimento di Matematica e Fisica "E. De Giorgi", Università del Salento, Lecce, Italy
[3]Istituto Nazionale di Fisica Nucleare - Sezione di Lecce, Lecce, Italy
[4]Institute of Theoretical Physics, University of Wrocław, 50-204 Wrocław, Poland
[5]Physical Sciences, Barry University, 11300 NE 2nd Ave., Miami Shores, FL 33161, USA
[6]Istituto Nazionale di Fisica Nucleare - Sezione di Bari, Bari, Italy
[7]Department of Physics, University of Basel, Basel, Switzerland
[8]Centre for Astrophysics Research, University of Hertfordshire, Hatfield, UK

DOI: http://dx.doi.org/10.3204/DESY-PROC-2018-03/Mirizzi_Alessandro

A Galactic supernova (SN) axion signal would be detected in a future neutrino Mton-class water Cherenkov detector, such as the proposed Hyper-Kamiokande in Japan. The main detection channel for axions is absorption on the oxygen nuclei in the water. The subsequent oxygen de-excitation leads to a potentially detectable gamma signal. In this contribution we present a calculation of the SN axion signal and discuss its detectability in Hyper-Kamiokande.

1 Introduction

Low-mass axions can be copiously produced in a core-collapse supernova (SN) affecting the neutrino burst. In fact, bounds on axions have been placed studying the neutrino signal from SN 1987A. In particular, in [1] it was pointed out that a SN axion burst could produce an observable signal in a neutrino water Cherenkov detector by oxygen absorption. The following oxygen de-excitation would produce a photon signal. Currently it has been proposed a future Mton-class neutrino water Cherenkov detector, Hyper-Kamiokande, in Japan. Motivated by this exciting situation, we find it worthwhile to take a fresh look at the possibility of detecting a SN axion burst. In this contribution we present preliminary results of an updated calculation of the SN axion signal in Hyper-Kamiokande. We refer the interested reader to [2, 3] for further details.

*Speaker

2 SN axion flux

Axions are produced in a SN enviroment via nucleon-bremsstrahlung $NN \to NNa$. The axion-nucleon coupling constant g_{aN} depends on the Peccei-Quinn scale f_a as $g_{aN} = C_N m_N / f_a$, where $N = p, n$, m_N is the nucleon mass and C_N is a model-dependent factor. We computed the axion and neutrino fluxes through a SN simulation developed by the "Wroclaw Supernova Project" based on a spherically symmetric core-collapse SN model, using the AGILE-BOLTZTRAN code [4, 5]. We consider two representative cases:

- Weakly-interacting axions with $g_{ap} = 9 \times 10^{-10}$ and $g_{an} = 0$. In this case, axions are in a free-streaming regime and they drain energy from the SN core, suppressing the neutrino fluxes.
- Strongly interacting axions with $g_{ap} = g_{an} = 10^{-6}$. Axions are in a trapping regime, so they do not reduce the neutrino fluxes. However, they are emitted from a last-scattering surface, the axionsphere. In this case their flux can be larger than the neutrino ones.

3 Axion-^{16}O absorption cross section

Axions can be detected in a water Cherenkov detector via axion-^{16}O absorption, $a\,^{16}\mathrm{O} \to {}^{16}\mathrm{O}^*$, revealing the oxygen decays in photons. The absorption cross section is evaluated starting from the following axion-nucleon interaction Lagrangian [1]

$$\begin{aligned}
\mathcal{L} &= \frac{1}{2f_a}\bar{\Psi}_N \gamma^\mu \gamma^5 (C_0 + C_1 \tau_3) \Psi_N \partial_\mu a \ ; \\
C_0 &= \frac{1}{2}(C_p + C_n) \ ; \\
C_1 &= \frac{1}{2}(C_p - C_n) \ ;
\end{aligned}$$

where Ψ_N is the nucleon spinor and τ_3 is a Pauli matrix. The obtained cross section is

$$\sigma = \frac{4\pi^2 E_p}{f_a^2} |\langle J^P || L_{j,0} || 0^+ \rangle|^2 \ ; \tag{1}$$

where

$$\begin{aligned}
L_{j,0} &= \frac{i}{p} \int d^3 r \, \partial_i (j_j(pr) Y_{j,0}(\Omega)) J^i(\mathbf{r}) \ ; \\
J^i(\mathbf{r}) &= \bar{\Psi}_N(\mathbf{r}) \gamma^i \gamma^5 (C_0 + C_1 \tau_3) \Psi_N(\mathbf{r}) \ .
\end{aligned}$$

The reduced matrix element in Eq. (1) is calculated between the ^{16}O ground state, $|0^+\rangle$, and the $^{16}\mathrm{O}^*$ excited state, $|J^P\rangle$. The angular momentum and parity of the excited oxygen are fixed by conservation laws. Therefore J is the axion angular momentum and $P = (-1)^{J+1}$. The cross section in Eq. (1) is explicitly computed with the Random Phase Approximation. Particle- and γ-emissions from the excited ^{16}O were computed using transmission coefficients from the SMARAGD Hauser-Feshbach code [6]. Two-particle emission was included. The obtained total γ-ray and particle spectra were folded with the detector properties to obtain the expected event number.

4 Axion events

As reference detector we consider Hyper-Kamiokande, a next-generation water Cherenkov detector, with $M = 374\,\mathrm{kton}$ of fiducial mass. The detected neutrino (or axion) events in the proposed detector are calculated as

$$N_{\mathrm{ev}} = F \otimes \sigma \otimes \mathcal{R} \otimes \mathcal{E} \; ;$$

where F, the neutrino (or axion) flux, is convoluted with the cross section σ in the detector, the detector energy resolution, $\mathcal{R}$ and the detector efficiency $\mathcal{E}$. We assume $\mathcal{E} = 1$ above the energy threshold ($E_{\mathrm{th}} = 5\,\mathrm{MeV}$) and the energy resolution is the same of the Super-Kamiokande detector.

With the given energy threshold, the majority of the detectable axion signal falls in the range $5 - 10\,\mathrm{MeV}$. Therefore we restrict our attention to this energy window. The neutrino interaction reactions in the detector are a background for the axion detection. In particular, one has to consider the following channels: inverse beta decay (IBD), $\bar{\nu}_e p \to n e^+$; elastic scattering (ES), $\nu e^- \to \nu e^-$; charged and neutral current ν-^{16}O nuclei interactions (O-CC and O-NC). The number of free-streaming axion and neutrino events in the range $5 - 10\,\mathrm{MeV}$ is shown in Tab. 1. The huge neutrino background dominates the axion signal. However, the axion detectability can be enhanced doping the detector with gadolinium (Gd) to tag the IBD events. This possibility is currently being realized in Super-Kamiokande. We assume that it would occur also for Hyper-Kamiokande. Gd has a large neutron capture cross section and, after a neutron capture, emits a cascade of photons with a total energy of 8 MeV. The coincidence detection of the positron and photon signals tags the IBD events. We will assume 90% tagging efficiency as quoted in [7]. The ES signal can be reduced through a directional cut. Indeed the scattered electrons preserve the incident neutrino direction. Then the majority of ES events (about 95%) is contained in a 40° cone, making possible a reduction of this background by means of a directional cut which eliminates also the 12% of the events in the other channels [8]. The number of events with the background reduction is shown in Tab. 1. We observe that the background reduction makes it possible to detect axions at less than 2σ for a SN at $d = 1\,\mathrm{kpc}$.

Furthermore, a new calculation of the axion bremsstrahlung production in a SN [9], shows that the SN axion flux should be about 20 times lower than the one we used until now. Since the flux in the free-streaming is proportional to g_{ap}^2, to obtain the same luminosity we should use a coupling constant larger by a factor of $\sqrt{20}$. Then the number of axion events is 20 times larger than our previous estimate [Tab. 1]. In this case, the axion signal would emerge at $\sim 28\sigma$ for a SN at 1 kpc and at $\sim 3\sigma$ for a SN at 10 kpc.

We also calculated the events in the trapping regime, obtaining the results in Tab. 2. In this regime the axion signal dominates the neutrino background.

5 Conclusions

We evaluated the Hyper-Kamiokande potential to detect the axion burst associated with a Galactic SN event. We found that axions in the free-streaming regime would be potentially detectable if a careful reduction of the neutrino background is performed. On the other hand, in the trapping regime the axion signal would dominate over the neutrino one, being easily detectable. Therefore a Galactic SN explosion would be a once in a lifetime opportunity for detecting axions.

$g_{ap} = 9 \times 10^{-10}, g_{an} = 0$			
Interaction	Events	BKG RED	NEW FLUX
a-O	270	238	4.76×10^3
IBD	1.99×10^5	1.75×10^4	1.75×10^4
ES	3.53×10^4	1.77×10^3	1.77×10^3
O-CC	1.76×10^3	1.55×10^3	1.55×10^3
O-NC	9.21×10^3	8.10×10^3	8.10×10^3

Table 1: Number of events without background reduction (first column), number of events with background reduction (second column) and number of events with the flux correction factor (third column) in the range $[5; 10]$ MeV for a SN at $d = 1$ kpc and a detector mass $M = 374$ kton.

$g_{ap} = g_{an} = 10^{-6}$	
Interaction	Events
a-O	2.73×10^5
IBD	2.85×10^3
ES	522
O-CC	24
O-NC	116

Table 2: Number of events with background reduction in the range $[5; 10]$ MeV for a SN at $d = 10$ kpc, a detector mass $M = 374$ kton and a coupling constant $g_{ap} = g_{an} = 10^{-6}$.

Acknowledgments

The work of A.M. is supported by the Italian Istituto Nazionale di Fisica Nucleare (INFN) through the "Theoretical Astroparticle Physics" project and by Ministero dell' Istruzione, Università e Ricerca (MIUR). Futhermore, A.M. acknowledges support from the Alexander von Humboldt Foundation for his participation in the Patras Workshop 2018. T.F. acknowledges support from the Polish National Science Center (NCN) under grant numbers UMO-2016/23/B/ST2/00720. The supernova simulations were performed at the Wroclaw Center for Scientific Computing and Networking (WCSS). T.R. is partially supported by the EU COST Action CA16117 (ChETEC).

References

[1] J. Engel *et al.*, Phys. Rev. Lett. **65** (1990) 960.

[2] P. Carenza, "Axion emission and detection from a galactic supernova," Master Thesis (2018).

[3] P. Carenza, G. Cò, T. Fischer, M. Giannotti, A. Mirizzi, and T. Rauscher, in preparation.

[4] M. Liebendoerfer *et al.*, Astrophys. J. Suppl. **150** (2004) 263 [astro-ph/0207036].

[5] T. Fischer *et al.*, Phys. Rev. D **94** (2016) no.8, 085012 [arXiv:1605.08780 [astro-ph.HE]].

[6] T. Rauscher, code SMARAGD, version v0.11.0sn (2018).

[7] J. F. Beacom and M. R. Vagins, Phys. Rev. Lett. **93** (2004) 171101 [hep-ph/0309300].

[8] R. Tomas *et al.*, Phys. Rev. D **68** (2003) 093013 [hep-ph/0307050].

[9] J. H. Chang, R. Essig and S. D. McDermott, arXiv:1803.00993 [hep-ph].

Axion Search with Ring Cavity Experiment

Ippei Obata[1], *Tomohiro Fujita*[2], *Yuta Michimura*[3]

[1]Institute for Cosmic Ray Research, University of Tokyo, Kashiwa 277-8582, Japan
[2]Department of Physics, Kyoto University, Kyoto, 606-8502, Japan
[3]Department of Physics, University of Tokyo, Bunkyo, Tokyo 113-0033, Japan

DOI: http://dx.doi.org/10.3204/DESY-PROC-2018-03/Obata_Ippei

We suggest a novel experimental method to search for axion dark matter with an optical ring cavity. Our cavity measures the difference of the resonant frequencies between two circular-polarizations of the laser beam. Its technical design adopts double-pass configuration to realize a null experiment and reject environmental common-mode noises. We reveal that it can probe the axion-photon coupling constant with a broad range of axion mass $10^{-17}\mathrm{eV} \lesssim m \lesssim 10^{-10}\mathrm{eV}$, up to several orders of magnitude beyond the current limits. We expect that this cavity experiment establishes a new window to develop the axion research.

1 Introduction

We propose a new experiment to search for the coupling of photon to axion dark matter [1]. The axion, motivated by higher dimensional theories, is known to be one of the best candidate of dark matter [2]. Its coherent mode oscillating around the minimum of its potential provides a small difference in the phase velocity between the left-handed and the right-handed photon. Inspired by this photon birefringence effect, we suggest that the optical ring cavity is useful to detect such a small deviation of the phase velocity. Ring cavity experiments have been recently emerged to test the parity-odd Lorentz violation in the photon sector [3]. They have measured the variation of the resonant frequency depending on the direction of the light path. Similar technique can be applied for our purpose, because the resonant frequency of the cavity shifts depending on the polarization of photons, provided that the dark matter axion is coupled to photon. The dark matter axion predicts the phase velocities of the left and right-handed polarized photon shift with the opposite signs and the same magnitude. Therefore such shifts of the resonant frequencies of the polarized laser in the optical cavity are the measurement target in our experiment. The sensitivity curve is in principle determined only by quantum shot noise by virtue of the double-pass configuration and hence we can achieve the great sensitivity level for the detection of the axion-photon coupling constant. We have demonstrated that it can reach sensitivities beyond the current constraints by several orders of magnitude.

2 Phase velocities of photons

In this section, we estimate the phase velocities of two circular-polarized photons coupled with the axion dark matter. The axion-photon coupling term is written as $g_{a\gamma}aF_{\mu\nu}\tilde{F}^{\mu\nu}/4$, where $a(t)$ is the axion field value, $F_{\mu\nu} \equiv \partial_\mu A_\nu - \partial_\nu A_\mu$ is the field strength of vector potential A_μ, and

$\tilde{F}_{\mu\nu} \equiv \epsilon_{\mu\nu\rho\sigma}\partial_\rho A_\sigma/2$ is its dual. Here, we adopt the temporal gauge $A_0 = 0$ and the Coulomb gauge $\nabla \cdot \mathbf{A} = \mathbf{0}$. Then the equation of motion (EoM) for gauge field reads

$$\ddot{A}_i - \nabla^2 A_i + g_{a\gamma}\dot{a}\epsilon_{ijk}\partial_j A_k = 0\,, \quad \text{“}\cdot\text{”} = d/dt\,. \tag{1}$$

The present background axion field is given by $a(t) = a_0\cos(mt + \delta_\tau(t))$ with its constant amplitude a_0, its mass m and a phase factor $\delta_\tau(t)$. Note that we assume δ_τ to be a constant value within the coherence timescale of dark matter $\tau = 2\pi/(mv^2) \sim 1\,\text{year}(10^{-16}\text{eV}/m)$.

Decomposing A_i into two helicity modes with the wave number $\mathbf{k}$, we find EoMs for the two polarization modes $A_k^\pm$ as

$$\ddot{A}_k^\pm + \omega_\pm^2 A_k^\pm = 0\,, \quad \omega_\pm^2 \equiv k^2\left(1 \pm \frac{g_{a\gamma}a_0 m}{k}\sin(mt+\delta_\tau)\right) \tag{2}$$

and obtain the difference of their phase velocities $\delta c \equiv |c_+ - c_-|$. Since the coupling constant $g_{a\gamma}$ is tiny, δc is approximately given by

$$\delta c \simeq \frac{g_{a\gamma}a_0 m}{k}\sin(mt+\delta_\tau) \equiv \delta c_0 \sin(mt+\delta_\tau)\,. \tag{3}$$

Therefore, with the wavelength $\lambda = 2\pi/k = 1550$ nm we can estimate

$$\delta c_0 \simeq 3\times 10^{-24}\left(\frac{g_{a\gamma}}{10^{-12}\ \text{GeV}^{-1}}\right)\,, \tag{4}$$

where we used the present energy density of the axion dark matter, $\rho_a = m^2 a_0^2/2 \simeq 0.3\ \text{GeV/cm}^3$.

3 Optical ring cavity search for axion dark matter

In this section, we describe our experiment to detect δc caused by the axion dark matter and calculate the sensitivity to the axion-photon coupling constant. The setup of our experiment is schematically illustrated in Figure 1. First, we create a incident laser beam which is circularly polarized by a 1/4 waveplate. The incident beam to the cavity is partially reflected by the input mirror and goes to the photodetector A, while the other part enters the cavity which eventually goes to either the photodetector A or the mirror on the far right. And the beam which is reflected from the mirror on the far right is partially reflected into the photodetector B or re-enters the cavity, and finally some part of the beam goes into the photodetector B. Note that the beam changes its polarization each time when it is reflected by a mirror. Considering this effect, we stretch the bow-tie optical path in the longitudinal direction in order to make the dominant polarization states at each photodetector. For instance, we can make the laser beam entering the detector A right-handed polarization most of the time, while the other laser beam left-handed polarization going into the detector B. Without the phase velocity modulation δc given by the axion dark matter, the resonant frequency would not depend on the circular-polarizations. Therefore our setup works as a null-experiment sensitive to the axion-photon coupling.

In our setup, most of the environmental noises are also cancelled due to the double-pass configuration [4], because the second error signal observes only the difference in the resonant frequency between the two counter-propagating optical paths in the cavity and their common

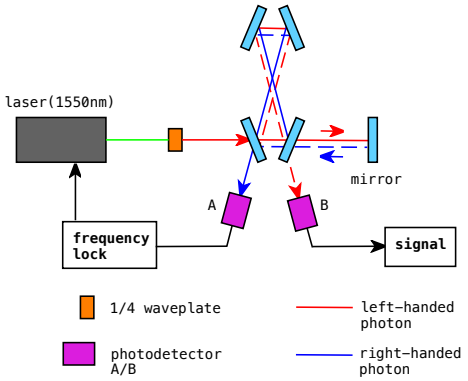

Figure 1: The layout of our double-pass bow-tie cavity. The left-handed beam (solid line) is injected to the resonant cavity, while the transmit beam reflected by the mirror on the far right goes to the cavity as the right-handed beam (dashed line). The photodetector A is used to lock the laser frequency at the resonant frequency for the injected beam from the left, and the photodetector B monitors the modulation of the resonant frequency difference of two optical paths from the beam coming from the right.

fluctuations become irrelevant. Then the primary source of noise is the quantum shot noise. One-sided spectrum of the shot noise of an optical ring cavity is written as [5]

$$\sqrt{S_{\rm shot}} = \sqrt{\frac{\lambda}{4\pi P}\left(\frac{1}{t_r^2}+\omega^2\right)}\,, \qquad t_r = \frac{L\mathcal{F}}{\pi}\,, \tag{5}$$

where λ is the laser wavelength, P is the input power, and ω is the angular frequency which is the axion mass m in our case. Note that the quantum radiation pressure noise is cancelled out by our double-pass configuration. The averaged round-trip time t_r is characterized by the cavity round-trip length L and the finesse $\mathcal{F}$. If our measurement is limited by the shot noise, the signal-to-noise ratio (SNR) improves with the measurement time $T^{1/2}$ as long as the axion oscillation is coherent for $T \lesssim \tau$. When the measurement time becomes longer than this coherence time $T > \tau$, the phase δ_τ is not constant any more and δ_τ will behave as a random variable staying constant for each period of τ. As a consequence, the growth of the SNR with the measurement time changes as $(T\tau)^{1/4}$ [6]. Therefore the sensitivity to $\delta c_0/c$ is limited by

$$\frac{\delta c_0}{c} \lesssim \begin{cases} \dfrac{2}{\sqrt{T}}\sqrt{S_{\rm shot}} & (T \lesssim \tau) \\ \dfrac{2}{(T\tau)^{1/4}}\sqrt{S_{\rm shot}} & (T \gtrsim \tau) \end{cases} \longleftrightarrow \quad g_{a\gamma} \lesssim \begin{cases} 10^{12}\sqrt{\dfrac{S_{\rm shot}}{T}}\ [1/{\rm GeV}] & (T \lesssim \tau) \\ 10^{12}\sqrt{\dfrac{S_{\rm shot}}{(T\tau)^{1/2}}}\ [1/{\rm GeV}] & (T \gtrsim \tau) \end{cases}. \tag{6}$$

In this experiment, we search for the axion dark matter with the mass $m \lesssim 10^{-10}$eV corresponding to the frequency range $f \simeq 2.4\,{\rm Hz}(m/10^{-14}{\rm eV})$. Figure 2 shows the sensitivity of our experiment to the axion-photon coupling constant for different configurations. Here we set $\lambda = 1550$ nm and assumed $T = 1$ year $= 3\times10^7$ sec. With feasible parameters we can achieve a sensitivity level $g_{a\gamma} \simeq 3\times10^{-13}$ GeV^{-1} for $m \lesssim 10^{-16}$ eV, which is below the current constraints from axion helioscope experiments, SN1987A and *Chandra* X-ray observations. Moreover, with more optimistic parameters, our cavity can reach $g_{a\gamma} \simeq 3\times10^{-16}$ GeV^{-1} for $m \lesssim 10^{-16}$ eV which will be the best sensitivity among the proposed axion search experiments in this mass range. We note here that various technical noises at low frequency should be further investigated to determine the sensitivity for lower mass range of the axion. We leave this issue for future work.

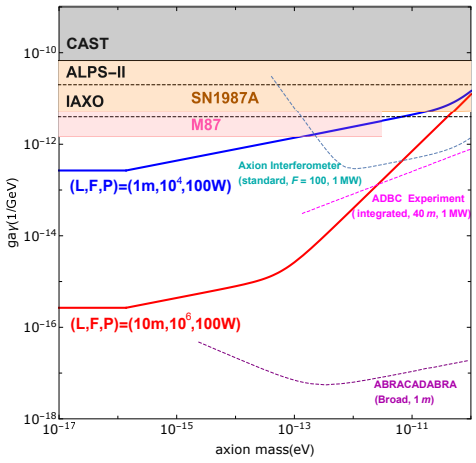

Figure 2: The sensitivity curves for the axion-photon coupling constant $g_{a\gamma}$ with respect to the axion mass m. The solid blue (red) line shows the sensitivity of our experiment $(L, F, P) = (1(10)\ \mathrm{m}, 10^4(10^6), 10^2(10^2)\ \mathrm{W})$. The gray band represents the current limit from CAST [7]. The dashed black lines are the prospected limits of IAXO [8] and ALPS-II [9] missions. The dashed blue, magenta and purple lines show the proposed reaches of axion optical interferometers [10], birefringent cavities [11] and ABRACADABRA magnetometer [12]. The orange and pink bands denote the astrophysical constraints from the cosmic ray observations of SN1987A [13] and radio galaxy M87 [14].

4 Acknowledgments

In this work, YM and TF are supported by the JSPS Grant-in-Aid for Scientific Research (B) No. 18H01224 and Grant-in-Aid for JSPS Research Fellow No. 17J09103, respectively.

References

[1] I. Obata, T. Fujita and Y. Michimura, Phys. Rev. Lett. **121**, no. 16, 161301 (2018).

[2] D. J. E. Marsh, Phys. Rept. **643**, 1 (2016).

[3] F. N. Baynes, M. E. Tobar and A. N. Luiten, Phys. Rev. Lett. **108**, 260801 (2012); Y. Michimura, N. Matsumoto, N. Ohmae, W. Kokuyama, Y. Aso, M. Ando and K. Tsubono, Phys. Rev. Lett. **110**, no. 20, 200401 (2013); Y. Michimura, M. Mewes, N. Matsumoto, Y. Aso and M. Ando, Phys. Rev. D **88**, no. 11, 111101 (2013).

[4] B. J. Cusack, D. A. Shaddock, B. J. J. Slagmolen, G. de Vine, M. B. Gray and D. E. McClelland, Class. Quant. Grav. **19**, 1819 (2002).

[5] H. J. Kimble, Y. Levin, A. B. Matsko, K. S. Thorne and S. P. Vyatchanin, Phys. Rev. D **65**, 022002 (2002).

[6] D. Budker, P. W. Graham, M. Ledbetter, S. Rajendran and A. Sushkov, Phys. Rev. X **4**, no. 2, 021030 (2014).

[7] K. Zioutas *et al.* [CAST Collaboration], Phys. Rev. Lett. **94**, 121301 (2005); V. Anastassopoulos *et al.* [CAST Collaboration], Nature Phys. **13**, 584 (2017).

[8] J. K. Vogel *et al.*, arXiv:1302.3273 [physics.ins-det].

[9] K. Ehret *et al.* [ALPS Collaboration], Nucl. Instrum. Meth. A **612**, 83 (2009); R. Bahre *et al.*, JINST **8**, T09001 (2013).

[10] W. DeRocco and A. Hook, Phys. Rev. D **98**, no. 3, 035021 (2018).

[11] H. Liu, B. D. Elwood, M. Evans and J. Thaler, arXiv:1809.01656 [hep-ph].

[12] Y. Kahn, B. R. Safdi and J. Thaler, Phys. Rev. Lett. **117**, no. 14, 141801 (2016).

[13] A. Payez, C. Evoli, T. Fischer, M. Giannotti, A. Mirizzi and A. Ringwald, JCAP **1502**, no. 02, 006 (2015).

[14] M. C. D. Marsh, H. R. Russell, A. C. Fabian, B. P. McNamara, P. Nulsen and C. S. Reynolds, JCAP **1712**, no. 12, 036 (2017).

Rare Low-Energy Event Searches with the Majorana Demonstrator

Gulden Othman[1]*, on behalf of the* Majorana *collaboration*

[1]University of North Carolina at Chapel Hill, USA

DOI: http://dx.doi.org/10.3204/DESY-PROC-2018-03/Othman_Gulden

The Majorana Demonstrator is currently searching for neutrinoless double-beta decay in ^{76}Ge and will demonstrate the feasibility to deploy a tonne-scale experiment in a phased and modular fashion. It consists of two modular arrays of natural and ^{76}Ge-enriched germanium detectors totaling 44.1 kg, of which 29.7 kg is enriched, located at the 4850' level of the Sanford Underground Research Facility in Lead, South Dakota, USA. The low-backgrounds and low trigger thresholds (<1 keV) achieved by the Demonstrator allow for additional rare-event searches at low-energies, e.g. searches for WIMPs, bosonic dark matter, and solar axions. In this work, we will present results and ongoing efforts related to these rare-event searches and discuss the future reach of Majorana.

1 The Majorana Demonstrator

The Majorana Demonstrator [1] is a search for neutrinoless double-beta decay ($0\nu\beta\beta$) in ^{76}Ge currently operating at the 4850' level of the Sanford Underground Research Facility (SURF) in Lead, SD, USA. The goals of the Majorana Demonstrator are to demonstrate backgrounds low enough to justify building a tonne-scale experiment, to demonstrate the feasibility to construct modular arrays of high-purity Ge (HPGe) detectors, and for additional searches for physics beyond the Standard Model (SM). The Majorana Demonstrator employs 44.1 kg P-type point contact (PPC) HPGe detectors, 29.7 kg of which is enriched to 88% ^{76}Ge. The detectors are arranged into two separate cryostats constructed of ultra pure underground electroformed copper (UGEFCu). Starting from the innermost region, two cryostat modules are surrounded by an inner layer of electroformed copper, an outer layer of commercial copper, lead, an active muon veto, borated polyethylene, and polyethylene.

The Majorana Demonstator is currently operating with the best energy resolution of any $0\nu\beta\beta$ experiment with an energy resolution of 2.5 keV FWHM at 2039 keV, the Q-value for $0\nu\beta\beta$ in ^{76}Ge. Recent results released at the Neutrino 2018 conference include a blind analysis of data with 26 kg-yr enriched exposure (11.85 kg-yr blind data). An observed background rate of 15.4 $\pm$ 2.0 cts/FWHM t yr was found near the ^{76}Ge Q-value for a full exposure limit on the half life of $T^{0\nu}_{1/2} > 2.7 \times 10^{25}$ [2, 3].

2 The MAJORANA Low-Energy Program

The low backgrounds and detector thresholds achieved by the MAJORANA DEMONSTRATOR allow for additional searches for physics beyond the SM at low-energies (<100 keV). These include searches for bosonic dark matter, Pauli exclusion principle violation, electron decay, solar axions [4], and light (∼10 GeV/c^2) WIMPs. Careful material selection and handling, as well as extreme care taken to reduce the amount of cosmogenic activation in the enriched detectors results in low-backgrounds down to low-energies. Additionally, the low-capacitance achieved by PPC detector technology coupled with the development of a low-noise, low-mass front-end [5] enable low trigger thresholds (<1 keV) and excellent energy resolution (0.4 keV FWHM at 10.4 keV). Excellent pulse-shape analysis abilities enable further background discrimination.

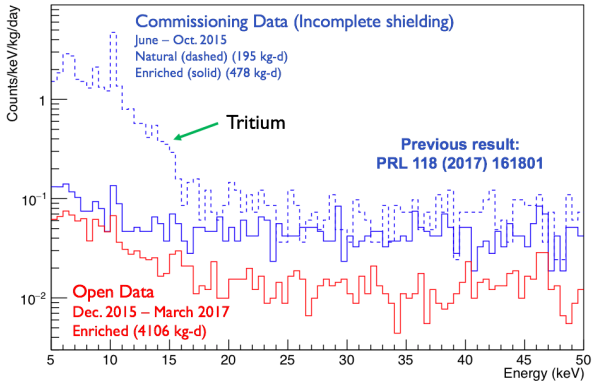

Figure 1: Spectrum from 5-50 keV of data from the MAJORANA DEMONSTRATOR. Data shown solid (dashed) blue is from commissioning data before shielding was completed from enriched (natural) detectors. Data in red is after the addition of the inner electroformed copper shield.

3 Previous Results

The MAJORANA background spectrum from 5-50 keV is shown in Fig. 1. There is a clear difference visible in the enriched and natural detectors due to the fact that, unlike the enriched detectors, the natural detectors had a much longer surface exposure, resulting in increased cosmogenic activation.

The MAJORANA collaboration has set limits on bosonic dark matter [4]. This is accomplished by searching for peaks at the mass of the dark matter particle in the spectrum, which is assisted by the excellent energy resolution of the MAJORANA detectors. The spectrum in solid blue in Fig. 1 was used to set the previous limits on pseudoscalar bosonic dark matter shown as the solid red line in Fig. 2. The dotted black line shows the projected sensitivity using new data with 9497 kg-d of exposure including blind data, assuming a background rate of 0.01 cts/keV/kg/d.

In addition to dark matter, the MAJORANA collaboration has set limits on lightly-ionizing particles (LIPs). LIPs are theoretical particles whose electromagnetic interactions are suppressed compared to the normal interaction strength. This would manifest experimentally as particles which have a fractional charge compared to the fundamental charge. Limits are typi-

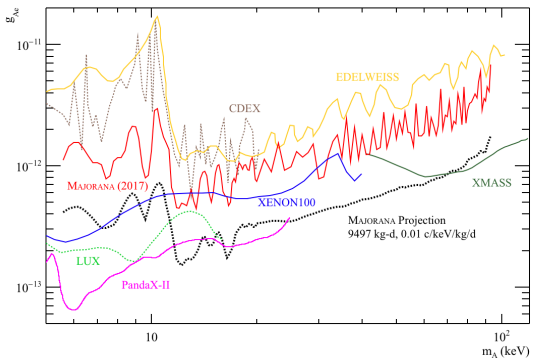

Figure 2: Current MAJORANA limits (red) and sensitivity projections based on exposure (dotted black) for pseudoscalar bosonic dark matter.

cally set based on a reduction factor f. The charge q detected is related to the reduction factor f by $q = e/f$, where e is the fundamental charge. The MAJORANA DEMONSTRATOR completed a background free search for LIPs resulting in the limit shown in Fig. 3 [6].

4 Ongoing Analyses

In addition to the results shown in the previous section, the MAJORANA collaboration is working on pulse-shape analysis efforts to further reduce backgrounds at low-energies in order to improve the analysis thresholds. Lower analysis thresholds would enable a host of additional searches at low energies, including searches for solar axions and low-mass WIMPs.

The MAJORANA collaboration is able to search for solar axions through two different coupling mechanisms: the Primakov effect as well as axio-electric effect. Solar axions can be detected via the Coherent Primakoff effect, even without exact knowledge of the directions of the crystal axes, if there are more than about 15 detectors [7]. In this case, the true total axion rate can be approximated by averaging angle-specific rates over all possible angles. This would manifest experimentally as a time-dependent spectrum with signals expected between 3-10 keV. Additionally, solar axions can be detected via the axio-electric effect [8]. This is analogous to the photoelectric effect, in that an axion is absorbed and the energy is released as electrons. This would manifest as characteristic peaks in a spectrum below 15 keV.

The MAJORANA DEMONSTRATOR is also sensitive to low-mass WIMPs ($\sim$10 GeV/c^2). Though the DEMONSTRATOR is unable to distinguish between events originating from nuclear recoils and those due to electron recoils, the low intrinsic backgrounds will enable a search which can provide an important check for experiments searching for WIMPs using Ge.

Acknowledgments

This material is based upon work supported by the U.S. Department of Energy, Office of Science, Office of Nuclear Physics, the Particle Astrophysics and Nuclear Physics Programs of

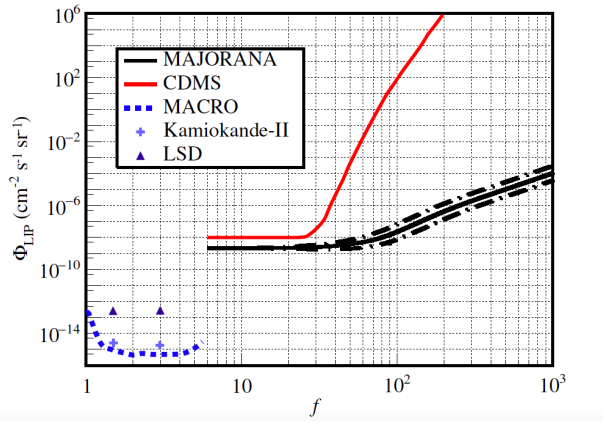

Figure 3: The MAJORANA 90% confidence interval (solid black) and 1σ uncertainty bands (dashed black) for Lightly Ionizing Particles [6].

the National Science Foundation, and the Sanford Underground Research Facility. This work is also funded by the National Science Foundation Graduate Research Fellowship Program under grant number DGE-1144081.

References

[1] N. Abgrall et al. The Majorana Demonstrator Neutrinoless Double-Beta Decay Experiment. *Adv. High Energy Phys.*, 2014:365432, 2014.

[2] C. E. Aalseth et al. Search for Neutrinoless Double-β Decay in ^{76}Ge with the Majorana Demonstrator. *Phys. Rev. Lett.*, 120(13):132502, 2018.

[3] Vincente Guiseppe. New Results from the MAJORANA DEMONSTRATOR Experiment. *Zenodo*, http://doi.org/10.5281/zenodo.1286900, June 2018.

[4] N. Abgrall et al. New limits on bosonic dark matter, solar axions, pauli exclusion principle violation, and electron decay from the majorana demonstrator. *Phys. Rev. Lett.*, 118:161801, Apr 2017.

[5] P. Barton et al. Low-noise low-mass front end electronics for low-background physics experiments using germanium detectors. In *2011 IEEE Nuclear Science Symposium Conference Record*, pages 1976–1979, Oct 2011.

[6] S. I. Alvis et al. First limit on the direct detection of lightly ionizing particles for electric charge as low as $e/1000$ with the majorana demonstrator. *Phys. Rev. Lett.*, 120:211804, May 2018.

[7] Wenqin Xu and Steven R. Elliott. Solar axion search technique with correlated signals from multiple detectors. *Astroparticle Physics*, 89:39 – 50, 2017.

[8] Javier Redondo. Solar axion flux from the axion-electron coupling. *JCAP*, 1312:008, 2013.

On the Mass and Size of Axion Miniclusters

Andreas Pargner[1], *Thomas Schwetz*[1]

[1]Institut für Kernphysik, Karlsruher Institut für Technologie, Germany

DOI: http://dx.doi.org/10.3204/DESY-PROC-2018-03/Pargner_Andreas

We present results of a semi-analytical calculation of the axion energy density from the realignment mechanism in a post-inflationary Peccei-Quinn symmetry breaking scenario. Together with a modified Press & Schecter method, the power spectrum of the energy density fluctuations is used to derive the distribution of axion miniclusters in mass and size.

1 Introduction

The nature of Dark Matter in our Universe is one of the biggest puzzles of modern physics. Among the best motivated Dark Matter candidates is the axion which emerges as pseudo Nambu-Goldstone boson in Peccei and Quinn's solution of the strong CP problem [1, 2]. In invisible axion models the interaction between the axion and the Standard Model particles is suppressed by the high Peccei-Quinn symmetry breaking scale f_a [3, 4]. The mass of the axion is generated by the mixing with the other mesons around QCD around phase transition. At higher temperatures the axion is effectively massless.

One of the most prominent cosmological production mechanisms of axions is vacuum realignment. When the Peccei-Quinn symmetry is broken at the scale f_a, the axion field a takes some random value $a/f_a \in [-\pi, \pi]$. Around the QCD phase transition, the potential will force the axion field to roll down to the CP conserving minimum. The coherent oscillations around this minimum can be identified as the Dark Matter axions. See Ref. [5] for a thorough review on axion cosmology.

If the vacuum realignment happens after an inflationary epoch, the axion field takes different values in causally disconnected regions. In that case the axion field resembles white noise on scales larger than the horizon. This leads to large isocurvature fluctuations in the axion energy density. The large overdensities can decouple from the Hubble flow already in the radiation dominated era and form gravitationally bound objects, which are called axion miniclusters [6]. Relating the size of the minicluster to the Hubble horizon at the time the axion starts to oscillate, the mass can be estimated to be around $M_{\rm MC} \sim 10^{-10}\, M_\odot$ for a typical Peccei-Quinn breaking scale $f_a \sim 10^{12}\,\text{GeV}$.

The specific properties of axion miniclusters were first studied in detail by Kolb and Tkachev in Ref. [7]. For recent work on axion miniclusters see, for example, Refs. [8, 9]. In this article we present the main results of Ref. [10] where the distribution of axion miniclusters in mass and size is derived.

2 Axion Energy Density and Power Spectrum

Defining the misalignement field $\theta = a/f_a$, the axion potential created by QCD effects

$$V(\theta) = m_a^2(T)\,(1 - \cos\theta) \tag{1}$$

is approximately harmonic for small θ, i.e. $V(\theta) \simeq m_a^2(T)\theta^2/2$. Note that in the harmonic approximation all non-linear effects, like the formation of cosmic strings and domain walls, are neglected. The temperature dependent axion mass $m_a^2(T) = \chi_{\rm QCD}(T)/f_a$ is determined by the topological susceptibility of QCD $\chi_{\rm QCD}(T)$ and the Peccei-Quinn breaking scale f_a. For temperatures $T \gtrsim T_{\rm QCD} \sim 200\,{\rm MeV}$, the mass m_a switches on exponentially and reaches its zero temperature value $m_a \sim 5.7 \cdot 10^{-6}\,{\rm eV}\left(10^{12}\,{\rm GeV}/f_a\right)$ at $T \lesssim T_{\rm QCD}$. The explicit temperature dependence of $\chi(T)$ and therefore $m_a(T)$ was recently derived in Ref. [11] with state of the art lattice calculations.

Using the harmonic approximation for the axion potential, the evolution equation for the Fourier modes θ_k of the misalignment field in a flat Friedmann-Robertson-Walker background is

$$\ddot{\theta}_k + 3H(T)\dot{\theta}_k + \frac{k^2}{A^2}\theta_k + m_a^2(T)\theta_k = 0\,, \tag{2}$$

where A is the scale factor and $H(T) \equiv \dot{A}/A$ is the Hubble rate. In post-inflation realignemnt, the initial conditions for θ_k have to be chosen such that they reflect the white noise character of the misalignment field. Namely, that θ has a random value between $-\pi$ and π from one horizon to another, but is constant therein. This can be done by assuming a specific power spectrum $P_\theta(k)$ for the Fourier modes via the relation:

$$\langle \theta_k \theta^*_{k'} \rangle = (2\pi)^3 \delta^3(k - k') P_\theta(k)\,, \tag{3}$$

where $\langle\cdot\rangle$ denotes a statistical average. In Ref. [10], a Gaussian power spectrum with exponential suppression for high modes $k > K$ is applied. Where $K \equiv a_i H_i$ reflects the size of the horizon at the initial time. Optimally, the intial time for solving the evolution equation should be the time of Peccei-Quinn symmetry breaking. But since $f_a \gg T_{\rm QCD}$, one would have follow the field evolution over many orders of magnitude. This is numerically not feasible. Assuming that the misalignment field keeps its white noise character also at later times, the evolution equation can be solved starting at some temperature $T_i \gtrsim T_{\rm QCD}$ with the above described initial conditions.

Under this assumption one can solve the evolution equation mode by mode and calculate the energy density of misalignemnt axions ρ, using the statistical porperties of the θ_k. With the above described method it is also possible to determine the power spectrum $P(q)$ of the density fluctuations:

$$P(q) = \frac{1}{V}\frac{\langle|\rho_q|^2\rangle}{\bar{\rho}^2} = 2(2\pi)^3 \frac{\int d^3k\ P_\theta(|\vec{k}|)P_\theta(|\vec{k}-\vec{q}|)\,F(k,k-q)^2}{\left[\int d^3k\ P_\theta(k)F(k,k)\right]^2}\,, \tag{4}$$

where F is a function determined by the evolution of the Fourier modes and $\bar{\rho}$ is the mean energy density

The result is shown in left panel of Fig. 1. We observe the expected impact of the random field on the energy density. For small wavenumbers q, we have essentially a constant power spectrum, as expected for white noise. For large q, i.e. small scales, we see that $P(q)$ suddenly drops off, meaning that the energy density fluctuations are correlated on these scales. The position of the shoulder of $P(q)$ indicates the characteristic size of the inhomogeneities.

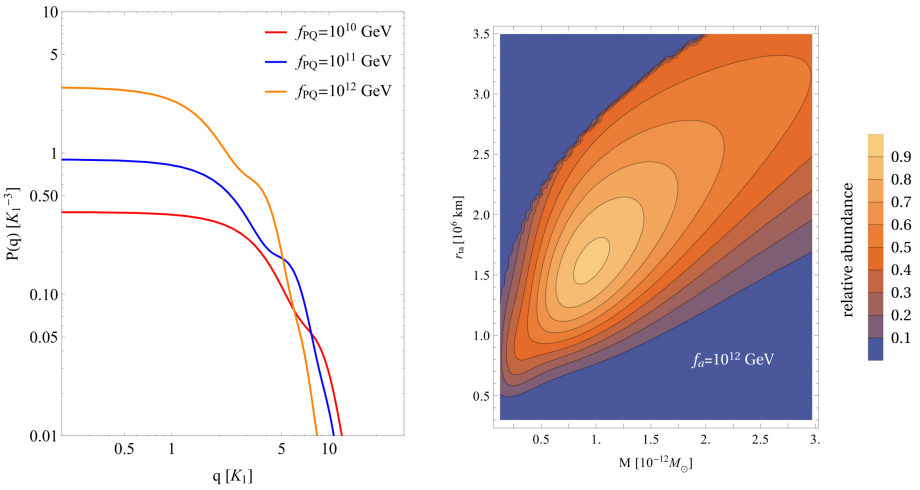

Figure 1: Left Panel: Power spectrum of the axion energy density fluctuations. $K_1 = aH(T = 1\,\mathrm{GeV})$ is a reference scale. Right Panel: Distribution of Axion Miniclusters in Mass and Size. Similar Plots can be found in Ref. [10]

3 Size and Mass of Axion Miniclusters

With the power spectrum of the energy density fluctuations $P(q)$ at hand, one can calculate the mass function of collapsed objects via the Press & Schechter method [12]. But this approach has disadvantages for calculating the mass function of axion miniclusters. First, the overdensities in the misalignment energy density are not small. Thus, a linearization of the decoupling process is not possible. Further, the fluctations can collpase already in the radiation dominated epoch. Second, in the standard Press & Schechter method a one to one relation between size and mass of collapsed objects is assumed. This should be relaxed when dealing with large fluctuations. Using the methods of [13], where collapse during and after radiation domination is conisdered, one can calculate the time when a fluctuation δ of given mass and size decouples from the Hubble flow. In Ref. [10] this was used to derive a formula for the double differential mass function $\mathrm{d}n/(\mathrm{d}M\mathrm{d}R)$. It describes the distribution of collapsed objects not only in mass but also in size.

The right panel of Fig. 1 shows the results for the two dimensional distribution function of axion miniclusters setting the Peccei-Quinn breaking scale to $f_a = 10^{12}\,\mathrm{GeV}$. It is peaked around a characteristic mass and turn around radius. Doing the calculation for different breaking scales, one can identify typical intervals for size and mass. The turn around radii cover about one order of magnitude, whereas the minicluster masses span up to three orders of magnitude around the peak value. For the peak value, we observe that the size is somewhat smaller than the estimate by the horizon at the time the oscillations commence. For the same reason the miniclusters seem also a little lighter than naively expected. We find $M_{\mathrm{MC}} \sim 8 \cdot 10^{-13}\,M_\odot$ for $f_a \sim 10^{-12}\,\mathrm{GeV}$.

Acknowledgements

This project has received funding from the European Unions Horizon 2020 research and innovation programme under the Marie Sklodowska-Curie grant agreement No 674896 (Elusives). A.P. acknowledges the support by the DFG-funded Doctoral School KSETA.

References

[1] R. D. Peccei and H. R. Quinn, *Constraints Imposed by CP Conservation in the Presence of Instantons*, *Phys. Rev.* **D16** (1977) 1791–1797.

[2] F. Wilczek, *Problem of Strong P and T Invariance in the Presence of Instantons*, *Phys. Rev. Lett.* **40** (1978) 279–282.

[3] M. Dine, W. Fischler, and M. Srednicki, *A simple solution to the strong CP problem with a harmless axion*, *Physics Letters B* **104** (1981), no. 3 199 – 202.

[4] M. Shifman, A. Vainshtein, and V. Zakharov, *Can confinement ensure natural CP invariance of strong interactions?*, *Nuclear Physics B* **166** (1980), no. 3 493 – 506.

[5] D. J. E. Marsh, *Axion Cosmology*, *Phys. Rept.* **643** (2016) 1–79, [1510.07633].

[6] C. J. Hogan and M. J. Rees, *Axion Miniclusters*, *Phys. Lett.* **B205** (1988) 228–230.

[7] E. W. Kolb and I. I. Tkachev, *Axion Miniclusters and Bose Stars*, *Phys. Rev. Lett.* **71** (1993) 3051–3054, [hep-ph/9303313].

[8] K. M. Zurek, C. J. Hogan, and T. R. Quinn, *Astrophysical Effects of Scalar Dark Matter Miniclusters*, *Phys. Rev.* **D75** (2007) 043511, [astro-ph/0607341].

[9] M. Fairbairn, D. J. E. Marsh, and J. Quevillon, *Searching for the QCD Axion with Gravitational Microlensing*, *Phys. Rev. Lett.* **119** (2017), no. 2 021101, [1701.04787].

[10] J. Enander, A. Pargner, and T. Schwetz, *Axion minicluster power spectrum and mass function*, *JCAP* **1712** (2017), no. 12 038, [1708.04466].

[11] S. Borsanyi et al., *Calculation of the Axion Mass Based on High-Temperature Lattice Quantum Chromodynamics*, *Nature* **539** (2016), no. 7627 69–71, [1606.07494].

[12] W. H. Press and P. Schechter, *Formation of Galaxies and Clusters of Galaxies by Selfsimilar Gravitational Condensation*, *Astrophys. J.* **187** (1974) 425–438.

[13] E. W. Kolb and I. I. Tkachev, *Large Amplitude Isothermal Fluctuations and High Density Dark Matter Clumps*, *Phys. Rev.* **D50** (1994) 769–773, [astro-ph/9403011].

Completion of Phase I and Preparation for Phase II of the HAYSTAC Experiment

Nicholas M. Rapidis[1]

[1]HAYSTAC Collaboration
University of California, Berkeley, Berkeley, USA

DOI: http://dx.doi.org/10.3204/DESY-PROC-2018-03/Rapidis_Nicholas

The HAYSTAC experiment utilizes a tunable resonant microwave cavity to search for dark matter axions. We report on the system and the results from Phase I of the experiment. This phase relied on a 9 T magnet, Josephson parametric amplifiers, and a dilution refrigerator for the operation of the experiment. Axion models with two photon coupling $g_{a\gamma\gamma} \gtrsim 2 \times 10^{-14}$ GeV were excluded in the $23.15 < m_a < 24.0$ μeV mass range. Phase II of the experiment will include upgrades to the cryogenics system and a new squeezed-state receiver. Finally, we discuss work on multi-rod cavities and photonic band gap resonators for higher frequency operation.

1 Introduction

Axions are a promising light dark matter candidate that also solve the Strong CP problem. They arise as the pseudogoldstone bosons that appear when a new global $U(1)_{PQ}$ symmetry is broken [1, 2, 3, 4].

To-date, most experimental efforts to search for the axion have utilized the Primakoff effect in which the axion couples to a virtual photon provided by a strong magnetic field to produce a real detectable photon. In these searches, a microwave cavity is used to resonantly enhance the signal produced by the axion. This detector setup is called a haloscope. Such cavities are tunable so that the frequency of a resonant mode of interest matches the mass of the axion, i.e. $\nu = m_a c^2/h$ $[1 + \mathcal{O}(10^{-6})]$ [5]. A schematic of this setup is shown in Figure 1.

The weak signal power of these cavities makes axion searches inherently difficult. The signal power is given by:

$$P = \left(\frac{g_\gamma^2 \alpha^2 \rho_a}{\pi^2 \Lambda^4}\right)\left(\omega_c B_0^2 V C_{nml} Q_L \frac{\beta}{1+\beta}\right)$$

where g_γ is a model-dependent coupling constant, ρ_a is the local dark matter density, set at $\rho \approx 0.45$ GeV/cm^3, and $\Lambda = 78$ GeV. The second parenthesis contains experimental parameters: ω_c is the resonant frequency of the cavity, B_0 is the applied magnetic field, V is the volume of the cavity, C_{nml} is the mode form factor, and $Q_L = Q_0/(1+\beta)$, where Q_0 is the quality factor of the mode. Cavity designs focus on increasing the values for these latter parameters.

Since the power is very weak, searches focus on increasing the signal-to-noise ratio which is

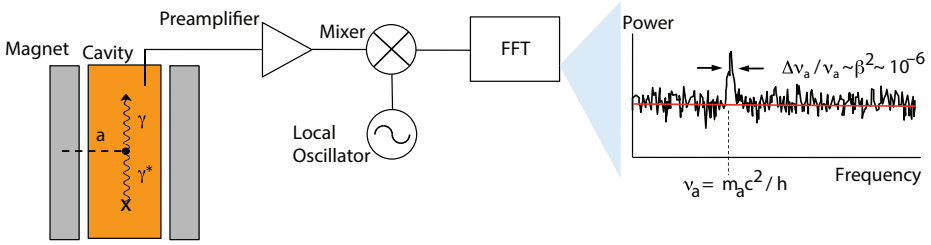

Figure 1: Schematic for haloscope with expected spectrum from axion event at ν_a with a bandwidth of $\Delta\nu_a$.

given by

$$SNR = \frac{P}{k_B T_S}\sqrt{\frac{t}{\Delta\nu_a}}$$

where T_S is the system noise temperature, $\Delta\nu_a$ is the bandwidth of the signal line, and t is the integration time. It is critical to be able to reach a low system noise temperature, which in turn is given by

$$k_B T_S = h\nu\left(\frac{1}{e^{h\nu/k_B T}-1}+\frac{1}{2}+N_A\right)$$

where N_A is the noise from the amplifier, and T is the physical temperature. As a result, when the temperature of the system is sufficiently low, the main source of noise is quantum in origin. Limiting this noise is a key component of improving axion searches.

2 HAYSTAC

The Haloscope At Yale Sensitive To Axion CDM (HAYSTAC) is a collaboration of Yale University, the University of Colorado, Boulder, and the University of California, Berkeley. The current cavity has a TM_{010} mode frequency range of $3.4-5.8$ GHz which corresponds to axions with $14\ \mu\text{eV} < m_a < 24\ \mu\text{eV}$.

2.1 Phase I

The first phase of the HAYSTAC experiment, which was completed in 2018, excluded axions with $g_{a\gamma\gamma} \gtrsim 2\times10^{-14}$ GeV in the $23.15 < m_a < 24.0\ \mu$eV range [6, 7, 8]. This is the first experiment to exclude axions in the model band at masses greater than 10 μeV. These results are summarized in Figure 2.

This phase relied on a 2 L copper-plated stainless steel cylindrical cavity of 25.4 cm in height and 10.2 cm in diameter. A 5.1 cm diameter cylindrical copper tuning rod that pivots from the center of the cavity to the wall allows for the tuning of the TM_{010} mode. This mode was chosen since its orientation along the z-axis maximized the form factor, which in turn is a measure of the overlap between the mode's electric field and the applied magnetic field. The magnetic field was provided by a 9 T magnet with a 14 cm diameter and 56 cm height bore.

The cavity was placed in a dilution refrigerator whose final plate was cooled to 127 mK. However, poor thermal contact between the rod body and the cold environment meant that

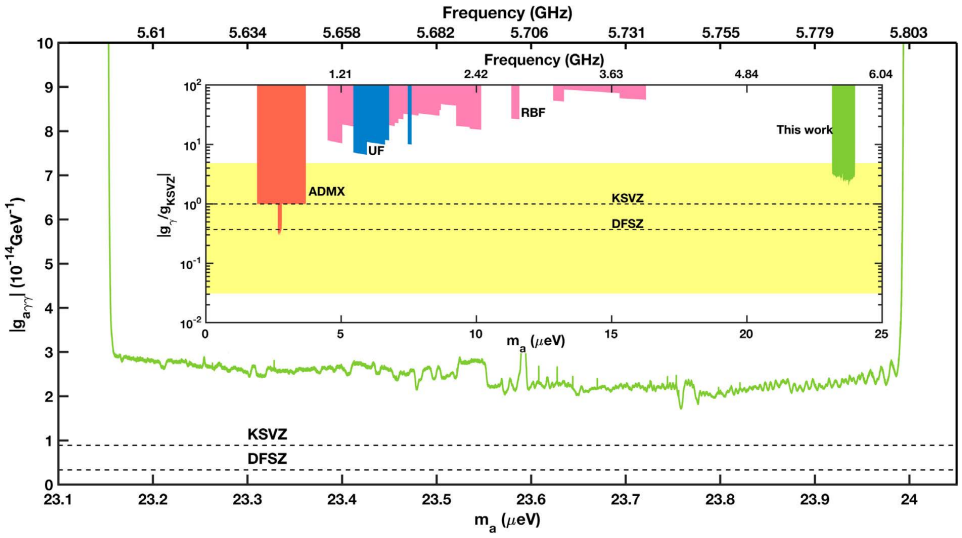

Figure 2: Exclusion limits set by Phase I of the HAYSTAC experiment in green [8].

the system was unable to cool below the standard quantum limit (SQL), which at 5 GHz corresponds to 240 mK. As a result, the first run was completed at $T \approx 3 \times T_{SQL}$ while an attempt to mitigate the problem in the second run lowered the temperature to $T \approx 2 \times T_{SQL}$. Further attempts to address this problem will be implemented in Phase II of the experiment.

A quantum limited Josephson Parametric Amplifier (JPA) was used for this phase. JPAs are nonlinear LC circuits whose inductance stems from an array of Superconducting Quantum Interference Devices (SQUIDs). The JPA provided a 20 dB gain and was tunable over 4.4-6.5 GHz.

2.2 Phase II

Preparation for Phase II of the HAYSTAC experiment will primarily focus on two upgrades: enhanced thermal properties of the system, which include a new dilution refrigerator and improved thermal contact for the rod, and the introduction of a squeezed state receiver.

A BlueFors Model LD 250 dilution refrigerator will be used for the next phase. By introducing this, the mechanical vibrations in the system will be reduced. To improve heat transfer between the tuning rod and the dilution refrigerator, two copper shafts are inserted into the two alumina alumina axles on either end of the rod. Tests at room temperature show that the copper shafts can be inserted sufficiently deep in the alumina tubes such that the thermal properties of the system are expected to significantly improve while the TM_{010} only experiences a $\sim 1 - 2\%$ drop in the quality factor.

Since the temperatures achieved by HAYSTAC are below the standard quantum limit, quantum noise becomes dominant. To address this issue, a squeezed state receiver will be used in Phase II. These devices rely on the uncertainty principle. At a given frequency the vacuum background can be written as $\mathbf{E}_\omega = \mathbf{E_0}(\hat{X}\cos(\omega t) + \hat{Y}\sin(\omega t))$ where $\hat{X}$ and $\hat{Y}$ are non-commuting observables. In the vacuum, the uncertainty can be modeled as being symmetric in phase space — this leads to the histogram in Fig. 3b where the vacuum does not have a

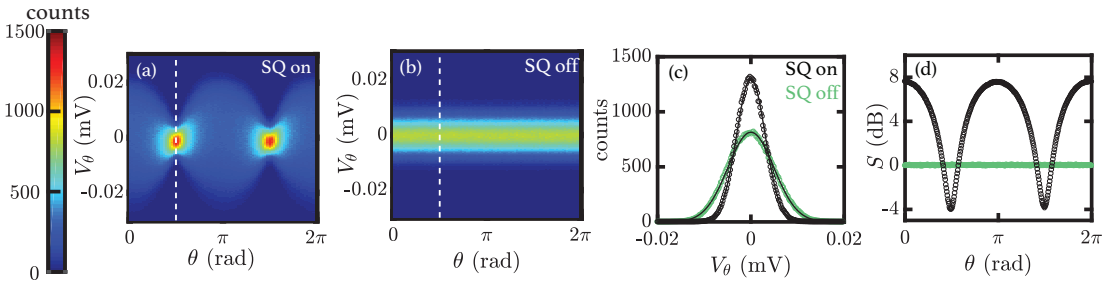

Figure 3: Histogram for output voltage fluctuations as a function of the phase difference θ between the squeezer pump and the amplifier pump (a) with squeezing and (b) without squeezing. (c) Profiles of fluctuations along the dashed line of Figs. 3a and 3b ($\theta = \pi/2$) show that squeezing provides a less ambiguous signal. (d) Ratio of square of variances $S = \sigma^2_{\text{on}}/\sigma^2_{\text{off}}$ as a function of θ for the squeezed (black) and unsqueezed (green) states [9].

preferred orientation in phase space. The squeezed state receiver can then "squeeze" the state along one quadrature (at a phase difference θ) thus reducing the uncertainty along that direction and leading to the histogram in Fig. 3a. This leads to an increase in the signal-to-noise ratio (SNR) of the system. Squeezing is only optimal when a wide range of frequencies is scanned, as in the case of haloscopes. If the exact frequency of the axion were known, a non-squeezed state would provide a higher SNR on resonance with the signal. However, by squeezing, the noise along the squeezed quadrature becomes weaker (Fig. 3c), therefore leading to shorter integration times to achieve the same SNR. This ultimately results in an increase in the scan rate of the system by a factor of 2.3.

3 Future Cavity Designs

Two new designs have been proposed for HAYSTAC's cavities: multi-rod cavities and photonic band gap structures. Multi-rod cavities act as a means of using the current cavity size and maintaining the same interaction volume while accessing higher frequencies. In particular, these cavities contain seven smaller rods: one stationary rod at the center of the cavity and six that surround the central rod. The six rods tune symmetrically outwards. This can be understood conceptually as if the seven rods act as an effective single larger rod whose radius is increasing while keeping its volume constant. Furthermore, simulations have shown that this design provides a higher form factor than that of a single larger tuning rod. This design will ultimately allow HAYSTAC to access higher frequencies in the future.

Photonic band gap (PBG) structures are also of particular interest since they can be designed to confine TM modes but not TE modes. They are similar to the current cavity but instead of a continuous wall, they contain a lattice of rods that acts as an effective wall. In the current cavity, TE modes plague regions of the frequency range since they mix with the TM modes due to the non-idealities of the cavity. When the TM_{010} mode mixes with a TE mode, its form factor degrades, thereby rendering certain frequencies unusable. By using PBG structures, previously unusable frequencies will become accessible due to the lack of mode mixing. Forthcoming publications will discuss the PBG structures and the multi-rod cavities in detail.

4 Acknowledgments

This work was supported by NSF grants PHY-1362305 and PHY-1607417, Heising-Simons Foundation grants 2014-181, 2014-182, and 2014-183, and U.S. DOE Contract DE-AC52-07NA27344. N. Rapidis is supported by the Haas Scholars Program.

References

[1] R.D. Peccei and H.R. Quinn, "CP Conservation in the Presence of Instantons," Phys. Rev. Lett. **38**, 1440 (1977) doi.org/10.1103/PhysRevLett.38.1440.

[2] R.D. Peccei and H.R. Quinn, "Constraints Imposed by CP Conservation in the Presence of Instantons," Phys. Rev. D **16**, 1791 (1977) doi.org/10.1103/PhysRevD.16.1791.

[3] S. Weinberg, "A New Light Boson?" Phys. Rev. Lett. **40**, 223 (1978) doi.org/10.1103/PhysRevLett.40.223.

[4] F. Wilczek, "Problem of Strong P and T Invariance in the Presence of Instantons," Phys. Rev. Lett. **40**, 279 (1978) doi.org/10.1103/PhysRevLett.40.279.

[5] P. Sikivie, "Experimental Tests of the 'Invisible' Axion," Phys. Rev. Lett. **51**, 1415 (1983) doi.org/10.1103/PhysRevLett.51.1415.

[6] B.M. Brubaker *et al.*, "First Results from a Micro Cavity Axion Serach at 24 μeV," Phys. Rev. Lett. **118**, 061302 (2017) doi.org/10.1103/PhysRevLett.118.061302 arXiv:1610.02580v3 [astro-ph.CO].

[7] S. Al Kenany *et al.*, "Design and Operational Experience of a Microwave Cavity Axion Detector for the $20-100$ μeV Range," Nucl. Instrum. Meth. A **854**, 11 (2017) doi.org/10.1016/j.nima.2017.02.012 [arXiv:1611.07123v2 [physics.ins-det]].

[8] L. Zhong *et al.*, "Results from Phase 1 of the HAYSTAC Microwave Cavity Axion Experiment," Phys. Rev. D **97**, 092001 (2018) doi.org/10.1103/PhysRevD.97.092001 [arXiv:1803.03690v1 [hep-exp]].

[9] M. Malnou *et al.*, "Optimal Operation of a Josephson Parametric Amplifier for Vacuum Squeezing," Phys. Rev. Applied **9**, 044023 (2018) http://doi.org/10.1103/PhysRevApplied.9.044023 [arXiv:1711.02786v1 [quant-ph]]

Status report of the QUAX R&D activity

D. Alesini[1], *C. Braggio*[2,3], *G. Carugno*[2,3], *N. Crescini*[3,4], *D. Di Gioacchino*[1], *P. Falferi*[5,6], *S. Gallo*[2,3], *U. Gambardella*[8], *C. Gatti*[1], *G. Iannone*[8], *G. Lamanna*[9], *C. Ligi*[1], *A. Lombardi*[4], *R. Mezzena*[6,7], *A. Ortolan*[4], *S. Pagano*[8], *R. Pengo*[4], *A. Rettaroli*[1], *G. Ruoso*[4], *C. C. Speake*[10], *L. Taffarello*[2], *S. Tocci*[1]

[1]INFN, Laboratori Nazionali di Frascati, Frascati (Roma), Italy
[2]INFN, Sezione di Padova, Padova, Italy
[3]Dip. di Fisica e Astronomia, Padova, Italy
[4]INFN, Laboratori Nazionali di Legnaro, Legnaro (PD), Italy
[5]Istituto di Fotonica e Nanotecnologie, CNR-Fondazione Bruno Kessler, Povo (TN), Italy
[6]INFN, TIFPA, Povo (TN), Italy
[7]Dip. di Fisica, Povo (TN), Italy
[8]Dip. di Fisica E.R. Caianiello, Fisciano (SA), Italy and INFN, Sez. di Napoli, Napoli, Italy
[9]Dip. di Fisica and INFN, Sez. di Pisa, Pisa, Italy
[10]School of Physics and Astronomy, Univ. of Birmingham, Birmingham, United Kingdom

DOI: http://dx.doi.org/10.3204/DESY-PROC-2018-03/Ruoso_Giuseppe

The current status of the QUAX R&D program is presented. QUAX is a feasibility study for a detection of axion as dark matter based on the coupling to the electrons. The relevant signal is a magnetization change of a magnetic material placed inside a resonant microwave cavity and polarized with a static magnetic field.

1 Introduction

The QUAX (QUaerere AXion) program explores the feasibility of an apparatus to detect axions as a dark matter component by exploiting its interaction with the spin of electrons (See [1] and references therein). Due to the motion of the Solar System through the galactic halo, the Earth is effectively moving through the cold dark matter cloud surrounding the Galaxy and an observer on Earth could detect such axion wind. In particular, its effect on a magnetized material can be described as an effective oscillating rf field with frequency determined by the axion mass m_a and amplitude proportional to the axion-electron coupling constant g_{aee} and to the dark matter density and velocity. Thus, a possible detector for the axion wind can be a magnetized sample with Larmor resonance frequency tuned to the axion mass by means of an external polarizing static magnetic field: e.g. 1.7 T for 48 GHz, corresponding to $m_a \simeq 200\,\mu$eV, in the case of the interaction with the electron spin that is considered here. The interaction with the axion effective field drives the total magnetization of the sample, and so produce oscillations in the magnetization that, in principle, can be detected. To optimize the detection scheme, the sample is placed inside a microwave cavity. The cavity and the magnetized sample have to be cooled down at ultra-cryogenic temperature to reduce the noise due to thermal photons.

2 The QUAX prototype

The QUAX apparatus [2] uses a cylindrical copper cavity TM110 mode with resonance frequency $f_c \simeq 13.98\,\text{GHz}$ and linewidth $k_c/2\pi \simeq 400\,\text{kHz}$ at liquid helium temperature. The shape of the cavity is not a regular cylinder, two symmetric sockets are carved into the cylinder to remove the angular degeneration of the normal mode, the maximum and minimum diameters are 26.7 mm and 26.1 mm, and the length is 50.0 mm. The choice of the TM110 mode has the advantage of having a uniform maximum magnetic rf field along the cavity axis. Its volume can be increased using a longer cavity without changing the mode resonance frequency. The cavity mode is coupled to a magnetic material. Highest values of spin density n_s together with long relaxation times have been found for YIG (Yttrium Iron Garnet) and GaYIG (Gallium doped YIG). To avoid inhomogeneous broadening of the linewidth due to geometrical demagnetization, these garnets are shaped as highly polished spheres. Five GaYIG spheres of 1 mm diameter have been placed in the maximum magnetic field of the mode, which lies on the axis of the cavity. The spheres are housed inside a PTFE support large enough to let them rotate in all possible directions, in order to automatically align the GaYIG magnetization easy axis with the external magnetic field.

The amplitude of an external magnetic field B_0 determines the Larmor frequency f_L of the electrons. The uniformity of B_0 on all the spheres must be enough to avoid inhomogeneous broadening of the ferromagnetic resonance. To achieve a magnetic field uniformity $\leq 1/Q_h$, where $Q_h \sim 10^4$ is the quality factor of the hybrid mode, we make use of a superconducting NbTi cylindrical magnet equipped with a concentric cylindrical NbTi correction magnet. With $B_0 = 0.5\,\text{T}$ we have $f_L \simeq f_c$ and thus the hybridization of the cavity and Kittel modes. The power supply of the main magnet is a high-precision, high-stability current generator, injecting 15.416 A into the magnet with a precision better than 1 mA, while a stable current generator provides 26.0 A for the correction magnet. A simplified scheme of the cavity, material and magnet setup is represented in the left part of Fig. 1.

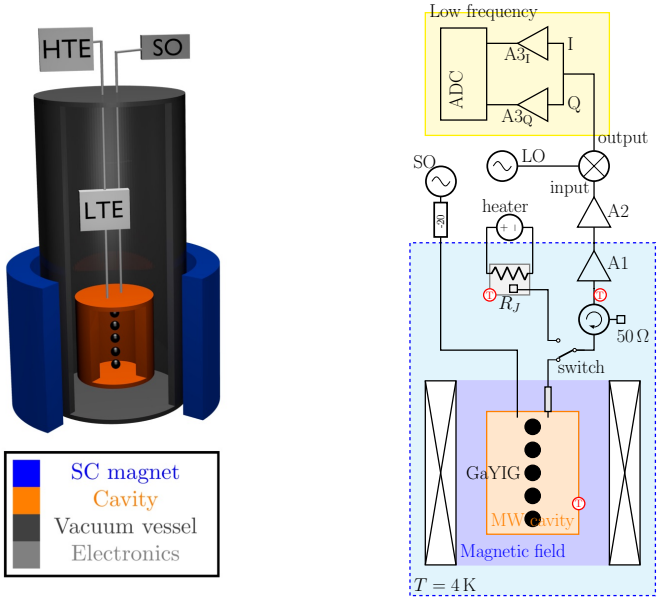

Figure 1: *Left* - Simplified scheme (not to scale) of the experimental apparatus showing the high temperature and low temperature electronics (HTE and LTE) and the source oscillator (SO). *Right* - Electronics layout.

The detection electronics consists in an amplification chain which has two inputs, called Input Channel 1 and 2, (IC-1 and IC-2, respectively). Channel 1 measures the signal power, while Channel 2 has calibration and characterization purposes. A cryogenic switch is used to select the desired channel:

IC-1 - The rf power inside the cavity is collected with a dipole antenna whose coupling to the cavity can be changed using an external micro-manipulator, allowing us to switch continuously from sub-critical to over-critical coupling. For optimal measurement conditions, we tune the antenna to critical coupling by doubling the sub-critical linewidth of the selected mode;

IC-2 - A 50 Ω termination R_J, enclosed in a copper block together with a heater resistance, is used as Johnson noise source. The emitted power can be used to calibrate the noise temperature of the system and the total gain.

3 Results

The output of the cavity is down-converted in its in-phase and quadrature components with respect to the local oscillator (LO), that are sampled separately. We applied a complex FFT to $\{s_n\} = \{\phi_n\} + i\{q_n\}$ to get its power spectrum s^2_ω with positive frequencies for $f > f_{\rm LO}$ and negative frequencies for $f < f_{\rm LO}$.

Fig. 2 reports the analysis of RUN31, which we describe hereafter in some details. The ∼2.3 hours of the measurement consist in 2048000 FFTs of 8192 bins each (frequency resolution of 244 Hz), which were square averaged and rebinned to the bandwidth $\Delta f = 7.8\,$kHz (256 bins), close to the axion linewidth. Some frequency intervals of the power spectrum were affected by disturbances at the ADC output, and has been ignored in the analysis procedure. A polynomial of degree 5 is fitted to the averaged spectrum and the residuals estimated. The averaged spectrum is reported in Fig. 2 together with the fitting function.

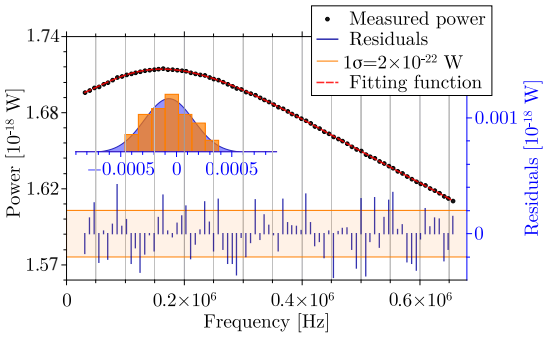

Figure 2: Down-converted power spectrum and residuals of RUN31. The black dots are the measured data points and their error is within the symbol dimensions, the red line is a polynomial fit of such points. The residuals are represented in blue and, as an inset, we show them on an histogram. The corrupted intervals are removed.

In Fig. 2 a plot of the residuals and their histogram is also given. The average value of the residuals is $-4.6 \times 10^{-23}\,$W with standard deviation $\sigma_P = 2.2 \times 10^{-22}\,$W. The result is compatible with Dicke radiometer equation

$$\sigma_{\rm D} = k_B(T_c + T_n)\sqrt{\frac{\Delta f}{t}} = 2.1 \times 10^{-22}\sqrt{\left(\frac{\Delta f}{7.8\,\text{kHz}}\right)\left(\frac{8280\,\text{s}}{t}\right)}\,\text{W}, \tag{1}$$

where t is the total integration time, T_n system noise temperature and T_c cavity temperature. This means that the standard deviation of the noise decreases as $1/\sqrt{t}$ trend at least within the RUN31 time span.

The measured rf power is compatible with the modeled noise for every bin and no statistically significant signal consistent with axions was found. The upper limit at the 95% C.L. is $2\sigma'_P = 1.1 \times 10^{-21}\,$W. This value can be converted to an equivalent axion field [2], obtaining

$$B_m < 2.6 \times 10^{-17}\left[\left(\frac{14\,\text{GHz}}{f_+}\right) \times \left(\frac{2.13 \cdot 10^{28}/\text{m}^3}{n_S}\right)\left(\frac{0.11\,\mu\text{s}}{\tau_+}\right)\left(\frac{2.6\,\text{mm}^3}{V_s}\right)\right]^{1/2}\text{T}, \tag{2}$$

where f_+, τ_+ are the working mode frequency and relaxation time, V_s the GaYIG volume: all the reported parameters have been explicitly measured. Several measurements have been performed for different cool downs of the setup. Probably due to mechanical instabilities and to the low resolution of the correction magnet power supply, the resulting working frequency f_+ slightly changed between the runs, allowing us to perform also a limited frequency scan over a $\sim$3 MHz range. The maximum integration time for a 1 MHz band was 6 hours, and no deviations from the $1/\sqrt{t}$ scaling of σ_P were found.

Our results represent also a limit on the axion-electron coupling constant, since the relation between B_m and g_{aee} is known once the axion dark matter density is fixed. The results of this preliminary measurements are far from the sensitivity requirements for a cosmological axion search, however they can be used to detect DM Axion-like particles (ALPs). During the measurement time the DM-wind amplitude was on the maximum of the daily modulation, allowing us to use the collected data to obtain an upper limit on the ALP-electron coupling at the maximum sensitivity. By repeating the analysis procedure for seven measurement runs and averaging together overlapping bandwidths, we produce the plot in Fig. 3. The minimum measured value of g_{aee} is 4.9×10^{-10}, corresponding to an equivalent axion field limit of 1.6×10^{-17} T.

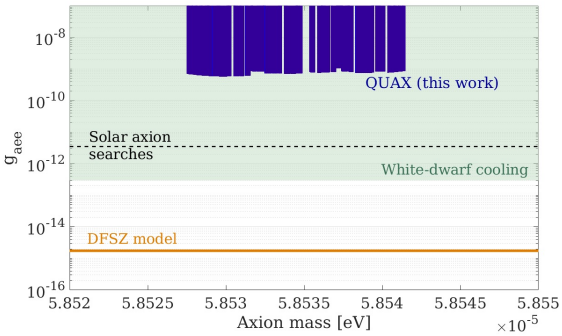

Figure 3: Excluded values of the g_{aee} coupling (blue area) compared to its theoretical prediction for the DFSZ axion model (orange line) and a DM density of 0.45 GeV/cm^3. The green shaded area is excluded by white dwarf cooling, while the black dashed line is the best upper limit obtained with solar axion searches relying on the axio-electric effect (See ref. [2] for details).

Acknowledgments

The authors wish to thank Fulvio Calaon, Mario Tessaro, Mario Zago, Massimo Rebeschini, Andrea Benato and Enrico Berto for the help with cryogenics and for the mechanical and electronic work on the experimental setup. We acknowledge the support of Giampaolo Galet and Lorenzo Castellani for the building of the high-precision power supply and Nicola Toniolo, Michele Gulmini and Stefano Marchini for the work on the DAQ system. We also acknowledge Riccardo Barbieri for the stimulating theoretical discussions.

References

[1] R. Barbieri *et al.*, Phys. Dark Univ. **15**, 135 (2017).

[2] N. Crescini *et al.*, Eur. Phys. J. C **78**, 703 (2018).

Standard Model thermodynamics and primordial gravitational waves

Ken'ichi Saikawa[1], *Satoshi Shirai*[2]

[1]Max-Planck-Institute for Physics, Munich, Germany
[2]Kavli Institute for the Physics and Mathematics of the Universe (Kavli IPMU), Chiba, Japan

DOI: http://dx.doi.org/10.3204/DESY-PROC-2018-03/Saikawa_Kenichi

We discuss the role of Standard Model thermodynamics in cosmology and identify how it affects the spectrum of primordial gravitational waves. By collecting recent results of perturbative and non-perturbative analysis of thermodynamic quantities in the Standard Model, we obtain the effective degrees of freedom including the corrections due to non-trivial interaction properties of particles for a wide temperature interval. Applying them to the estimation of the spectrum of gravitational waves originated from inflation, we find that there exist several corrections overlooked in previous studies, and that some of them are relevant to future high-sensitivity gravitational wave experiments.

1 Introduction

The existence of primordial gravitational waves (GWs) is an important prediction of inflationary theory. In order to extract detailed information about the primordial universe from future observations, it will become more important to improve the precision of theoretical calculations. The purpose of this work is to obtain the state-of-the-art results for thermodynamic quantities in the Standard Model (SM), or the effective degrees of freedom,

$$g_{*\rho}(T) = \frac{\rho(T)}{\left[\frac{\pi^2 T^4}{30}\right]}, \quad g_{*s}(T) = \frac{s(T)}{\left[\frac{2\pi^2 T^3}{45}\right]}, \tag{1}$$

where $\rho(T)$ and $s(T)$ are the energy density and entropy density of the primordial plasma at temperature T, and apply them to the analysis of the primordial GWs. Usually, the above effective degrees of freedom are estimated by assuming that the SM plasma behaves like an ideal gas. However, this assumption does not always hold true. There exist corrections due to particle interactions, which have to be quantitatively taken into account.

2 Inflationary gravitational waves

The GW background is originated from the quantum fluctuations generated during inflation. The spectrum of GWs at the present (conformal) time $\tau = \tau_0$ can be described as

$$\Omega_{\rm gw}(k) \equiv \frac{1}{\rho_{\rm crit}} \frac{d\rho_{\rm gw}(k)}{d\ln k} = T(k)\mathcal{P}_T(k), \quad T(k) \equiv \frac{1}{12 a_0^2 H_0^2} \left[\frac{d\chi(k,\tau_0)}{d\tau}\right]^2, \tag{2}$$

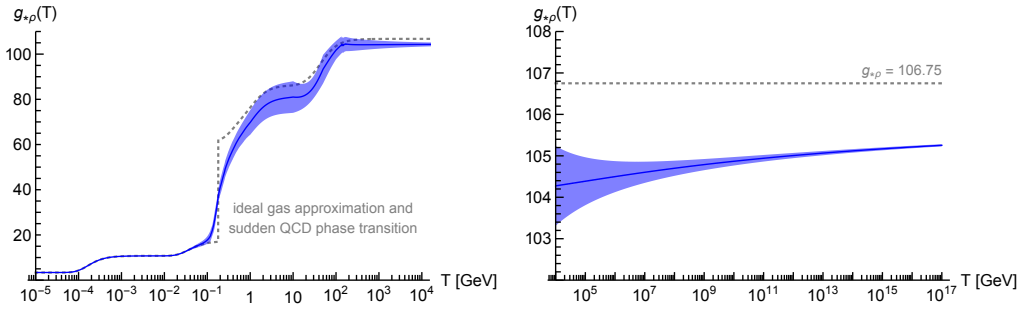

Figure 1: Temperature dependence of the effective degrees of freedom for the energy density in the SM [4].

where $\rho_{\rm gw}$ and $\rho_{\rm crit}$ are the energy density of GWs and the critical energy density of the universe, respectively, k is the comoving wavenumber, a_0 and H_0 are the scale factor and Hubble parameter at the present time, respectively, $\mathcal{P}_T(k) = (2H^2)/(\pi^2 M_{\rm Pl}^2)|_{k=aH}$ represents the primordial tensor power spectrum, which is determined by the Hubble parameter H when the mode with a wavenumber k crosses the horizon during inflation, and $M_{\rm Pl}$ is the reduced Planck mass. The transfer function $T(k)$ can be evaluated by solving the late-time evolution of the tensor perturbation $\chi(k,\tau)$ [1]:

$$\chi''(u) + \left[\frac{2a'(u)}{a}\right]\chi'(u) + \chi(u) = -\sum_{i=\gamma,\nu}\frac{\rho_i(u)}{\rho_{\rm crit}(u)}\left[\frac{a'(u)}{a(u)}\right]^2\int_{u_{i\,\rm dec}}^{u} dU\left[\frac{j_2(u-U)}{(u-U)^2}\right]\chi'(U), \quad (3)$$

where $u = k\tau$ and derivatives are taken with respect to u. The right-hand side corresponds to the contribution of free-streaming photons ($i = \gamma$) and neutrinos ($i = \nu$) to the anisotropic stress, and $\tau_{i\,\rm dec}$ represents the time at which they decouple from the thermal bath.

If we use the WKB approximation for $\chi(k,\tau)$ and assume that the mode reenters the horizon during the radiation dominated era, we further obtain the following approximate formula:

$$\Omega_{\rm gw}(k)h^2 \approx 5.15\times10^{-7}\, g_{*\rho}(T_{\rm hc})\left(\frac{g_{*s}(T_{\rm hc})}{g_{*s}(T_0)}\right)^{-\frac{4}{3}}\mathcal{P}_T(k), \quad (4)$$

where $T_{\rm hc}$ is temperature at the horizon crossing. Aside from the k-dependence of $\mathcal{P}_T(k)$, a non-trivial change of $g_{*\rho}(T)$ and $g_{*s}(T)$ can affect the detailed shape of the spectrum.

3 Equation of state in the Standard Model

To evaluate $g_{*\rho}(T)$ and $g_{*s}(T)$, we need to compute the energy density $\rho(T)$ and the entropy density $s(T)$, which are given by the pressure $p(T)$ and its derivative with respect to T. The pressure can be evaluated by considering a partition function:

$$p(T) = \frac{T}{V}\ln\mathcal{Z}, \quad \mathcal{Z} = \int\mathcal{D}\varphi\ldots\exp\left(-\int_0^{1/T}\int d^3x\mathcal{L}\right), \quad (5)$$

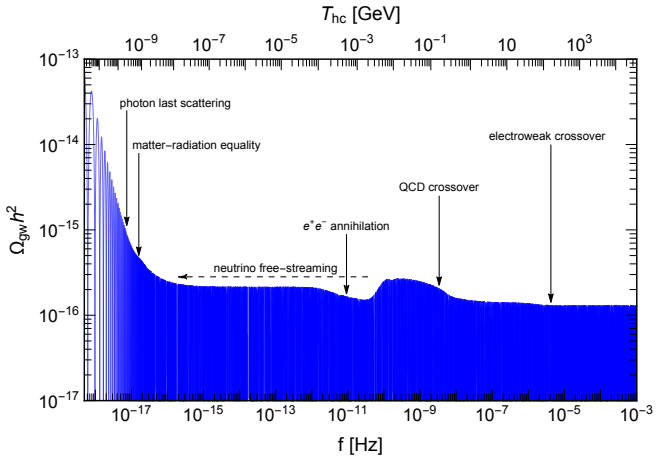

Figure 2: The spectrum of inflationary GWs for a broad frequency interval [4].

where V is a volume and $\mathcal{L}$ is the Lagrangian density of the theory. In the literature, there has been a lot of progress on the calculation of $p(T)$ in the SM with both perturbative and non-perturbative methods [see e.g. Refs. [2, 3]]. We collect all the results and combine them to estimate $g_{*\rho}(T)$, $g_{*s}(T)$, and their uncertainty at arbitrary temperatures, and the results are shown in Fig. 1. The dominant source of uncertainty in thermodynamic quantities in the SM is the estimation of the pressure of QCD at $T = \mathcal{O}(1\text{–}10)\,\mathrm{GeV}$. We quantify the corresponding uncertainty by interpolating the results obtained by different methods at that temperature range. We also note that there is some deviation from the ideal gas result and the convergence to the commonly used value 106.75 is fairly slow even at very high temperatures.

4 Spectrum of gravitational waves

We estimate the spectrum of GWs by numerically solving Eq. (3) together with the Friedmann equation for the scale factor $a(t)$, and Fig. 2 shows the result for a broad frequency interval. Note that the frequency of GWs can be related to the temperature $T_{\rm hc}$ at which the corresponding mode reenters the horizon. We find that there exist several corrections on the spectrum of GWs due to the effects that were overlooked in previous studies. The revision of the efficiency of the collisionless damping effect due to free-streaming photons and neutrinos results in additional suppression of the amplitudes of GWs at the frequency $f \sim 10^{-17}\,\mathrm{Hz}$ and $f \sim 10^{-11}\,\mathrm{Hz}$, respectively. We also find that the amplitude of GWs at $f \sim 10^{-8}\,\mathrm{Hz}$ changes smoothly due to the crossover nature of the QCD phase transition, which is in contrast to that of previous analysis [1] that there exists a wiggly feature due to the assumption that the values of $g_{*\rho}$ and g_{*s} change almost discontinuously at the critical temperature of the QCD phase transition. See Ref. [4] for details.

We note that the correction to the effective degrees of freedom due to the particle interactions in the SM can have an actual impact on experimental studies. In Fig. 3, we show the spectrum of GWs at higher frequencies. It turns out that the amplitude of GWs becomes slightly larger

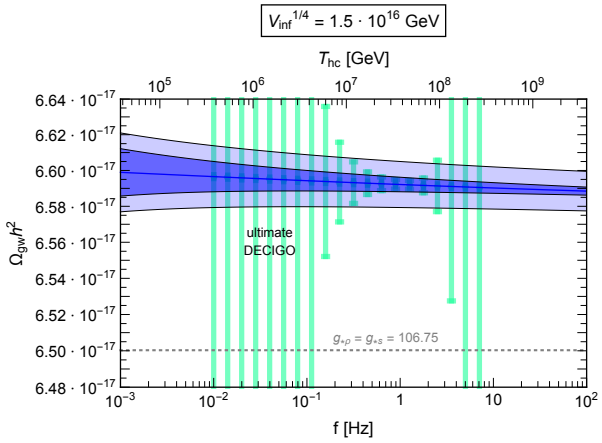

Figure 3: The spectrum of inflationary GWs at a higher frequency range and sensitivity of ultimate DECIGO [4]. For simplicity, here we assume that the primordial tensor power spectrum is a k-independent constant, $\mathcal{P}_T(k) = (2V_{\rm inf})/(3\pi^2 M_{\rm Pl}^4)$, with a fixed value of the inflationary energy scale $V_{\rm inf}^{1/4} = 1.5 \times 10^{16}\,{\rm GeV}$.

than the conventional estimate based on $g_{*\rho} = g_{*s} = 106.75$ due to the fact that $\Omega_{\rm gw}$ is approximately proportional to $g_{*\rho}(T_{\rm hc})^{-1/3}$ [see Eq. (4)] and that the values of the effective degrees of freedom remain smaller than the commonly assumed value 106.75 even at high temperatures. In principle, such a correction can be observed by future high-sensitivity GW experiments such as ultimate DECIGO [5].

5 Conclusion

In this work, we have estimated the temperature evolution of the effective degrees of freedom and their uncertainty for a wide temperature interval by including the effect of particle interactions in the SM. The refined results for the effective degrees of freedom lead to several corrections on the spectrum of inflationary GWs that were overlooked in previous studies. In particular, the amplitude of GWs at high frequencies becomes $\gtrsim 1\,\%$ larger than previous estimates, which is relevant to future high-sensitivity experiments. Although we have focused on the spectrum of primordial GWs in this work, we note that there would be a potential application of the effective degrees of freedom in the SM to several other topics in cosmology such as the analysis of the relic dark matter abundance.

References

[1] Y. Watanabe and E. Komatsu, Phys. Rev. D **73**, 123515 (2006) [astro-ph/0604176].

[2] M. Laine and M. Meyer, JCAP **1507**, no. 07, 035 (2015) [arXiv:1503.04935 [hep-ph]].

[3] S. Borsanyi *et al.*, Nature **539**, no. 7627, 69 (2016) [arXiv:1606.07494 [hep-lat]].

[4] K. Saikawa and S. Shirai, JCAP **1805**, no. 05, 035 (2018) [arXiv:1803.01038 [hep-ph]].

[5] N. Seto, S. Kawamura and T. Nakamura, Phys. Rev. Lett. **87**, 221103 (2001) [astro-ph/0108011].

Simulation studies for the MADMAX axion direct detection experiment

Jan Schütte-Engel[1] *on behalf of the MADMAX collaboration*

[1]University of Hamburg, Hamburg, Germany

DOI: http://dx.doi.org/10.3204/DESY-PROC-2018-03/Schuette-Engel_Jan

We present a general approach to solve the Maxwell-axion equations for arbitrary geometries and materials. The approach is based on the finite element method (FEM) and applied to experimental setups related to the new MADMAX (MAgnetized Disc and Mirror Axion eXperiment) project. Analytical methods are used to verify the FEM simulations. MADMAX is a dielectric haloscope which will utilize axion-photon conversion at many dielectric interfaces and probe axions in the mass range $m_a = 40 - 400$ μeV.

1 Introduction

The axion [1–3] is well motivated because it solves the strong CP problem and is at the same time a dark matter candidate. MADMAX is an experiment designed to detect axions from the dark matter halo by exploiting the effect of axion-photon mixing [4, 5]. Axion-electrodynamics yields two E-field solutions [6, 7] when a strong B-field is applied over an interface between two materials of different refractive index, because the fields have to satisfy interface conditions. The *photon-like* E-field is propagating away from the interface, while the *axion-like* E-field is a non-propagating solution[1]. MADMAX will resonantly enhance the propagating waves by using many dielectric discs. An idealized 1-dimensional calculation for the E-field boost which MADMAX can produce already exists [7, 8]. Here we present first results towards a simulation which takes into account diffraction losses and near-field effects which appear at discs of finite size.

The following text is structured as follows: In Sec. 2 the Maxwell-axion equations are introduced. After that we solve them for three different setups which are related to MADMAX. In Sec. 3 the photon-like E-fields coming from a circular perfectly electrically conducting (PEC) surface are computed. Furthermore two analytical approaches are cross checked against the 3-dimensional finite element method (FEM) simulations. In Sec. 4 the E-fields coming from a single dielectric disc in a strong external B-field are shown. The axion-electrodynamics solution for a waveguide, which is half filled with a dielectric, is computed in Sec. 5.

[1]Under the assumption that the B-field varies only slowly on the scale of the photon-like wavelength and the axions are non relativistic.

2 Maxwell-axion equations

The Maxwell-axion equations [5] are a coupled system of partial differential equations (PDEs). To decouple the Klein-Gordon equation from the modified Maxwell equations we generalize the perturbation approach [9] and expand all fields in $g_{a\gamma}$: $X(\boldsymbol{x},t) = X^{(0)}(\boldsymbol{x},t) + \sum_{i=1}^{\infty} g_{a\gamma}^i m_a^i X^{(i)}(\boldsymbol{x},t)$, with $X = \boldsymbol{E}, \boldsymbol{B}, \boldsymbol{J}_f, a, \rho_f$[2]. In the following we will only focus on the first order equations:

$$\nabla \cdot \boldsymbol{D}^{(1)} = \rho_f^{(1)} + \rho_a^{(1)}, \tag{1}$$

$$\nabla \times \boldsymbol{H}^{(1)} - \partial_t \boldsymbol{D}^{(1)} = \boldsymbol{J}_f^{(1)} + \boldsymbol{J}_a^{(1)}, \tag{2}$$

$$(\partial_\mu \partial^\mu + m_a^2) a^{(1)} = \frac{1}{m_a} \boldsymbol{E}^{(0)} \cdot \boldsymbol{B}^{(0)}, \tag{3}$$

with the axionic charge density $\rho_a^{(1)} = -\frac{1}{m_a} \boldsymbol{B}^{(0)} \cdot \nabla a^{(0)}$ and current density $\boldsymbol{J}_a^{(1)} = \frac{1}{m_a}(\boldsymbol{B}^{(0)} \partial_t a^{(0)} - \boldsymbol{E}^{(0)} \times \nabla a^{(0)})$. In this work we assume linear constitutive relations and no material losses $\boldsymbol{D}(\boldsymbol{x},t) = \epsilon(\boldsymbol{x}) \boldsymbol{E}(\boldsymbol{x},t)$, $\boldsymbol{H}(\boldsymbol{x},t) = \boldsymbol{B}(\boldsymbol{x},t)$, $\boldsymbol{J}_f^{(1)} = 0$. Furthermore, we assume the *zero velocity* limit $a^{(0)}(\boldsymbol{x},t) = a^{(0)}(t) = a_0 e^{-i\omega t}$, i.e. axions are at rest and that we have only an external B-field (i.e. $\boldsymbol{E}^{(0)} = 0$). The corresponding PDE we solve is therefore

$$\nabla \times (\mu^{-1} \nabla \times \boldsymbol{E}) - m_a^2 \epsilon \boldsymbol{E} - m_a \boldsymbol{B}^{(0)} a^{(0)} = 0, \tag{4}$$

with $\omega = m_a$, the permittivity ϵ and harmonic time dependence for the E-field. In Eq. (4) and in all following studies the superscript (1) is omitted. We use the tools COMSOL [10] and ELMER [11] to solve Eq. (4).

3 Perfectly electrically conducting surface

In this section diffraction and near-field effects of the photon-like E-field from a circular PEC are investigated. The external B-field is assumed to be homogeneous over the PEC $\boldsymbol{B}^{(0)} = B^{(0)} \hat{\boldsymbol{e}}_y$ as shown in Fig. 1. On the basis of a Fourier transformation [12] we derive the following formula for the propagating E-field:

$$\frac{E_y(r,z,t)}{E_0} = e^{-i\omega t} \int d\tilde{\rho} e^{i\sqrt{\tilde{\omega}^2 - \tilde{\rho}^2}\tilde{z}} J_0(\tilde{r}\tilde{\rho}) J_1(\tilde{\rho}), \quad \text{with} \quad \tilde{\rho} = \rho R, \tilde{r} = \frac{r}{R}, \tilde{z} = \frac{z}{R}, \tilde{\omega} = \omega R, \tag{5}$$

where J_0 and J_1 are Bessel functions of the first kind and E_0 is the magnitude of the photon-like E-field at the PEC. To study diffraction effects we define an imaginary receiver surface at a variable distance away from the emitter surface. On the receiver surface we define the variable $\bar{U}$ as the ratio of received power over emitted power. Figure 2 shows $\bar{U}$ for many frequencies and we find that for lower frequencies the diffraction loss is larger. A similar study for different PEC radii and a fixed frequency shows that the diffraction loss for smaller disc radii is larger. A more advanced description of the diffraction, which includes near-field effects, can be obtained by the Kirchhoff[3] formula [13]. In Fig. 3 the Kirchhoff results are compared to the FEM results in the xy-plane 10 cm away from the PEC ($R = 6\,\text{cm} = 2\lambda$). The overall good agreement gives us an encouraging validation of our FEM simulations.

[2] $\boldsymbol{E}$ and $\boldsymbol{B}$ are the E and B-fields, $\boldsymbol{J}_f$ and ρ_f are the free charge and current density and a is the axion field.

[3] The vector Kirchhoff formula is still not a complete description of the photon-like E-field, because it does not take into account boundary charges.

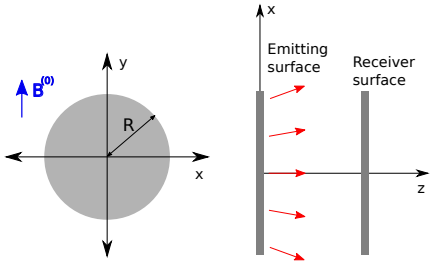

Figure 1: PEC surface in the xy and zx-plane.

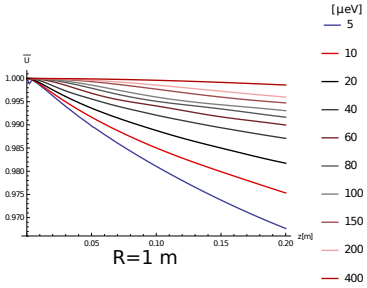

Figure 2: Emitted power over received power for different axion masses.

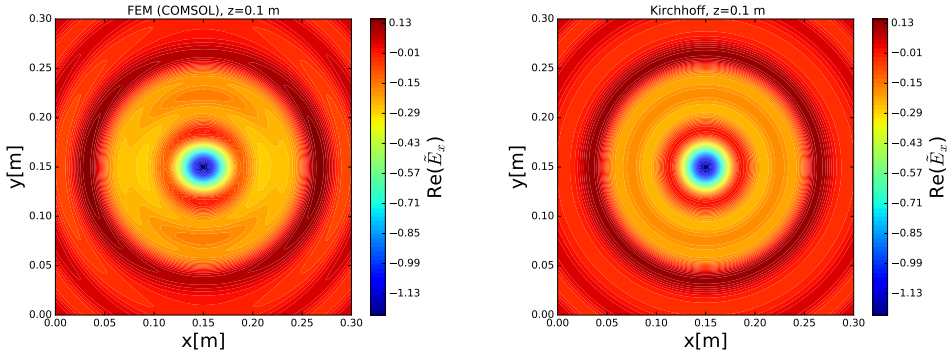

Figure 3: FEM (left) and the Kirchhoff (right) results for a PEC. The tilde symbolizes that the E-field values are normalized to the E-field which is emitted by an infinite PEC surface.

4 Dielectric disc

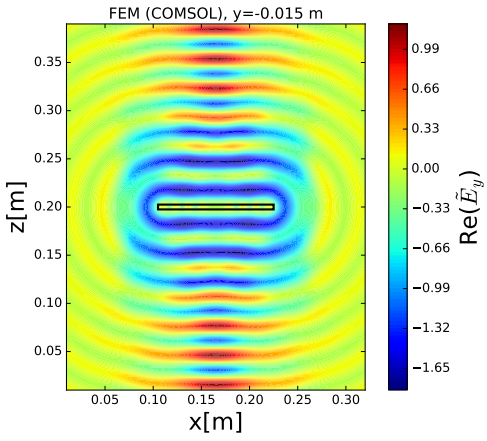

Figure 4: Radiating dielectric disc.

Besides a mirror the MADMAX experiment consists of many dielectric discs. In this section Eq. (4) is solved with the FEM for one circular dielectric disc of radius $R = 6\,\text{cm}$, thickness $0.5\,\text{cm}$ and $\epsilon = 9$ at a wavelength of $\lambda = 3\,\text{cm}$ (resonant case). The coordinate system is chosen as in the PEC case, just replacing the PEC with the dielectric disc (see Fig. 1). The B-field is constant over the complete disc and drops off to the boundaries of the simulation domain. Figure 4 shows a cross-section of the simulation domain where the disc is located at $z = 0.2\,\text{m}$. Close to the disc near-field effects are seen while far away from the disc classical diffraction effects are observed. The E-field in Fig. 4 was normalized as in the PEC case.

5 Waveguide filled with dielectrics

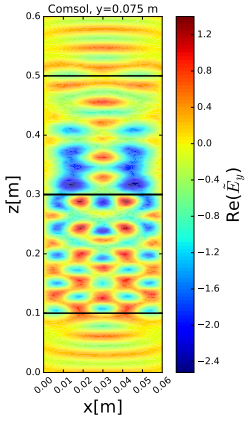

Figure 5: E-field solution for a waveguide half filled with dielectric material.

As a final example we show the simulation of a rectangular waveguide which has dimensions $2\lambda \times 5\lambda \times 20\lambda$, with $\lambda = 3\,\mathrm{cm}$ (see Fig. 5). The lower part of the waveguide ($0.1\,\mathrm{m} < z < 0.3\,\mathrm{m}$) is filled with a dielectric ($\epsilon = 2$), while the upper part of the waveguide is empty ($0.3\,\mathrm{m} < z < 0.5\,\mathrm{m}$). The ranges ($z < 0.1\,\mathrm{m}$ and $z > 0.5\,\mathrm{m}$) are free space simulation domains. We apply an external B-field which drops off in z-direction with a $\cos^2$ behavior to the ends of the waveguide. Inside the waveguide only specific modes are propagating which make the transition to the outside when reaching the ends of the waveguide. The tilde on the E-field in Fig. 5 symbolizes the same normalization as in the previous Secs.

6 Conclusions and outlook

We performed the first FEM simulations for MADMAX related setups. The simulations are compared to analytical calculations to validate the FEM simulations and for a better understanding of the diffraction and near-field effects, which are possible loss mechanisms in the MADMAX experiment. Our studies motivate us to investigate further loss mechanisms and to study more complicated experimental configurations, e.g. setups with more dielectric discs.

References

[1] R.D. Peccei, H.R. Quinn, Phys. Rev. Lett., **38**, 1440 (1977)

[2] S. Weinberg, Phys. Rev. Lett., **40**, 223 (1978)

[3] F. Wilczek, Phys. Rev. Lett., **40**, 279 (1978)

[4] G. Raffelt and L.Stodolsky, Phys. Rev. D, **37**, 1237 (1988)

[5] P. Sikivie, Phys. Rev. Lett., **51**, 1415 (1983)

[6] D. Horns *et al.*, JCAP, **1304**, 016 (2013) [arXiv:1212.2970[hep-ph]]

[7] A. Millar *et al.*, JCAP **1701**, 061 (2017) [arXiv:1612.07057 [hep-ph]]

[8] A. Millar *et al.*, JCAP **1710**, 006 (2017), erratum JCAP 1805 (2018), no.05, E02 [arXiv:1707.04266 [hep-ph]]

[9] P. Hoang *et al.*, Physics of the dark universe, (2017) http://dx.doi.org/10.1016/j.dark.2017.04.004

[10] COMSOL Multiphysics® v. 5.3. www.comsol.com. COMSOL AB, Stockholm, Sweden.

[11] Elmer finite element solver for multiphysical problems. URL www.csc.fi/web/elmer/elmer

[12] Joseph W. Goodman: Introduction to Fourier optics. 3rd ed.

[13] J.D. Jackson, "Classical electrodynamics," Wiley, 3rd ed., (1999)

ALPS II Status Report

Aaron Spector[1] *for the ALPS collaboration*

[1]DESY, Hamburg, Germany

DOI: http://dx.doi.org/10.3204/DESY-PROC-2018-03/Spector_Aaron

ALPS II is a light shining through a wall style experiment that will use optical cavities to resonantly enhance the coupling between photons and axion-like particles in the mass range below 0.1 meV. In the last year there has been significant experimental progress in the development of the optical system and the single photon detection schemes, as well as progress related to the preparation of the magnets and the on site infrastructure.

1 Introduction

The Any Light Particle Search II (ALPS II) [1] is a light shining through a wall (LSW) style of experiment under construction at DESY in Hamburg, Germany. ALPS II will search for a broad class of low mass, weakly interacting, 'axion-like' particles, that can mix with photons in presence of a strong magnetic field. The axion, the namesake for the axion-like particles, is a firm prediction [2, 3] of a solution to the strong CP problem in QCD proposed in 1977 by Peccei and Quinn [4].

LSW experiments are designed to measure the coupling between two photons and axion-like particles, $g_{a\gamma}$, in a laboratory setting [5]. This is done by shining a high power laser through a strong magnetic field thus generating a beam of axion-like particles that propagates through a wall that blocks the light. After the wall there is a second magnetic field that reconverts some of the axion-like particles to photons which are measured with a single photon detection scheme. Since LSW experiments generate the axion-like particles themselves, they can directly measure $g_{a\gamma}$. This is an advantage of this style of experiment over other axion-like particle searches such as haloscopes and helioscopes which rely on models of axions as dark matter or of their generation in the sun respectively.

ALPS II will take place in a section of the tunnel formerly occupied by the HERA experiment. Strings of ten 5.3 T superconducting HERA dipole magnets will be used to generate the magnetic fields before and after the wall giving ALPS II 468 T·m of magnetic field length in each of these regions. ALPS II will also be the first LSW experiment to use optical cavities before and after the wall to boost the probability that a photon will convert to an axion-like particle and then back to a photon after the wall. The power build up of the cavities, along with the long baseline, high magnetic field, and improvements in the detector technologies will help improve the sensitivity of ALPS II to the coupling between photons and axion-like particles over previous generations of LSW experiments by a factor of roughly 1000 [5]. For masses below 0.11 meV ALPS II will be able to detect axion-like particles down to couplings of $g_{a\gamma} \approx 2 \times 10^{-11}\,\mathrm{GeV}^{-1}$ [1] for a two week integration time.

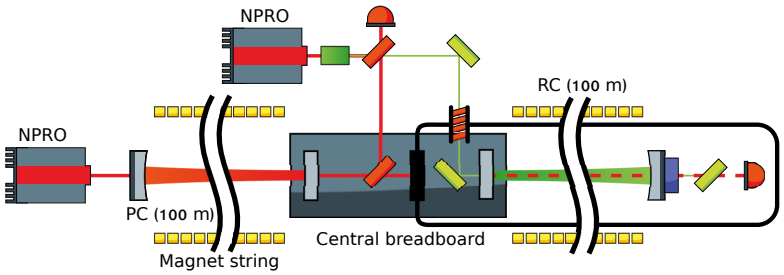

Figure 1: ALPS IIc optical system.

2 Optical system

The research and development for the ALPS II optics is taking place in two stages. The first, ALPS IIa, is a 20 m testbed for the individual optical systems [6]. The second stage, ALPS IIc, represents the full scale 200 m experiment and is shown in Figure 1. The setup is composed of two ∼100 m optical cavities with the production cavity (PC) before the wall and the regeneration cavity (RC) after the wall. The PC will be seeded with a 30 W fiber amplified nonplanar ring oscillator (NPRO) laser operating at 1064 nm. With a power build up of 5000, the PC aims to achieve a circulating power of 150 kW. The input optics will also be equipped with an automatic alignment system to maintain the coupling of the laser to the cavity. 50 kW of power has already been demonstrated in the 9.2 m ALPS IIa PC along with an automatic alignment system that allows the cavity to be stably operated for the anticipated measurement time of ALPS IIc.

The length of the RC must be resonant with the light circulating in the PC since the axion-like particles will have the same energy as the photons generating them. This requires stabilizing the differential length noise between the cavities to better than 0.5 pico-meters. The sensing of the RC length will be performed with a 1064 nm NPRO laser on the central optical table whose frequency is referenced to the light transmitted by the PC. This laser is then frequency doubled and the 532 nm light is coupled into the RC. This is necessary since 1064 nm light cannot be used as it would be indistinguishable from the regenerated photons. Because of this, the RC must be housed in a light-tight enclosure and requires dichroic mirrors that are reflective for both 1064 nm and 532 nm. The probability of axion-like particles reconverting to photon scales with the power build up of the RC for 1064 nm. Therefore, this value is chosen to be as high as possible, at 40,000. The power build up for green light is significantly lower at 55 to avoid having a high circulating power. This substantially lower power build up for green means that the light sensing the length of the RC must be stabilized to better than 1/10,000 of the cavity's linewidth.

In ALPS IIa the RC frequency control system has demonstrated the ability to maintain the resonance condition of a frequency doubled 1064 nm NPRO laser to better than the required 0.5 pm stability using the green light to probe the length of the cavity. Furthermore, a custom designed mirror mount composed of a piezoelectric actuator and a wave washer has demonstrated the ability to control the position of a 50 mm mirror with a ∼4 kHz control bandwidth and enough gain to suppress the environmental noise below the 0.5 pm requirement. This demonstrates that it will be possible to operate ALPS IIc without any additional seismic isolation. A separate 1064 nm was injected into the ALPS IIa RC and the power build up was measured to be 26,000±1,000.

The eigenmodes of the cavities must also share a spatial overlap of 95% to ensure that the electromagnetic component of the axion-like particles couples to the RC. This requires that the eigenmodes of the cavities have less than a 5 µrad angular misalignment and less than a 1.3 mm offset in their lateral position. To prevent any angular misalignment, the flat cavity mirrors at the center of the experiment will both be mounted to an in vacuum central optical bench (COB). The lateral position of the eigenmodes will be monitored with photodetectors mounted to the COB and this information will be fed back to three axis piezoelectric mounts that can actuate on the angle of the curved mirrors of the cavities. This will be used to maintain the lateral position of the eigenmodes with respect to the COB. Before a measurement run, the spatial overlap between the cavities can be checked by opening a shutter in the light-tight housing on the COB and allowing light transmitted by the PC to couple directly to the RC.

The alignment of the mirrors on the COB has been demonstrated by mounting mirrors to a test COB using Polaris® mirror mounts. The alignment noise of the mirrors was measured using a Trioptics TriAngl©r 300-57 auto-collimator. This measurement showed a peak-to-peak alignment drift of below 2 µrad over the course of a 5 day period.

3 Detection Systems

ALPS II will have the benefit of using two independent single photon detection systems to confirm the results of the experiment. One of these systems, known as the transition edge sensor (TES), is a microcalorimeter capable of measuring the temperature change induced by incident photons. The other measurement system uses a heterodyne detection technique to measure the optical interference signal between the regenerated photons and a local oscillator.

The TES detection system exploits a thin tungsten film stabilized at its critical temperature between normal and superconductivity by a bias current. It is read out via a two stage SQUID amplifier [7]. When photons are absorbed by the film they will increase its temperature slightly for a brief period of time. This will in turn cause a change in the resistance of the tungsten and lead to a sudden drop in current. At the moment the cryostat has been successfully set up and the rest of the system is being optimized.

The heterodyne detection technique measures the interference beatnote between the regenerated photons and a local oscillator. By exactly knowing the relative frequencies of these fields, the measured data can be demodulated at the signal frequency. This concept relies on the phase coherence between the regenerated field and the local oscillator which requires that the local oscillator is phase coherent with the light circulating in the PC. A demonstration of this system showed that it was capable of measuring a signal with a power of 1 photon per 30 s with no measureable background over the course of two weeks [8]. For a more detailed overview and status report please see the article in these proceedings by G. Messineo.

4 Site preparation and timeline

As mentioned earlier, ALPS IIc will require twenty superconducting HERA dipole magnets. Since these magnets were originally used in the arcs of the HERA accelerator, they must be unbent to provide sufficient aperture for the cavity eigenmodes. At the moment, sixteen of the magnets have been unbent and successfully operated. Furthermore, as Figure 2a shows, two magnets were connected in a test string to confirm that the interconnections between the

(a)

(b)

Figure 2: (a) Test string of two magnets. (b) The cleared HERA tunnel.

straightend magnets function properly. The tunnels and hall that will house ALPS IIc have also been cleared in preparation for the experiment as seen in Figure 2b.

The construction of the cleanroom for the first laser area of ALPS IIc is scheduled for fall 2019. The installation of the first string of ten magnets for the PC should be completed by early 2020 with the installation of the second string of ten magnets for the RC finished by summer 2020. The installation of the full scale optical system will be completed during the fall of 2020, and the ALPS collaboration is looking forward to begin taking data at the end of 2020.

Acknowledgments

The ALPS Collaboration would like to thank the DESY accelerator division, especially the MEA, MKS and MVS groups for their crucial support. This work is financially supported by the Helmholtz Foundation, the Deutsche Forschungsgemeinschaft, the Heising-Simons Foundation under Grant No. 2015-154, and the NSF under Grants No. 1505743 and No. 1802006.

References

[1] R. Bähre, *et al.*, "Any light particle search II — Technical Design Report," J. Instrum. **8**, T09001 (2013) doi:10.1088/1748-0221/8/09/T09001 [arXiv:1302.5647 [physics.ins-det]].

[2] S. Weinberg, "A New Light Boson?," Phys. Rev. Lett. **40** (1978) 223. doi:10.1103/PhysRevLett.40.223

[3] F. Wilczek, "Problem of Strong P and T Invariance in the Presence of Instantons," Phys. Rev. Lett. **40** (1978) 279. doi:10.1103/PhysRevLett.40.279

[4] R. Peccei, and H. Quinn., "CP Conservation in the Presence of Instantons," Phys. Rev. Lett. **38**, 1440 – 1443 (1977) doi:10.1103/PhysRevLett.38.1440

[5] J. Redondo and A. Ringwald, "Light shining through walls," Contemp. Phys. **52** (2011) 211 doi:10.1080/00107514.2011.563516 [arXiv:1011.3741 [hep-ph]].

[6] A. Spector, *et al.*, "Characterization of optical systems for the ALPS II experiment," Opt. Express **24** 9237 (2016) doi:10.1364/OE.24.029237 [arXiv:1609.08985 [physics.optics]].

[7] J. Dreyling-Eschweiler *et al.*, "Characterization, 1064 nm photon signals and background events of a tungsten TES detector for the ALPS experiment," J. Mod. Opt. **62**, 1132 – 1140 (2015) doi:10.1080/09500340.2015.1021723 [arXiv:1502.07878 [physics.ins-det]].

[8] Z. Bush, *et al.*, "Coherent detection of ultraweak electromagnetic fields," Phys. Rev. D **99** 022001 (2019) doi:10.1103/PhysRevD.99.022001 [arXiv:1710.04209 [physics.ins-det]].

Searching for Solar KK Axions with a Gaseous Detector

Francisco A. Vazquez de Sola Fernandez[1], *on behalf of the NEWS-G collaboration*[2]

[1]Queen's University, Kingston, Canada
[2] https://news-g.org/dark-matter/

DOI: http://dx.doi.org/10.3204/DESY-PROC-2018-03/Vazquezdesola_Francisco

In theories with extra dimensions, the standard QCD axion has excited states with higher mass. These Kaluza-Klein (KK) axions would have a significantly shorter decay time and, when produced by the Sun, would remain gravitationally trapped in the Solar System, boosting their local decay rate. A low density detector would distinguish such decays from background, by identifying the separate location of the capture of the two resulting photons. The NEWS-G collaboration uses Spherical Proportional Counters, gas-filled metallic spheres with a high voltage electrode in their centre. This paper shows preliminary results for the KK axion search with NEWS-G.

1 Solar Kaluza-Klein axions

The QCD axion, as motivated by the Strong CP problem, could theoretically decay into two photons, though its half life is orders of magnitude larger than the age of the Universe. However, in theories with extra dimensions, the axion gains higher mass modes, called Kaluza-Klein (KK) axions. Notably, these modes would have much shorter lifetimes, so their decay would be observable. Furthermore, part of the KK axions produced in the Sun would become trapped in its gravity well, greatly boosting their local density. Simulations show that solar KK axions could also explain phenomena such as the solar coronal heating problem, motivating a search for them [1]. In those models, the expected decay rate on Earth would be $\sim 0.1\,\mathrm{m}^{-3}\mathrm{day}^{-1}$.

2 NEWS-G detector

The NEWS-G collaboration (New Experiments With Spheres - Gas) uses Spherical Proportional Counters (SPCs) to search for Weakly Interacting Massive Particles (WIMPs). The current detector, NEWS-G-LSM, located in the Laboratoire Souterrain de Modane [2], consists of a spherical copper shell (60 cm in diameter, or $\sim 0.11\,\mathrm{m}^3$ in volume) filled with a noble gas, with an electrode at its centre, supported by a grounded metallic rod. The electrode is kept at a high voltage ($\sim 2000\,\mathrm{V}$) through a wire inside the rod. When a particle interacts with the gas, it converts some of its energy into ionization, with the resulting electrons drifting towards the central electrode. The high electric field there causes an avalanche, amplifying the signal from the electrons. For a detailed explanation of the detector, see Ref. [3].

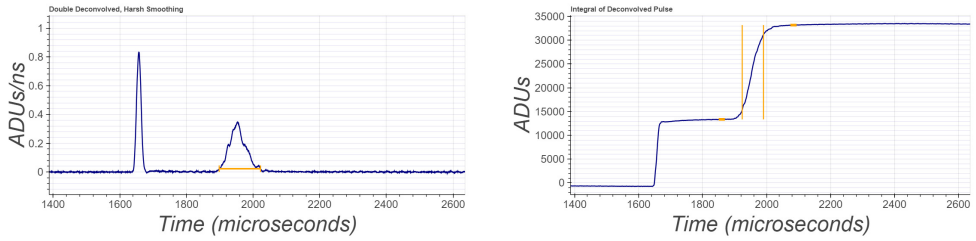

Figure 1: **Left:** Double-pulse event example, post-deconvolution; the yellow line at the second pulse shows the threshold to find pulses. **Right:** Same event, post-deconvolution and integration; the amplitude of each pulse is its height; the risetime is the time between 10% and 90% of its amplitude, as indicated by the vertical yellow lines for the second pulse.

An SPC is uniquely adapted for KK axion searches. In a gas detector at low enough pressures, the two photons produced back-to-back by a KK axion decay will travel some distance before interacting. As such, they can be resolved as happening at different locations. A search for coincident events leads to very strong rejection of background, allowing detection of axion decays despite their low rate. Using gas is not a detriment, since the decays happen irrespective of the medium, so the exposure depends only on the volume of the detector, not its mass.

3 Data analysis

To identify multiple-pulse events, the response function of the detector is deconvolved from the raw event to recover the 'instant current' from primary electrons. A threshold check identifies the beginning and end of each group of electrons, and the event is separated into pulses. The amplitude and risetime (estimators of the energy and radial location of the event) are computed for each of the pulses, as shown in Fig. 1. An event is considered axion-like if it contains two pulses of similar amplitude, close together in time (up to 400 μs difference in arrival time from different locations), and with characteristics consistent with those of other physical pulses.

As an empirical proof-of-concept for the procedure, a ^{222}Rn source was introduced in a test detector at Queen's University. The 30 cm detector, filled with 800 mbar of Argon with 2% CH_4, took data for 24 h. The main visible sources were the 5.5 MeV α from ^{222}Rn, the 6.0 MeV α from ^{218}Po, and the 7.7 MeV α from ^{214}Po. Since ^{214}Po has a half-life of $\sim 160\,\mu$s, we expect to see the decay from its radioactive mother, ^{214}Bi, shortly before. By applying a cut to select only for events with two pulses in it, we reject the ^{222}Rn and ^{218}Po events, as shown by Fig. 2.

Simulations were also performed to compute the sensitivity of this approach to axion-like events. By using NIST's photon attenuation length database [4], the distance travelled by the back-to-back photons created by a KK axion decay can be derived. Then, with field maps and electron drift characteristics computed from COMSOL [5] and Magboltz [6] respectively, the drift time of the primary electrons from each photon can be simulated. By convolving it with the single-electron response of the detector, axion-like events are produced. Double-pulse cuts are finally applied, and the sensitivity of the detector to KK axion decays was calculated to be around $\sim 25\%$, for the running conditions described in Sec. 4. A similar procedure was carried out for simulated single-pulse events, obtaining a false-positive rate of order $1 : 10^6$. This is adequate to produce first results.

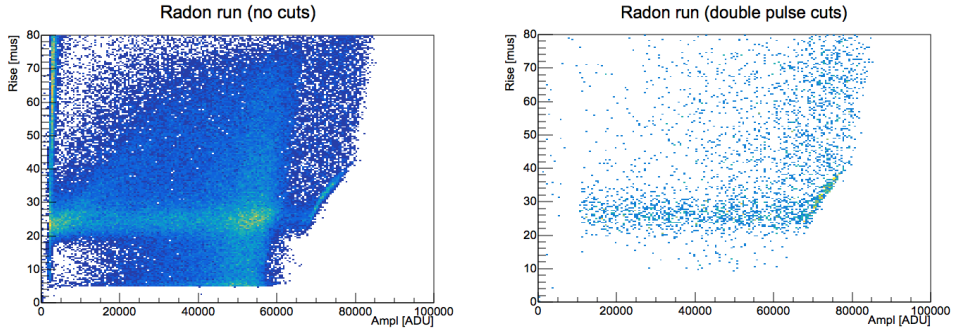

Figure 2: **Left:** Risetime vs amplitude of a 24 h ^{222}Rn run; the 5.5 MeV α from ^{222}Rn and the 6.0 MeV α from ^{218}Po appear as the vertical line at 55 kADUs; the 7.7 MeV α from ^{214}Po appear as the thinner, slanted line at $65 - 80$ kADUs; the horizontal line at 25 μs are the αs from all three sources that exit the detector before leaving all their energy in it. **Right:** Same run, after cuts to select events preceded by a smaller pulse; only the events from ^{214}Po remain.

4 Preliminary results

A 42-day-long run was taken with NEWS-G-LSM, with a 3.1 bar mixture of Neon and CH_4 (0.7%), originally for WIMP search [3]. For a sphere of diameter 60 cm, that corresponds to 4.75 $m^3 \cdot$ days of exposure. Accounting for the efficiency of the detector and data processing, the expected number of counts of KK axion decays in that run is ~ 0.1 events, assuming the preferred parameters for the solar KK axion model. While this is too low to set constraints on their existence, the run can still be used to test the background rejection capacity of this approach.

Of the $\sim$ 1 640 000 events observed during that period, $\sim$ 100 000 pass basic pulse-shape-discrimination cuts that eliminate spurious pulses. After applying the KK axion search cuts, 73 candidate events were found in the preliminary region of interest, as shown on Fig. 3. Their distribution and number suggest they likely come from background sources.

A preliminary exclusion limit on the axion-photon coupling can be derived from Poisson statistics by doing the conservative (if unrealistic) assumption that all the observed events come from KK axion decays, as seen in Fig. 3. For comparison, an ideal background-free exclusion limit for the same setup is also shown. To our knowledge, the only pre-existing exclusion limit was set by XMASS [7]. We see that our preliminary limit appears to be more stringent, encouraging further research.

5 Next steps

Systematic uncertainties are being calculated. A detailed analysis of the background of NEWS-G-LSM is also being performed, to optimize the choice of the region of interest for improved background rejection. Compton scattering of photons due to ^{210}Pb contamination in the inner surface of the sphere and improperly reconstructed events are expected to be the main sources of background.

The next phase of the NEWS-G experiment is a 140 cm sphere ($\sim 1.44\,m^3$), to be installed

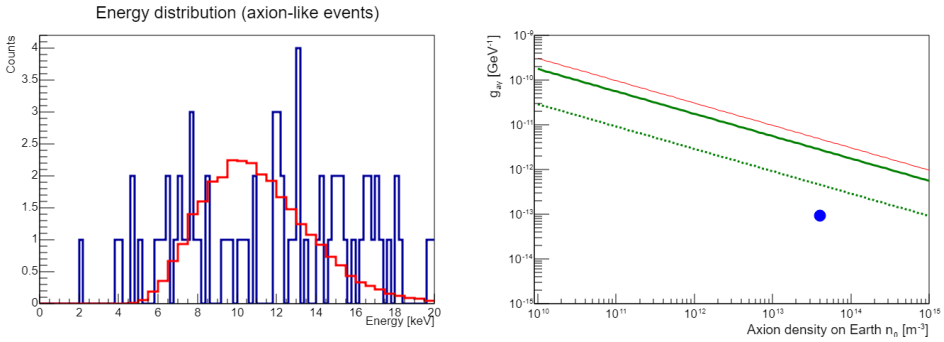

Figure 3: **Left:** Energy distribution of observed KK axion candidate events, with expected distribution superimposed. **Right:** Axion-photon coupling constant (GeV^{-1}) vs solar KK axion density on Earth (m^{-3}). Thin red line: XMASS exclusion limit. Solid green line: NEWS-G preliminary exclusion limit with NEWS-G-LSM. Dotted green line: Background-free exclusion limit. Blue dot: Parameter space that would explain the solar corona heating problem.

at SNOLAB [8]. Its improved design should allow us to reach the exposure and background level necessary to probe the region of interest of the solar KK axion model.

6 Acknowledgements

The help of the technical staff of the Laboratoire Souterrain de Modane is gratefully acknowledged. NEWS-G-LSM is partially funded by the European Commission program ILIAS. This work was undertaken, in part, thanks to funding from the Canada Research Chairs program.

References

[1] L. DiLella, K. Zioutas, "Observational evidence for gravitationally trapped massive axion(-like) particles," Astropart. Phys. **19**, no. 1, 145-170 (2003) doi:10.1016/S0927-6505(02)00186-X [arXiv:astro-ph/0207073].

[2] F. Piquemal, "Modane underground laboratory: Status and project," Eur. Phys. J. Plus **127**, 110-114 (2012) doi:10.1140/epjp/i2012-12110-3.

[3] Q. Arnaud *et al.*, "First results from the NEWS-G direct dark matter search experiment at the LSM," Astropart. Phys. J. C **97**, 54-62 (2018) doi:10.1016/j.astropartphys.2017.10.009 [arXiv:1706.04934 [astro-ph.IM]].

[4] J.H. Hubbell, S.M. Seltzer, "Tables of X-Ray Mass Attenuation Coefficients and Mass Energy-Absorption Coefficients (version 1.4)," http://physics.nist.gov/xaamdi (2004) doi:10.18434/T4D01F.

[5] COMSOL, Inc, "COMSOL Multiphysics Reference Manual (version 5.3)," https://www.comsol.com.

[6] S.F. Biagi, "Monte Carlo simulation of electron drift and diffusion in counting gases under the influence of electric and magnetic fields," Nucl. Instr. and Meth. A **421**, 234-240 (1999) doi:10.1016/S0168-9002(98)01233-9.

[7] XMASS Collaboration, "Search for solar Kaluza-Klein axion by annual modulation with the XMASS-I detector" PTEP **2017**, no. 10, 103C01 (2017) doi:10.1093/ptep/ptx137 [arXiv:1707.08995 [hep-ex]].

[8] F. Duncan, A.J. Noble, D. Sinclair, "The construction and anticipated science of SNOLAB," Ann. Rev. Nuclear Part. Sci. **60**, 163-180 (2010) doi:110.1146/annurev.nucl.012809.104513.

Index

List of Participants

Gonzalo Alonso lvarez - Heidelberg University
Pedro Alvarez - Universida de Antofagasta
Garcon Antoine - Helmholtz-Institut Mainz
Arata Aoki - Kobe University
Sergio Arguedas Cuendis - CERN
Justin Baier - Albert-Ludwigs-Universitt Freiburg
Keith Baker - Yale University
Csaba Balazs - Monash University
Iason Baldes - DESY
Sebastian Baum - Oskar Klein Centre
Ankit Beniwal - Oskar Klein Centre
John Blanchard - Helmholtz-Institut Mainz
Cristian Boffo - Bilfinger Noell GmbH
Riccardo Brugnera - Padova University
Ramy Brustein - Ben Gurion University
Malte Buschmann - University of Michigan
Zachary Bush - University of Florida
Gary Centers - Helmholtz-Institut Mainz
Aleksandr Chatrchyan - Heidelberg University
Chun Eung Jin - Korea Institute for Advanced Study
Woohyun Chung - IBS / CAPP
Chitta Ranjan Das - Bogoliubov Laboratory of Theoretical Physics
Emilio Depero - ETH
Alexander Derbin - Petersburg Nuclear Physics Institute
Klaus Desch - University of Bonn
Inma Dominguez - Universidad de Granada
Michael Duerr - DESY
Xiaolong Du - University of Goettingen
Babette Dbrich - CERN
Benedikt Eggemeier - University of Goettingen
Damian Ejlli - Novosibirsk State University
Anne Ernst - DESY
Nataniel Figueroa Leigh - Johannes Gutenberg Universitt
Horst Fischer - ALU Freiburg
Victor Flambaum - University of New South Wales
Katarzyna Frankiewicz - National Centre for Nuclear Research

Carlos Frenk - Durham University
Wolfgang Funk - CERN
Giorgio Galanti - INAF, Osservatorio Astronomico di Brera
Irina Galstyan - Stockholm University
Loredana Gastaldo - Heidelberg University
Claudio Gatti - LNF-INFN
Michael Gehring - Bilfinger Noell GmbH
Maurizio Giannotti - Barry University
Marina Gil Sendra - Johannes Gutenberg Universitt
Paolo Gondolo - University of Utah
Marco Gorhetto - SISSA
Maxim Goryachev - University of Western Australia
Daniel Grin - Haverford College
Ayman Hallal - University of Florida
Klaus Helbing - University of Wuppertal
Reyco Henning - University of North Carolina Chapel Hill
Heiko Hintz - DESY
Sebastian Hoof - Imperial College London
Shu-Yu Ho - Tohoku University
Nick Houston - ITP-CAS
Junwu Huang - Perimeter Institute
Igor Irastorza - Universidad de Zaragoza
Jordi Isern - Institut de Ciencies de l'Espai
Joerg Jaeckel - ITP Heidelberg
Friederike Januschek - DESY
Katharine Kelley - ICRAR-UWA
Chris Kelso - University of North Florida
Jingeun Kim - Center for Axion and Precision Physics Research
Younggeun Kim - IBS / CAPP
Ronald Klos - DESY
Alexandr Korochkin - Institute for Nuclear Research
Todd Kozlowski - University of Florida
Christoph Krieger - University of Hamburg
Stepan Kunc - Technical University of Liberec
Ranjan Laha - Johannes Gutenberg Universitt
Rafael Lang - Purdue University
Soohyung Lee - IBS / CAPP
Erik Lentz - Universitt Gttingen
Dmitry Levkov - Institute for Nuclear Research
Axel Lindner - DESY
Andrei Lobanov - University of Hamburg
Bla Majorovits - Max-Planck-Institut fr Physik
Jhilik Majumdar - University of Hamburg
Adeel Mansha - Institute of Theoretical Physics
David Marsh - University of Goettingen
M.C. David Marsh - University of Cambridge
Engler Martin - Helmholtz Institut Mainz

Emi Masaki - Kobe University
Ben McAllister - ARC Centre of Excellence for Engineered Quantum Systems
Giuseppe Messineo - University of Florida
Alexander Millar - Max-Planck-Institut fr Physik
Alessandro Mirizzi - University of Bari
Daniele Montainino - Univ. Salento
Guido Mueller - University of Florida
Francisco Neves - Laboratorio de Instrumentacao e Fisica Experimental de Particulas
Le Hoang Nguyen - University of Hamburg
Jens Niemeye - University of Goettingen
Ciaran O'Hare - Universidad de Zaragoza
Ippei Obata - ICRR, University of Tokyo
Gulden Othman - University of North Carolina Chapel Hill
Jonathan Ouellet - Massachusetts Institute of Technology
Alexander Panin - Institute for Nuclear Research
Andreas Pargner - Karlsruhe Institute of Technology
Jan Hendrik Pold - DESY
Peter Quinn - International Centre for Radio Astronomy Research
Nicholas Rapidis - University of California Berkeley
Javier Redondo - Universidad de Zaragoza
Olaf Reimann - Max-Planck-Institut fr Physik
Andreas Ringwald - DESY
Markus Rummel - McMaster University
Giuseppe Ruoso - Laboratori Nazionali Legnaro
Ken'ichi Saikawa - Max-Planck-Institut fr Physik
Filippo Sala - DESY
Kazufumi Sato - ICRR, University of Tokyo
Ignacy Sawicki - CEICO
Adam Scherlis - Stanford University
Dennis Schmelzer - AEI Hannover
Kai Schmitz - Max-Planck-Institut fr Kernphysik
Uwe Schneekloth - DESY
Marc Schumann - University of Freiburg
Bodo Schwabe - Universitaet Goettingen
Thomas Schwetz - Karlsruhe Institute of Technology
Thomas Schoerner-Sadenius - DESY
Jan Schuette-Engel - University of Hamburg
Yannis Semertzidis - CAPP / KAIST
Geraldine Servant - DESY
Gnter Sigl - University of Hamburg
Richard Smith - DESY
Andrew Sonnenschein - Fermilab
Aaron Spector - DESY
Yevgeny Stadnik - Johannes Gutenberg Universitt
Frank Steffen - Max-Planck-Institut fr Physik
Miroslav Sulc - Technical University of Liberec
David Tanner - University of Florida

Natalia Tapi - Universidad de Santiago de Chile
Hugo Teras - University of Lisbon
Lennert Thormhlen - University of Heidelberg
Igor Tkachev - Institute for Nuclear Research
Michael Tobar - University of Western Australia
Dieter Trines - DESY
Pranjal Trivedi - University of Hamburg
Evgeniy Unzhakov - Petersburg Nuclear Physics Institute
Francisco Andres Vazquez de Sola - Queen's University
Jan Veltmaat - University of Goettingen
Luca Visinelli - Stockholm University
Belina Krosigk - University of British Columbia
Arne Wickenbrock - Johannes Gutenberg Universitt
Walter Wilson - Yale University
Lindley Winslow - Massachusetts Institute of Technology
Pengwei Xie - Tsung-Dao Lee Institute
SungWoo Youn - Institute for Basic Science
Chao Zhang - University of Hamburg
Ariel Zhitnitsky - University of British Columbia
Konstantin Zioutas - University of Patras

151 participants